IOWA STATE UNIVERSITY
Digital Repository

2015

Chemical and thermal stability of semiconductors

Malinda Denise Reichert
Iowa State University

Follow this and additional works at: https://lib.dr.iastate.edu/etd

 Part of the Chemistry Commons

www.manaraa.com

Chemical and thermal stability of semiconductors

by

Malinda Denise Reichert

A dissertation submitted to the graduate faculty

in partial fulfillment of the requirements for the degree of

DOCTOR OF PHILOSOPHY

Major: Chemistry

Program of Study Committee:
Javier Vela, Major Professor
Wenyu Huang
Gordon Miller
Patricia Thiel
Keith Woo

Iowa State University

Ames, Iowa

2015

TABLE OF CONTENTS

ACKNOWLEDGEMENTS

First, I would like to thank my advisor, Javier Vela, for his guidance and encouragement throughout the years. I've learned a great deal to further my career as a chemist. I would also like to thank my committee members, Andreja Bakac (retired), Wenyu Huang, Gordon Miller, Patricia Thiel and Keith Woo, for their support.

Next, I want to thank my parents, Dennis and Debbie Reichert, for all their love, support, and encouragement throughout my journey. You both have always supported my decisions (although may not always have agreed) and been there whenever needed. I cannot express how appreciative I am and would not have made it this far without you both. You are my rocks. I also want to thank my grandmas, Louise Cummings and Betty Reichert, who are two special ladies. They were always supportive and inquisitive of how school was progressing. Coming home is/was always more special seeing them and I treasure those memories. I only wish Grandma Louise would have been around for my final graduation.

Finally, I need to thank the Vela group, past and present, Purnima Ruberu, Yijun Guo, Elham Tavasoli, Patrick Dilsaver, Sam Alvarado, Chia-Cheng (John) Lin, Michelle Thompson, Long Men, Himashi Andaraarachchi, Feng Zhu, Arthur White, Hannah Crotty, Bryan Rosales, and Josie Del-Pilar-Albaladejo. You have all made these past five years fun (well as fun as graduate school can be). We have had some great memories such as group picnics to Big Creek and floating down the Skunk River. Individually, I want to thank Purnima for training me in lab and being such a great friend through the years. I want to especially thank Pat and Yijun for being coffee/workout buddies and in general partners in crime while they were at ISU. I want to thank Sam and Michelle for the stimulating

commentary in the office. Thank you John and Long for helping to fill spots so there were enough people to play basketball. I also need to thank some very special people outside of the Vela group who have kept me sane throughout theses past five years, Chris Scobba, A.J. Lane, Toshia Albright and many more.

ABSTRACT

Utilization of solar energy continues to be a prominent topic in our society. The chemical and thermal stability of semiconductors is of great interest due to their widespread appeal and applicability as photoactive materials and in energy conversion devices. However, aside from surface chemistry studies and photo degradation (under continuous illumination), the general chemical reactivity and thermal stability of these materials is poorly understood. In this thesis, we use CdSe and CdS nanorods as model systems to investigate the behavior of II-VI semiconductor nanorods against various conditions of "extreme" chemical and physical stress (acids, bases, oxidants, reductants, heat). We demonstrate CdSe nanorods completely degrade in the presence of acids, but retain their structural and optical properties when subjected to basic or oxidative environments. Reductants, such as n-butyllithium, reduce CdSe to cadmium metal but hydrogen does not. Thermal treatment of both CdSe and CdS nanorods results in annealing, axial melting, and then coalescence of the particles. Axial melting did not depend on the type of inorganic material but on the ligand(s) coating the nanorod surface.

We also explore the synthesis of copper nitride (Cu_3N) nanocrystals by nitridation of Cu_2O nanocrystals with either ammonia or urea. We characterize the structure, optical properties, and morphology of both oxide and nitride phases using structural, optical and computational methods. Upon exposure to moisture and air, Cu_3N decomposes to CuO. Simple thermodynamics calculations explain that the observed concomitant release of NH_3 and N_2 is due to kinetic factors.

Finally, we investigate the thermal stability of bulk methylammonium lead halide perovskites ($CH_3NH_3PbX_3$ where X = I, Br, or Cl) to determine the decomposition products. Using thermogravimetric analysis (TGA) and differential scanning calorimetry (DSC) coupled with a quadrupole mass spectrometer (QMS) and Fourier-Transform infrared (FT-IR) spectrometer, the decomposition temperature and evolved gas products are analyzed. Bulk iodide and bromide decompose by a similar route compared to that of the bulk chloride. For the iodide and bromide, ammonia and methyl halide evolve but the bromide evolves methylamine too. The chloride acts similar to reports in literature with evolution of methylamine and HCl. However, peaks for HCl overlap with the CH_3 stretching of methylamine making it difficult to distinguish. Using this data and decomposition pathways, a way to achieve long-term thermal stability may be determined for methylammonium lead halide perovskites for solar cells.

CHAPTER 1

INTRODUCTION

General Introduction

In one hour, more light energy (4.3 x 10^{20} J) from the sun hits the Earth than is used (4.1 x 10^{20} J) in a year.[1] Thus, utilization of this potential solar energy continues to be of great interest. Two interesting processes for using solar energy are photovoltaics and photocatalysis. Recently, semiconductor materials such as nanocrystals have emerged as candidates for light harvesting.

A semiconductor is a material with conductivity and other properties between a metal and an insulator.[2,3] It has a band gap defined as the distance between the bottom of the conduction band and the top of the valence band (Figure 1A) energy levels. The band gap determines if the material is a semiconductor or not.[2,4] In general, a semiconductor's conductivity increases as temperature increases so conductivity cannot determine if a material is a semiconductor alone.[2,3] Semiconductors that have dimensions of 1-100 nm are nanocrystals and show a mix of solid-state and atomic properties, for example size dependent optical and electronic properties, from tuning the size of the band gap.[4,5] These nanocrystals can demonstrate the quantum confinement effect, which is similar to a particle in a box model.[4,6]

Quantum confinement results from electrons and holes being compressed into dimensions close to the exciton Bohr radius, which is the energy difference between the electron in the conduction band and the "hole" left behind in the valence band.[4,7-9] The exciton Bohr radius controls the size at which the energy levels are quantized instead of being treated as continuous such as a bulk semiconductor and changes the electronic and optical properties of the nanocrystals.[4,7-9] As the nanocrystal size decreases, the spacing between the valence band and

conduction band increases, due to quantum confinement.[6] The exciton Bohr radius is used to characterize a crystal a quantum confined nanocrystal or a bulk semiconductor.[7-9] Bulk semiconductors, along with quantum confined nanocrystals, have a band gap energy, which is the minimum energy needed to excite an electron from the valence band to the conduction band, that is compositionally dependent. A hole is left in the valence band when a photon of greater energy is absorbed and exciton generated.[4] The relaxation of the excited electron back to the valence band may emit a photon and remove the exciton. Along with the band gap being compositionally dependent, fluorescence and absorption wavelengths change with the size of the nanocrystal, Figure 1C.[4,5] The size of the nanocrystal is controlled in the synthesis.
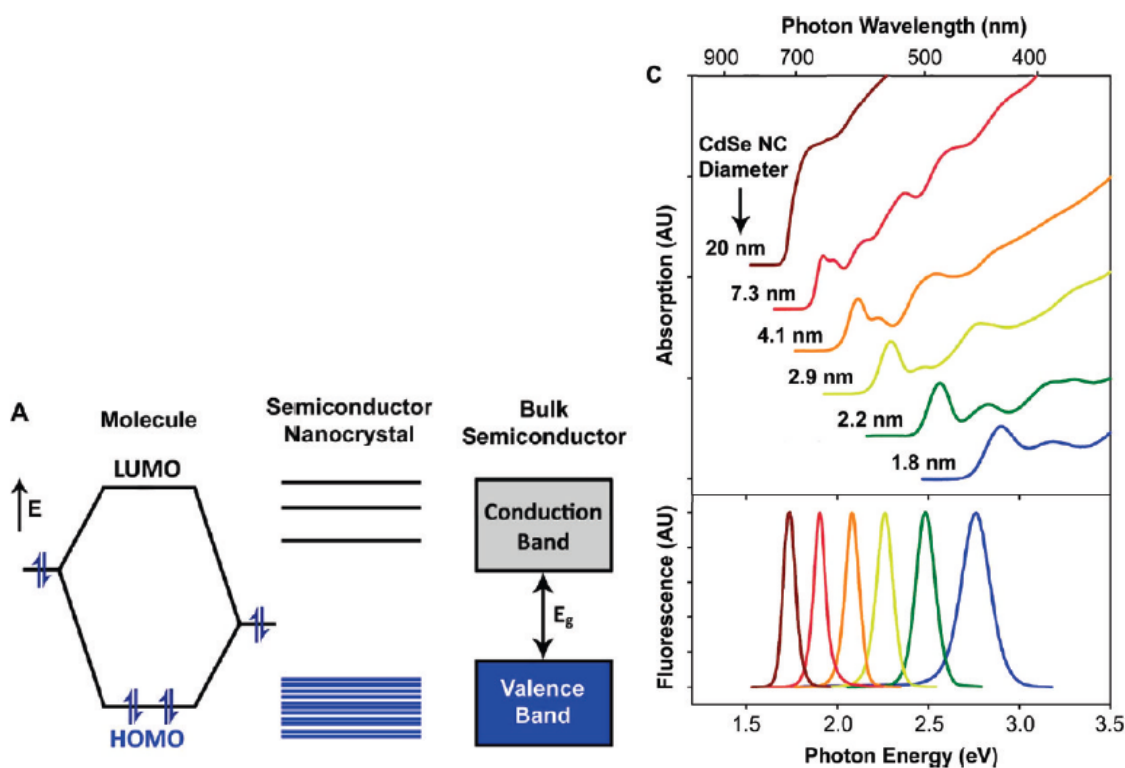

Figure 1. (a) Electronic energy states of a semiconductor in the transition from discrete molecules to nanosized crystals and bulk crystals. (c) Absorption (upper) and fluorescence (lower) spectra of CdSe semiconductor nanocrystals.[4]

There are different types of dimensions for nanocrystal semiconductors, 0D quantum dots, 1D quantum wires, 2D quantum wells, and 3D bulk materials. Zero-dimensional materials are confined in all three directions, 1D quantum wires are confined in 2, 2D in one and bulk materials are not confined, see Figure 2.[10]
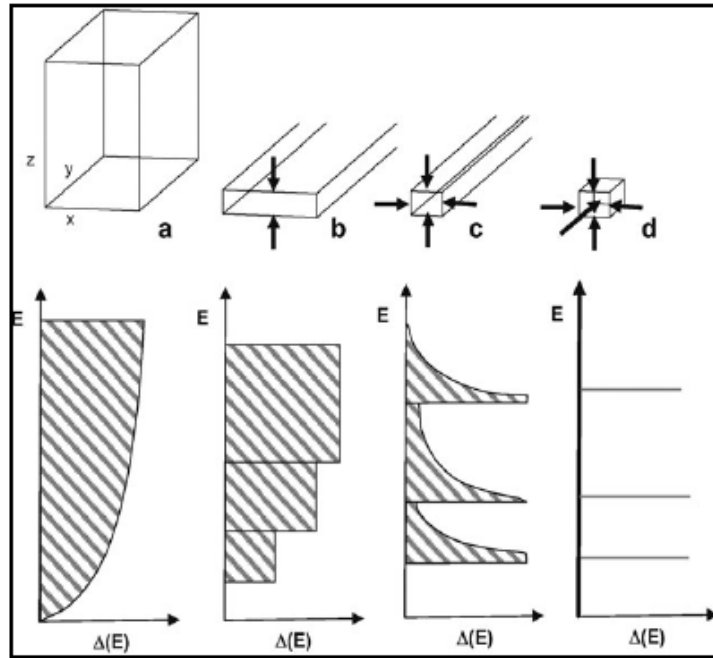
Figure 2. Scheme showing the concept of dimensionality for a bulk semiconductor – 3D (a) quantum well – 2D (b) quantum wire – 1D (c), and quantum dot – 0D (d) along with the corresponding density of states for ideal cases.[10]

The quantum confinement of nanocrystals is dependent on size, composition and shape.[11] Nanorods are in between quantum dots and quantum wires, and the diameter and length are controlled. The band gap decreases as the aspect ratio (length/diameter) increases.[11] Nanorod optical properties differ significantly from quantum dots. Compared to QDs, nanorods have higher photoluminescence quantum efficiency, suppression of non-radiative Auger processes, linear polarized PL, an increase in Stokes shift, faster carrier relaxation, and multiple exciton generation.[12-15] The properties of semiconductor nanocrystals, such as tunable band gaps, intense

and broad absorption, long-lived excitons, and good solubility, make them ideal as light harvesters.

Nanocrystals have applications in areas such as solar energy, optoelectronic devices, biological imaging, photovoltaic devices, single-electron transistors, and ultrasensitive detection.[4,16,17] Furthermore, the properties of quantum dots and rods such as the size tunable band gap, absorption, and photoluminescence, large molar extinction coefficients, and sizable dipole moment, are utilized in applications such as lasers, LEDs, photodetectors, transistors, thermoelectric purposes, memory elements, and biological imaging and analyses.[17-21] The utilization of light as renewable energy continues to be of great research interest. Two main processes looked at are converting sunlight to electricity using photovoltaics and using sunlight for photocatalysis to produce fuels such as hydrogen.[22-24] Semiconductors and colloidal nanocrystals are being explored as inexpensive and efficient materials for renewable energy.[1,17,25,26] However, there are issues with solar cells and semiconductor nanocrystals that limit efficiencies such as optical absorption, charge recombination, electron injection, hole scavenging, electrolyte, and counter-electrode effect.[18,19] The thermal and chemical stability of nanocrystals and light harvesting materials is also problematic for some applications.

Chemical and Thermal Stability of Nanocrystals

Nanostructured materials are in a non-equilibrium state. Stability of nanostructured materials is not uniform and the largest set of data is on grain growth where the chemical stability and deformation stability were not investigated.[27-29] The stability of metallic nanostructured nanocrystals has been reviewed under extreme temperature, radiation and deformation conditions; however, it did not include semiconductors due to the lack of systematic data.[30] Thermal activation, radiation, corrosion and deformation can stimulate and enhance

diffusion, grain growth, and homogenization resulting in partial or total loss of the nanostructure along with its associated properties. The thermal behavior is complicated by abnormal grain growth where larger grains consume smaller grains resulting in a bimodal size distribution observed at room and higher temperatures. This destroys the nanostructure and results in loss of physical and mechanical properties. Surface passivation can increase stability by forming a protective coating against corrosion, which is increased due to the high surface area of nanomaterials.[31] Heat generation also affects the performance of the device; therefore, using optical spectroscopy, the thermal stability of semiconductor nanocrystals for photoluminescence was investigated. This was done for InP, Si, CdSe, and Mn:ZnCdS.[32-35]

II-VI Semiconductors (CdSe and CdS)

II-VI semiconductors are wide band gap materials displaying quantum confinement and tunable size dependent optical properties. Decreasing the size of the nanocrystals increases the band gap and shifts the absorbance and photoluminescence to lower wavelengths.[36] Due to these optoelectronic properties, II-VI semiconductors such as CdS and CdSe are proposed for applications such as photocatalysis, light emitting devices, flat panel displays, sensors, and solar cells.[36,37] The bulk band gap of CdSe is 1.74 eV (713 nm) and the band gap of CdS is 2.42 eV (515 nm).[38] The size of both of these can be tuned to absorb in the visible spectrum. Nanorods, with their elongated structure are heavily utilized for properties, such as generation of multiple excitons, emitting linearly polarized light, and large Stokes shift, which can decrease reabsorption of light.[4] For some applications of these materials, the environments are harsh and the structural stability in those situations has not been thoroughly investigated. Both the chemical (acidic, basic, oxidative, and reductive environments) and the thermal stability of II-VI nanorods,

specifically CdSe and CdS, are investigated in Chapter 2 along with reactivity with silica coating.

Metal Nitrides (From Metal Oxides)

Transition metal oxides are among the most extensively studied and characterized materials. They have been investigated at for various applications including renewable energy. Compared to metal oxides, metal nitrides are not as well understood or characterized. Recently, however, transition metal nitrides have received attention due to their properties of high melting points, hardness, and resistance to corrosion.[39] Furthermore, metal nitrides are interesting materials for a variety of applications. Compared to metal oxides, the conduction band (potential) stays the same but the valence bond forming orbital (2p) of nitrogen is higher in energy compared to the oxygen (2p) orbital, resulting in a higher oxidation potential.[40] Therefore, converting metal nitrides to oxides increases the valence band energy, resulting in a narrower band gap. Raising the valence energy band and narrowing the band gap impacts a material's optical, electronic and photocatalytic behavior. Therefore, others have studied using transition metal oxides as precursors to the nitrides.[41-43] We investigated this conversion (metal oxide to metal nitride) for copper(I) oxide nanocrystals and found interesting results. In Chapter 3, the facile conversion of copper(I) oxide to copper(I) nitride is investigated using two different nitrogen sources (ammonia and urea), along with the instability and decomposition of the nitride to copper(II) oxide at room temperature in humid conditions.

Methylammonium Lead Halides ($CH_3NH_3PbX_3$, where X = I, Br, or Cl)

A popular, new direction for photovoltaics is using semiconductor organometal halide perovskite materials. In 2009, a methylammonium lead halide perovskite produced a power conversion efficiency (PCE) of 3-4%.[44] Then in 2012, the PCE doubled with a reported PCE of

9.7% for a solid-state perovskite solar cell. In 2014, the perovskite solar cell reached a PCE of 19.3% and a certified PCE of 17.9% was shown. This performance increase was due to the high optical absorption, balanced charge transport, and long diffusion lengths of these perovskite materials.[45] Perovskites have a crystal structure of ABX_3 where A and B are two cations with different sizes and X is an anion, which is commonly oxygen or a halogen (Figure 3).[46] For organic-inorganic perovskite halides, A is an organic ammonium cation, B is Pb or Sn, and X is the halide.[47] The larger cation, A, occupies a cubo-octahedral site shared with 12 anions. The smaller B cations are in octahedral sites shared with 6 anions.[44] The perovskites studied at in Chapter 4 are $CH_3NH_3PbX_3$ (where X = I, Br, or Cl).
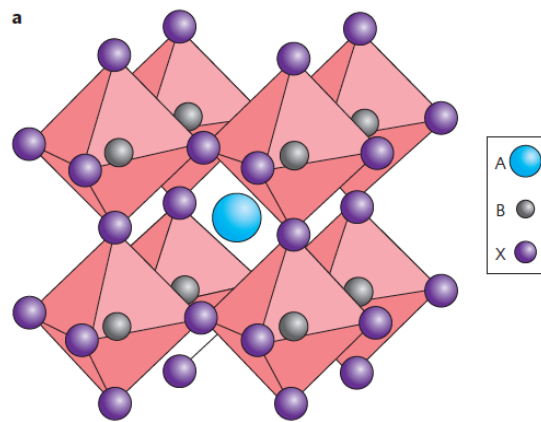

Figure 3. Cubic perovskite crystal structure where A is a large cation, B is a small cation, and X is an anion.[46]

The properties of these perovskite materials make them very interesting for applications in photovoltaics. For instance, $CH_3NH_3PbI_3$ has a band gap of 1.5 eV (820 nm) and is highly fluorescent.[48,49] Methylammonium lead bromide and chloride have a band gap of 2.3 eV (540 nm) and 3.1 eV (400 nm), respectively.[50,51] The red shift of the band gap from the chloride to iodide results from the increasing the covalent character of the lead-halide bond, which results in a decrease in electronegativity of the halide.[52,53] However, the stability of the perovskites is an

issue for solar cells. The materials decompose in high humidity and high temperature, which is unwanted in solar cells.[44,45] Recently, groups looked at different methods for long-term stabilization of the materials, such as using a carbon nanotube/polymer composite as a stable hole collection layer.[45,54] The perovskite solar cell showed a notable increase in moisture and thermal stability. Others looked at using a hole transport material free solar cell with a carbon back contact that showed an increased resistance to water.[45,55] However, the degradation mechanism of the perovskite is not yet understood, which would help improve the long-term stability of perovskite solar cells. Therefore, in Chapter 4, we investigated the thermal decomposition of bulk perovskite methylammonium lead halides to help determine a pathway which could lead to synthesizing more stable perovskite materials for use in solar cells.

Thesis Organization

This thesis discusses the chemical and thermal stability of the semiconductor materials to investigate how the different compositions and structures (both nano and bulk) of materials would react within different harsh environments (chemical and thermal) usually used for catalysis or solar cells. The following chapters contain a diverse range of materials and relevant literature is reviewed to give background and important results in each introduction.

Chapter 2 describes the chemical and thermal stability of II-VI nanorods. We used acids, bases, oxidants, and reductants to see the effect on the CdSe nanorods. We used variable temperature powder XRD to explore the thermal stability of both CdSe and CdS nanorods. Chia-Cheng Lin performed the silica coating of the CdSe nanorods and CdSSe drumsticks to determine the reactivity of the different types of surfaces of II-VI nanocrystals. In Chapter 3, the transformation of copper(I) oxide to copper(I) nitride and the stability of the nitride, under normal conditions (room temperature and humid/dry environments), is investigated. Miles A.

White performed the DOS and band structure calculations for the three materials, Cu_2O, CuO, and Cu_3N, along with discussion of the enthalpic contributions to determine the products of the decomposition (ammonia and nitrogen). Finally, the thermal stability of $CH_3NH_3PbX_3$ where (X = I, Br, or Cl) was investigated in Chapter 4 to determine the decomposition pathway of the materials. Determining the decomposition products may lead to improved modification of the material, increasing the stability for use in solar cells. Long Men and Bryan Rosales synthesized and characterized the methylammonium lead halides.

References

[1] Etgar, L. *Materials* **2013**, *6*, 445–459.

[2] Atkins, P.; De Paula, J. Physical Chemistry. 2006, 8th ed., 723.

[3] Atkins, P.; Overton, T.; Rourke, J.; Weller, M.; Armstrong, F. Shriver & Atkins' Inorganic Chemistry. 2010, 5th ed., 104.

[4] Smith, A.; Nie, S. *Acc. Chem. Res.* **2010**, *43*, 190–200.

[5] Kilmov, V. *Los Alamos Science* **2003**, *28*, 214–220.

[6] Andersen, K.; Fong, C.; Pickett, W. *J. Non-Cryst. Solids* **2002**, 299-302, 1105–1110.

[7] Yoffe, A. D. *Adv. Phys.* **1993**, *42*, 173–266.

[8] Yoffe, A. D. *Adv. Phys.* **2001**, **50**, 1–208.

[9] Koole, R.; Groeneveld, E.; Vanmaekelbergh, D.; Meijerink, A.; de Mello Donegá, C. "Size Effects on Semiconductor Nanoparticles" in *Nanoparticles: Workhorses of Nanoscience*, Ed. de Mello Donegá, C., Springer, 2014, pp 13–751.

[10] Suresh, S. Nanoscience and nanotechnology **2013**, 3, 62–74.

[11] Buhro, W. E.; Colvin, V. L. *Nature Materials* **2003**, *2*, 138–139.

[12] Shabaev, A.; Efros, A. L. *Nano Lett.* **2004**, *4*, 1821–1825.

[13] Hu, J. T.; Li, L. S.; Yang, W. D.; Manna, L.; Wang, L. W.; Alivisatos,A. P. *Science* **2001**, *292*, 2060–2063.

[14] Li, L.; Hu, J.; Yang, W.; Alivisatos, A. P. *Nano Lett.* **2001**, *1*, 349–351.

[15] Zhu, H.; Lian, T. *J. Am. Chem. Soc.* **2012**, *134*, 11289–11297.

[16] Park, J.; Joo, J.; Kwon, S.; Jang, Y.; Hyeon, T. *Angew. Chem. Int. Ed.* **2007**, 26, 2–33.

[17] Talapin, D.; Lee, J.; Kovalenko, M.; Shevchenko, E. *Chem. Rev.* **2010**, 110, 389–458.

[18] Giménez, S.; Lana-Villarreal, T.; Gómez, R.; Agouram, S.; Muñoz-Sanjosé V.; Mora-Seró I. *J. Appl. Phys.* **2010**, 108, 064310.

[19] González-Pedro, V.; Xu, X.; Mora-Seró, I.; Bisquert, J. *ACS Nano* **2010**, *4*, 5783–5790.

[20] Biju, V.; Itoh, T.; Anas, A.; Sujith, A.; Ishikawa, M. *Anal. Bioanal. Chem.* **2008**, 391, 2469–2495.

[21] Yong, K.; Roy, I.; Law, W.; Hu, R. *Chem. Commun.* **2010**, 46, 7136–7138.

[22] Cates, E. L.; Chinnapongse, S. L.; Kim, J.-H.; Kim, J.-H. *Environ. Sci. Technol.* **2012**, *46*, 12316–12328.

[23] Su, Y.-W.; Lin, W.-H.; Hsu, Y.-J.; Wei, K.-H. *Small* **2014**, *10*, 4427–4442.

[24] Wilker, M. B.; Schnitzenbaumer, K. J.; Dukovic, G. *Isr. J. Chem.* **2012**, *52*, 1002–1015.

[25] Kamat, P. V. *J. Phys. Chem. C* **2008**, *112*, 18737–18753.

[26] Hillhouse, H. W.; Beard, M. C. *Curr. Opin. in Colloid Interface Sci.* **2009**, *14*, 245–259.

[27] Andrievski, R. A. *J. Mater. Sci.* **2003**, *38*, 1367–1375.

[28] Andrievski, R. A. *Materials Science Forum* **2005**, *494*, 113–120.

[29] Andrievski, R. A. Mater. Res. Soc. Symp. Proc. **2014**, 1645.

[30] Andrievski, R. A. *Physics-Uspekhi* **2014**, *57*, 945–958.

[31] Andrievski, R. A. *J. Mater. Sci.* **2014**, *49*, 1449–1460.

[32] Rowland, C. E.; Hannah, D. C.; Demortiere, A.; Yang, J. H.; Cook, R. E.; Prakapenka, V. B.; Kortshagen, U.; Schaller, R. D. *ACS Nano* **2014**, *8*, 9219–9223.

[33] Rowland, C. E.; Liu, W. Y.; Hannah, D. C.; Chan, M. K. Y.; Talapin, D. V.; Schaller, R. D. *ACS Nano* **2014**, *8*, 977–985.

[34] Hannah, D. C.; Dunn, N. J.; Ithurria, S.; Talapin, D. V.; Chen, L. X.; Pelton, M.; Schatz, G. C.; Schaller, R. D. *Phys. Rev. Lett.* **2011**, *107*, 177403.

[35] Zheng, J.; Cao, S.; Wang, L.; Gao, F.; Wei, G.; Yang, W. *RSC Adv.* **2014**, *4*, 30938–30952.

[36] Alivisatos, A. P. *J. Phys. Chem. C* **1996**, *100*, 13226–13239.

[37] Wang, J.; Isshiki, M. "Wide-Bandgap II-VI Semiconductors: Growth and Properties" in *Springer Handbook of Electronic and Photonic Materials*, Springer, 2007, pp 325–342.

[38] Berger, L. I. "Properties of Semiconductors" in *CRC Handbook of Chemistry and Physics 95th Edition*, CRC Press, Taylor & Francis, Boca Raton, FL, 2014-2015, http://www.hbcpnetbase.com (accessed March 30, 2015).

[39] Dong, S.; Chen, X.; Zhang, X.; Cui, G. *Coordination Chemistry Reviews* **2013**, *257*, 1946–1956.

[40] Ho, C-T.; Low, K.-B.; Klie, R. F.; Maeda, K.; Domen, K.; Meyer, R. J.; Snee, P. T. *J. Phys. Chem. C* **2011**, *115*, 647–652.

[41] Buha, J.; Djerdj, I.; Antonietti, M.; Niederberger, M. *Chem. Mater.* **2007**, *19*, 3499–3505.

[42] Bilecka, I.; Niederberger, M. *Electrochimica Acta* **2010**, *55*, 7717–7725.

[43] Niederberger, M.; Buha, J.; Djerdj, I. *Mater. Res. Soc. Symp. Proc.* **2008**, *1007*, 213–221.

[44] Park, N.-G. *Materials Today* **2015**, *18*, 65–72.

[45] Jung, H. S.; Park, N.-G. *Small* **2015**, *11*, 10–25.

[46] Green, M. A.; Ho-Baillie, A.; Snaith, H. J. *Nature Photonics* **2014**, *8*, 506–514.

[47] Jeon, N. J.; Noh, J. H.; Yang, W. S.; Kim, C. Y.; Ryu, S.; Seo, J.; Seok, S. *Nature* **2015**, *517*, 476–480.

[48] Etgar, L.; Gao, P.; Xue, Z.; Peng, Q.; Chandiran, A. K.; Liu, B.; Nazeeruddin, M. K.; Grätzel, M. *J. Am. Chem. Soc.* **2012**, *134*, 17396–17399.

[49] Stoumpos, C. C.; Malliakas, C. D.; Kanatzidis, M. G. *Inorg. Chem.* **2013**, *52*, 9019–9038.

[50] Edri, E.; Kirmayer, S.; Cahen, D.; Hodes, G. *J. Phys. Chem. Lett.* **2013**, *4*, 897–902.

[51] Mosconi, E.; Amat, A.; Nazeeruddin, M. K.; Grätzel, M.; Angelis, F. D. *J. Phys. Chem. C* **2013**, *117*, 13902–13913.

[52] Huang, L.-Y.; Lambrecht, W. R. L. *Phys. Rev. B* **2013**, *88*, 165203-1–12.

[53] Gao, P.; Grätzel, M.; Nazeeruddin, M. K. *Energy Environ. Sci.* **2014**, *7*, 2448–2463.

[54] Habisreutinger, S. N.; Leijtens, T.; Eperon, G. E.; Stranks, S. D.; Nicholas, R. J.; Snaith, H. J. *Nano Lett.* **2014**, *14*, 5561–5568.

[55] Mei, A.; Li, X.; Liu, L.; Ku, Z.; Liu, T.; Rong, Y.; Xu, M.; Hu, M.; Chen, J.; Yang, Y.; Grätzel, M.; Han, H. *Science* **2014**, *345*, 295–298.

CHAPTER 2

HOW ROBUST ARE SEMICONDUCTOR NANORODS? INVESTIGATING THE STABILITY AND CHEMICAL DECOMPOSITION PATHWAYS OF PHOTOACTIVE NANOCRYSTALS

Malinda D. Reichert, Chia-Cheng Lin, Javier Vela

Abstract

Anisotropic II-VI semiconductor nanostructures are important photoactive materials for various energy conversion and optical applications. However, aside from the many available surface chemistry studies and from their ubiquitous photo degradation under continuous illumination, the general chemical reactivity and thermal stability (phase and shape transformations) of these materials are poorly understood. Using CdSe nanorods and CdS nanorods as model systems, we have investigated the behavior of II-VI semiconductor nanorods against various conditions of "extreme" chemical and physical stress (acids, bases, oxidants, reductants, heat). CdSe nanorods react rapidly with acids, becoming oxidized to Se or SeO_2. In contrast, CdSe nanorods remain mostly unreactive when treated with bases or strong oxidants, although bases do partially etch the tips of the nanorods (along their axis). Roasting (heating in air) of CdSe nanorods results in rock salt CdO, but neither CdSe nor CdO are easily reduced by hydrogen (H_2). Another reductant, n-BuLi, reduces CdSe nanorods to metallic Cd. Variable temperature X-ray diffraction experiments show axial annealing and selective axial melting of the nanorods precede particle coalescence. Furthermore, thermal analysis shows that the axial melting of II-VI nanorods is a ligand dependent process. In agreement with chemical reactivity

and thermal stability observations, silica-coating experiments show that the sharpest (most curved) II-VI surfaces are most active against heterogenous nucleation of a silica shell. These results provide valuable insights into the fate and possible ways to enhance the stability and improve the use of II-V semiconductor nanostructures in the fields of optics, magnetism and energy conversion.

Introduction

II-VI semiconductor nanostructures are among the most hyped materials to date. Photophysics studies of CdSe, CdS, etc. have blanketed the scientific literature for the past thirty years, and numerous applications in energy conversion devices (photovoltaics, light emitting devices, etc.) have followed. In comparison, we know relatively little about the general chemical and thermal stability of low dimensional II-VI semiconductors. What little we know comes mostly from surface chemistry studies or from indirect observations related to the apparent instability and photo-degradation of these materials under continuous illumination, as described in many photocatalytic studies.

Semiconductors are known to undergo photoinduced oxidative etching and degradation under continuous illumination,[1,2] often in detriment of their photocatalytic properties.[3-10] Photocatalytic reactions tend to occur under relatively harsh, oxidative, reductive, acidic or basic conditions, contributing to the degradation process.[11-13] Amine-passivated, wurtzite CdSe platelets photodegrade faster than carboxylate-passivated, zinc-blende CdSe nanoplatelets.[14] Nanocrystals with incompletely passivated surfaces degrade the fastest.[15] Photopassivation, photooxidation, and photo introduction of defects occur in CdSe/CdS dot-in-rod nanoparticles.[16] Ways to prevent semiconductor photodegradation include hole scavenging with stoichiometric reagents such as sulfide (S^{2-}).[17] Additive-free methods include metal and metal-oxide

modification: SC-M heterostructures are more robust to photodegradation than unmodified SCs,[18,19] likely due to electron-transfer between the SC and M components.[20-22] Decoration of CdS nanorods with MFe_2O_4 (M = Zn or Co) also results in photochemically stable and magnetically recyclable photocatalysts.[23,24]

Beyond these numerous straightforward photocatalytic observations, relatively little is known about the general chemical and thermal stability, degradation and reactivity of semiconductor nanorods in the presence of different reagents and/or "extreme" conditions. Tributylphosphine shortens the length of CdSe nanorods, nanowires and tetrapods through axial etching. When accompanied by photoirradiation, tributyphosphine and primary amines decrease nanocrystal diameter.[25] Encapsulation in dendron boxes makes CdSe/CdS core/shells more stable against H_2O_2, HCl, UV irradiation in air and mild heating under vacuum.[26] Aminosilane modification improves the chemical stability of ZnO nanorods in HCl solution.[27] "Roasting" (heating in air) of GaP nanocrystals produces Ga_2O_3 hollow particles, nanorods or nanotubes, depending on the specific heating rate and final heating temperature.[28] Roasting of GaN results in single-crystalline β-Ga_2O_3 nanowires and zigzag- nanostructures.[29] Heating and adding acids corrode $GeSe_4$ glasses to produce Se nanoparticles.[30] In the case of metals, it is known that the chemical and thermal stability of nano gold correlates with nanoparticle size and morphology.[31,32] Gold nanorods undergo anisotropic chemical dissolution (axial etching) when treated with cyanide, and are selectively shortened when treated with oxygen in HCl solution.[33] Small aspect ratio silver nanorods are unstable in air and light, likely due to photooxidation. However, Ag nanowires are relatively stable under similar conditions.[34]

Low dimensional nanostructures undergo melting and other phase transformations at much lower temperatures than their bulk counterparts. Examples include: ZnO nanorods (750

°C) *vs.* bulk ZnO (1976 °C);[35] CdSe nanorods (460–470 °C) *vs.* bulk CdSe (1239 °C); Ge nanowires (650–800 °C) vs. bulk Ge (930 °C);[36] Cu nanowires (450 °C) *vs.* bulk Cu (1083 °C);[37] and RuO$_2$ nanorods (600–650 °C) *vs.* bulk RuO$_2$ (1200 °C).[38,39] Additional relevant examples based on detailed thermal stability analyses have been reported for CdSe,[40,41] CdS and SnS nanocrystals,[42-44] CdSe/CdS octapods,[45] PbS nanorods,[46] Au nanorods,[47,48] Au-tipped CdS nanorods,[49] and layered inorganic (II-VI)–organic (ethylenediamine) nanostructures.[50] Beyond experiments, molecular dynamics (MD) simulations predict heating-induced formation of anisotropic CdSe nanostructures at 600–1000 K.[51] MD simulations also predict the melting point of Ni nanorods decreases with diameter, regardless of length. MD simulations on Pd, Au, Zr, Ni and Ti nanowires are also available.[52] Nanocrystals have also been shown to undergo cation exchange.[53]

Several surface chemistry studies have used X-ray photoelectron spectroscopy (XPS) to probe the inorganic-organic interface of nanosized II-VI semiconductors under a variety of conditions. XPS studies showed that CdO and SeO$_2$ form on CdSe quantum dot surfaces, particularly under illumination.[54-57] Upon exposure to H$_2$O$_2$, SeO$_2$ and CdSO$_4$ form on CdSe and CdS dot surfaces, respectively (and an increase in CdS photoluminescence).[58,59] CdCl$_3^-$, Se$_x^-$ clusters, and SeH$_x^-$ species form on CdSe nanorod surfaces in the presence of chloromethane solvents.[25] In the majority of these cases, the new surface species were either produced in very small enough or were amorphous, and thus undetectable by XRD. Phase and shape tranformations of the whole nanocrystals under similar or even more "extreme" conditions were not usually addressed.

In view of the perceived lack of substantive and systematic reports on the chemical and thermal stability of II-VI semiconductor nanocrystals, and because of their great importance and

widespread interest and applicability as photoactive materials for optics, magnetism and energy conversion, we decided to study their overall stability in detail. In this paper, we specifically focus our attention on one-dimensional (1D) nanocrystals (nanorods) of CdSe and CdS as model systems.

Experimental

Materials. Selenium (99.999%), cadmium oxide (99.998%), sulfur (99.999%), tetramethylammonium hydroxide (TMAH) (98%) and diphenylpropyl phosphine (DPP) were purchased from Alfa Aesar; octadecylphosphonic acid (ODPA) from PCI Synthesis; 1-octadecene (ODE) (90%) from Acros Organics; trioctylphosphine oxide (TOPO) (99%), n-butyllithium (1.6 M in hexanes), tetraethyl orthosilicate (TEOS) (98%), Igepal CO-520, ammonium hydroxide (NH_4OH) (28 wt%) from Aldrich; trioctylphosphine (TOP) (97%) from Strem; hydrochloric acid, nitric acid, potassium permanganate, hydrogen peroxide (30% w/w), sodium hydroxide, ethanol (200 proof), and hexane from Fisher. All chemicals were used as received unless specified otherwise.

II-VI Nanorod Synthesis. *CdSe nanorods*, and *CdS nanorods*, and compositionally-graded, *$CdS_{0.4}Se_{0.6}$ drumstick-like nanorods* were made by literature procedures (see Supporting Information file).[60-63]

Chemical Reactivity Studies. *Acids and bases.* Freshly made and purified CdSe nanorods (15-20 mg) (and/or in some cases, CdS nanorods, see Supporting Information for details) were allowed to dry overnight. 20 mL aqueous 4 M acid (HCl or HNO_3) or 4 M base (NaOH or Me_4NOH) was added and the mixture stirred for 3 days at room temperature (R.T.). *Warning*: Acid digestion of CdSe could potentially release H_2Se, which is highly toxic. These and similar reactions should be carried inside a fume hood with other appropriate engineering

controls and while wearing personal protective equipment. *Oxidants: KMnO₄.* Freshly made and purified CdSe nanorods (15-20 mg) were allowed to dry overnight. 20 mL aqueous 0.2 M KMnO₄ was added and the mixture stirred for 3 days at R.T. *Oxidants: H₂O₂.* Freshly made and purified CdSe nanorods (15-20 mg) were allowed to dry overnight. 10 mL aqueous 30% w/w H₂O₂ were added and the mixture stirred for 1 day at R.T. Two additional additions of 5 mL aqueous 30% w/w H₂O₂ each were added after 1 and 2 day reaction, and stirring continued for a total of 3 days at R.T. *Oxidants: O₂ (Air).* Freshly made and purified CdSe nanorods (15-20 mg) were allowed to dry overnight, placed in a combustion boat and inside a tube furnace (Lindberg 55035). Air, dried through a Drierite tube, was passed (60 mL/min) while heating to 350 °C, 500 °C or 600 °C at a rate of 10 °C/min, and kept at this temperature for a period of time (see below). *Reductants: H₂.* Freshly made and purified CdSe nanorods (or CdO) (15-20 mg) were allowed to dry overnight, placed in a combustion boat and inside a tube furnace (Lindberg 55035). H₂ (20% v/v in Ar) was passed (60 mL/min) while heating at a rate of 10 °C/min (see Supporting Information). *Reductants: n-BuLi.* 10 mL CdSe nanorod solution (optical density ~0.69 at λ = 650 nm) in ODE was added to a three neck round bottom flask and degassed under dynamic vacuum at 80 °C for 20 min. The flask was refilled with argon, heated to a given temperature (25 °C, 100 °C, or 300 °C), n-butyllithium (0.5 mL in 0.5 mL ODE) injected, and the mixture stirred for 1 h.

Silica Coating. CdSe or CdS₀.₄Se₀.₆ nanorods were washed once with a mixture of toluene and methanol (1:5 v/v ratio). *CdSe/SiO₂.* 3 mL CdSe nanorod solution (6×10⁻⁵ M in hexane), 0.8 g Igepal CO-520 and 9.5 mL hexane were mixed and stirred at room temperature (R.T.) for 30 min. 0.1 mL aqueous NH₄OH (28% w/w) was added and stirring continued for 15 min. 0.1 mL TEOS was added and the solution further stirred for 1 h. Particles were precipitated

by adding 10 mL methanol and centrifuged 5 min at 5000 rpm. Particles were re-dispersed in 5 mL ethanol, centrifuged 5 min at 10000 rcf, and this washing procedure repeated once. *CdS$_{0.4}$Se$_{0.6}$/SiO$_2$*. 0.1 mL CdS$_{0.4}$Se$_{0.6}$ nanorod solution (2×10^{-2} M in toluene), 0.8 g Igepal CO-520 and 12.5 mL hexane were mixed and stirred at R.T. for 30 min. 0.1 mL NH$_4$OH (28% w/w) was added and stirring continued for 15 min. 0.1 mL TEOS was added and the solution further stirred for 1 h. Particles were precipitated by adding 10 mL methanol and centrifuged 5 min at 5000 rpm. Particles were re-dispersed in 5 mL ethanol, centrifuged 5 min at 10000 rcf, and this washing procedure repeated once.

Optical Characterization. Absorption spectra were measured with a photodiode array Agilent 8453 UV-Vis spectrophotometer. Solvent absorption was subtracted from all spectra. Steady-state photoluminescence (PL) spectra were measured with a Horiba-Jobin Yvon Nanolog scanning spectrofluorometer equipped with a photomultiplier detector.

Structural Characterization. *X-Ray Diffraction.* Powder X-ray diffraction (XRD) data were measured using Cu Kα radiation on a Rigaku Ultima U4. *Transmission Electron Microscopy.* TEM was conducted on carbon-coated copper grids using a FEI Technai G2 F20 field emission scanning transmission electron microscope (STEM) at 200 kV (point-to-point resolution <0.25 nm, line-to-line resolution <0.10 nm). *Particle analysis.* Dimensions were measured manually and/or with ImageJ. Size measurements and particle statistics were obtained for at least >100 particles. Average sizes are reported along ± standard deviations.

Thermal Stability Studies. *VT XRD.* Variable temperature (R.T. to 700 °C) XRDs were measured under an inert atmosphere (He or Ar) using Cu Kα radiation on a Philips PANalytical XRD. Individual XRD peak widths at half maximum intensity (FWHM, denoted β) were measured by modeling the experimental data using Origin or KaleidaGraph. The results were

used to calculate single crystalline (ordered) domain sizes (τ) along the main crystallographic directions using the Scherrer equation, $\tau = K \times \lambda / (\beta \times \cos\theta)$, where the shape factor K was assumed to be 0.9, λ is the X-ray wavelength (Cu Kα = 0.154 nm), and θ is the diffraction (Bragg) angle. *Differential Thermal Analysis*. DTA was performed using a PerkinElmer DTA 7 on ~20 mg samples at a heating rate of 10 °C/min. *Thermogravimetric Analysis*. TGA was performed using a PerkinElmer TGA 7 on ~0.5 mg samples and at a heating rate of 10 °C/min.

Results and Discussion

Reactivity of II-VI semiconductor nanorods against acids: Chalcogenide oxidation. We began our investigation by probing the reactivity of CdSe nanorods against common acids, specifically HCl and HNO_3 (equation **1**, Table 1's entries 1 and 2). Powder X-ray diffraction (XRD) shows that, after 3 days stirring with 4 M HCl at room temperature (R.T.), the main crystalline product is elemental selenium (Se^0), although some CdSe remains (Figure 1a). Transmission electron microscopy (TEM) reveals that the newly formed Se^0 is made of elongated nanoparticles with a rod-like morphology; however, these Se^0 nanorods (282±118 nm × 20±8 nm) are significantly larger than the original CdSe nanorods (18±2 nm × 7±1 nm) (Figure 1b and Table 1). Optical spectroscopy shows that the absorption fine structure and band edge photoluminescence (675 nm PL) characteristic of the original CdSe nanorods disappears within the first 12 h of reaction, strongly suggesting that chalcogenide oxidation (from Se^{2-} in CdSe to Se^0) occurs relatively fast (Figure 1c). When we used HNO_3 instead of HCl, we observed a very similar behavior. However, the more oxidizing HNO_3 acid leads to the formation of crystalline SeO_2 in addition to Se^0, as evidenced by powder XRD (Figure 1a and Supporting Information Figure S1).

$$\text{CdSe} + \text{4M Acid} \xrightarrow[\text{3 day}]{\text{RT}} \text{Se}^0 + \text{SeO}_2 \qquad (\textit{unbalanced}) \quad \textbf{(1)}$$
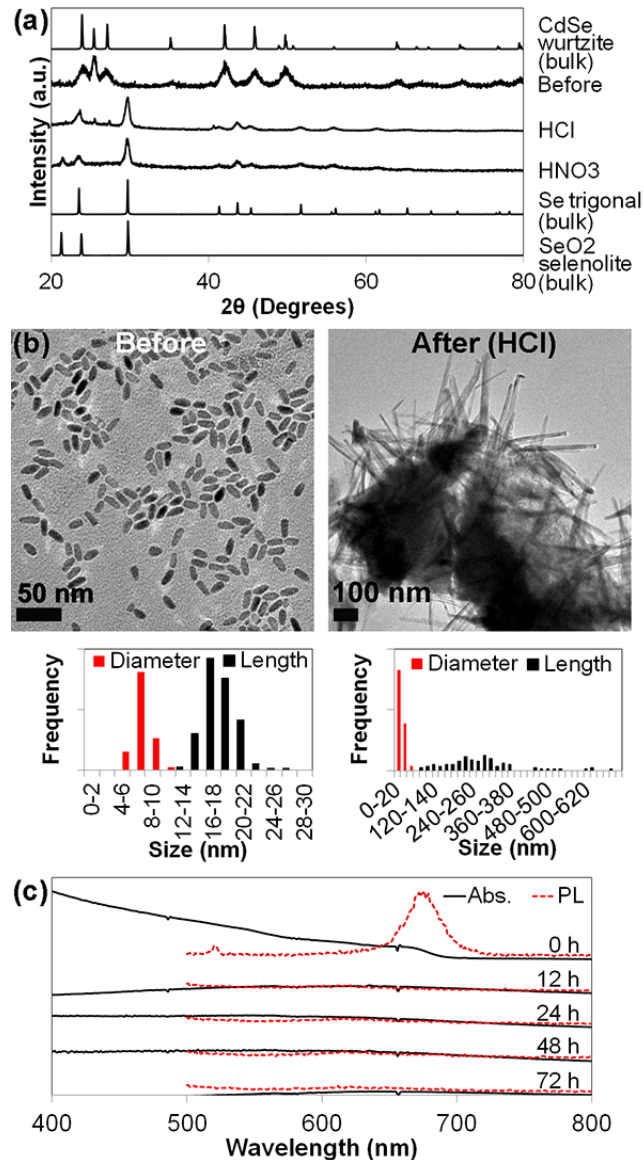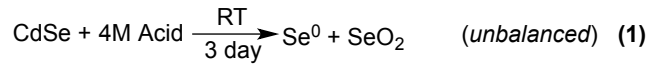

Figure 1. Reactivity of CdSe nanorods against acids: (a) Powder XRD patterns before and after treatment with aqueous 4M HCl or HNO$_3$ at R.T. for 3 days. (The standard XRD patterns for "bulk" wurtzite CdSe, trigonal Se, and selenolite SeO$_2$ are shown for comparison) (b) Representative TEM images and size histograms, and (c) time evolution of absorption and emission spectra before and after treatment with aqueous 4M HCl at R.T. for 3 days.

Table 1. Effect of common chemical reagents on CdSe nanorods.

Entry #	Reactants	Conditions	Before Length/Diameter (nm)		After Length/Diameter (nm)		Aspect Ratio	Observed XRD Phases
1	CdSe, HCl	RT, 3 days	18±2	7±1	282±118	20±8	14	CdSe, Se
2	CdSe, HNO$_3$	RT, 3 days	18±2	7±1	600±332	24±12	25	Se, SeO$_2$
3	CdSe, NaOH	RT, 3 days	20±2	5±1	16±2	5±1	3	CdSe, Se, CdO
4	CdSe, Me$_4$NOH	RT, 3 days	18±2	7±1	14±2	6±1	2	CdSe, Se, CdO
5	CdSe, KMnO$_4$	RT, 3 days	10±1	5±1	9±1	4±1	2	CdSe (NR)
6	CdSe, H$_2$O$_2$	RT, 3 days	27±3	6±1	29±3	7±1	4	CdSe (NR)
7	CdSe, O$_2$	600 °C, 4 h	23±2	7±1	50^a	50^a	4	CdO
8	CdO, H$_2$	300 °C, 4 h	30^a	30^a	35^a	35^a	1	CdO
9	CdSe, H$_2$	500 °C, 2 h	20±2	6±1	20^a	25^a	3	CdSe (NR)
10	CdSe, n-BuLi	300 °C, 1 h	23±2	7±1	50^a	50^a	4	Cd

^{a}Estimated from XRD peak widths. (RT = Room Temperature or 21 °C; NR = No Reaction)

Reactivity against bases: Axial etching. We next investigated the chemical reactivity of CdSe nanorods against two common bases, NaOH and tetramethylammonium hydroxide (Me$_4$NOH) (equation **2**, Table 1's entries 3 and 4). Powder XRD and TEM data show that stirring with 4 M NaOH or Me$_4$NOH at room temperature (R.T.) for 3 days results in partial axial etching, *i.e.* along the 002 set of planes (Figures 2 and S2). In XRD, this is evident by a decrease in intensity and widening of the 002 diffraction peaks relative to the 100 and 110 peaks (Figure 2a and Figure 3). TEM confirms that, upon treatment with 4 M NaOH, the diameter of the CdSe nanorods stays the same (5±1 nm), but their length decreases somewhat (from 20±2 nm to 17±2 nm) (Figure 2b and Table 1). Both NaOH and Me$_4$NOH result in similar partial etching, however Me$_4$NOH also results in the formation of small amounts of crystalline Se^0 and CdO, while NaOH does not (Figure 2a and S2a). Interestingly, this base-induced, axial etching does not affect the

absorption band edge of the CdSe nanorods, confirming that their diameter remains unchanged; however, the relative photoluminescence (PL) intensity decreases by about one order of magnitude, likely due to the introduction of surface defects (Figure 2c).
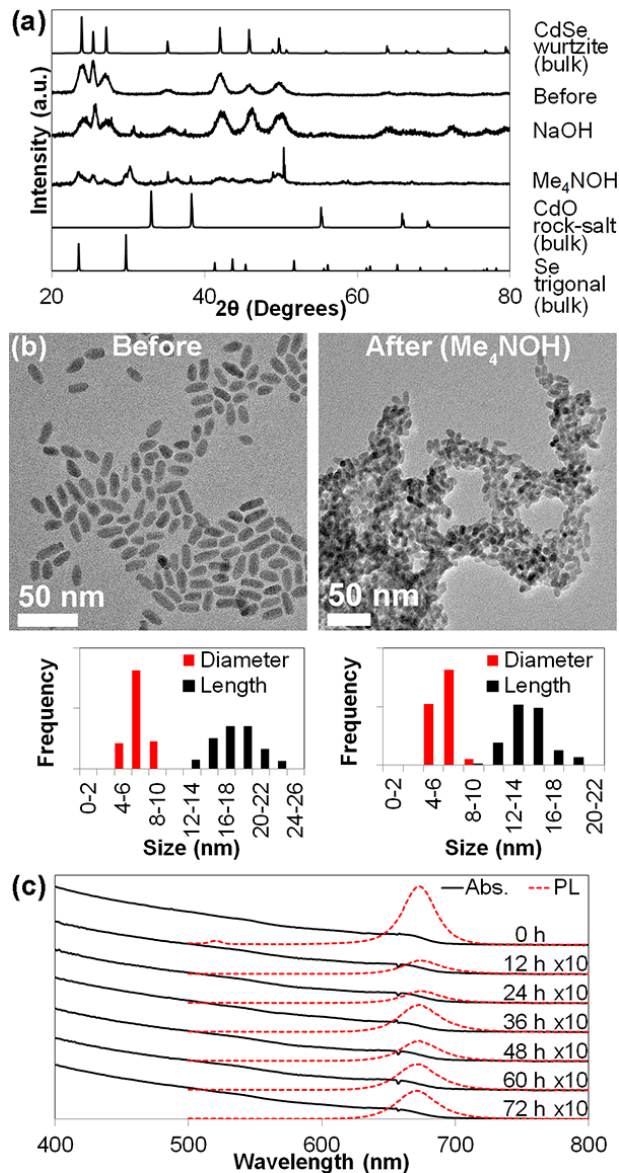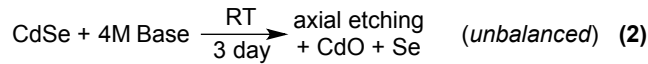
$$CdSe + 4M\ Base \xrightarrow[\text{3 day}]{RT} \text{axial etching} + CdO + Se \quad (\textit{unbalanced}) \quad (2)$$

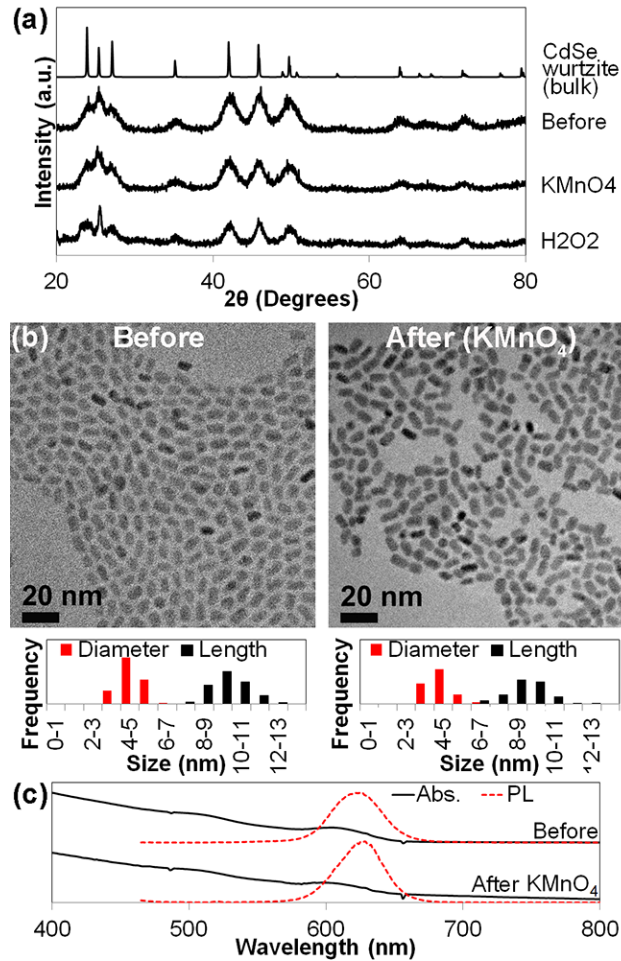**Figure 2.** Reactivity of CdSe nanorods against bases: (a) Powder XRD patterns before and after treatment with aqueous 4M NaOH or Me₄NOH at R.T. for 3 days. (The standard XRD patterns for "bulk" wurtzite CdSe, and trigonal Se are shown for comparison) (b) Representative TEM

images and size histograms, and (c) time evolution of absorption and emission spectra upon treatment with aqueous 4M Me$_4$NOH at R.T.

Relative stability against oxidants. To our surprise, CdSe nanorods appear to be relatively stable in the presence of strong oxidants such as KMnO$_4$ or H$_2$O$_2$ (equation **3**, Table 1's entries 5 and 6). There are no significant changes in the powder XRD, TEM or absorption and emission spectra of CdSe nanorods after stirring for 3 days over 0.2 M KMnO$_4$ at room temperature (R.T.) (Figure 4 and Table 1). Likewise, using H$_2$O$_2$ (30% w/w) under similar conditions does not change or impact the original crystalline structure (XRD), morphology (TEM) or absorption onset of the CdSe nanorods, although the relative PL intensity decreases significantly (Figure S3). This may be due to surface chemistry effects, undetectable by XRD but previously observed by XPS, such as the formation of amorphous and/or small amounts of CdO and SeO$_2$.[58,59]
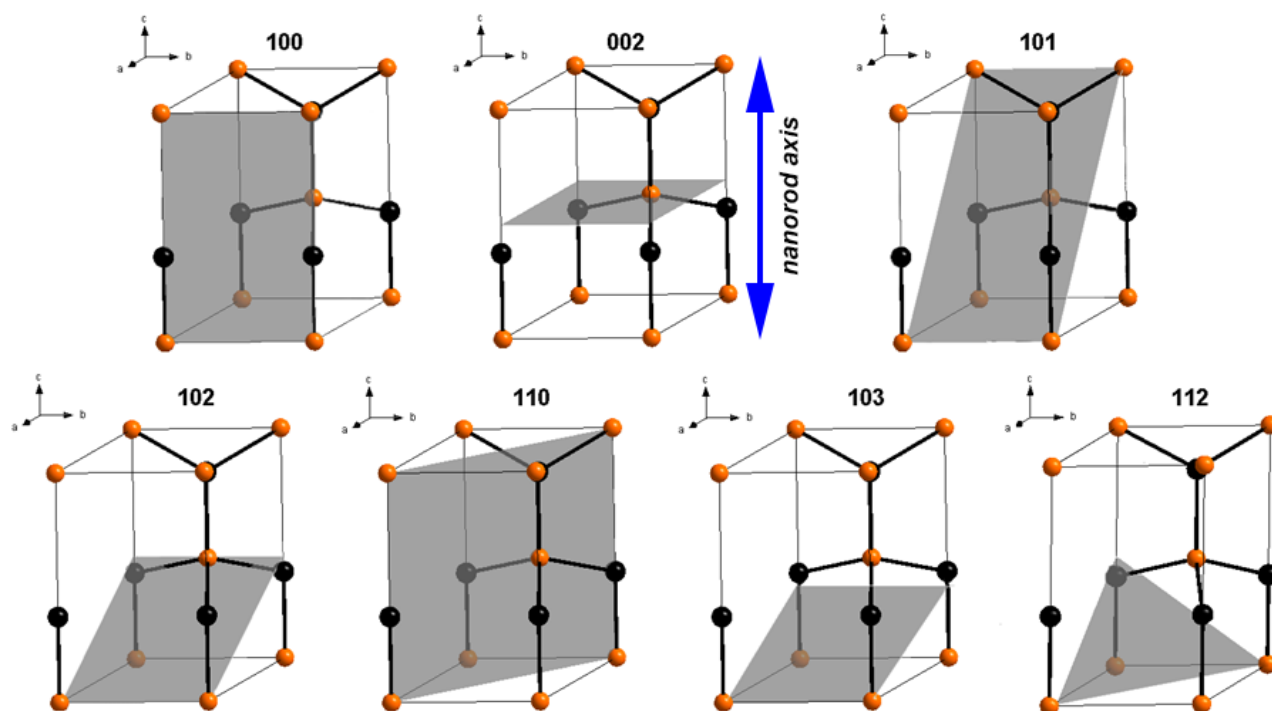
Figure 3. Main lattice planes for the wurtzite unit cell (adopted by hexagonal CdE, where E = S, Se).

Roasting. At elevated temperatures, CdSe nanorods react with oxygen from air to produce polycrystalline (bulk) CdO. As shown in Figure 5, CdSe particles are relatively stable up to 350 °C under air for long periods of time (see thermal stability and morphology discussion further below). However, all hexagonal (wurtzite) CdSe diffraction peaks narrow with continued heating, and a new set of peaks indexing for rock salt CdO appears at 600 °C. This transformation, which is complete after a few hours at 600 °C, closely resembles the "roasting" process used to isolate group II metals from II-VI chalcogenide ores (equation **4**, Table 1's entries 7 and 8). Roasting is commonly used in extractive metallurgy and is followed by reduction of the metal oxide (II-O) over hydrogen gas. In our case, we find that the polycrystalline CdO made by roasting CdSe nanorods does not easily react with a stream of H_2 (even at 300 °C for 4 h, Figure 5).

$$CdSe + Oxidant \xrightarrow[\text{3 day}]{\text{RT}} N.R \qquad\qquad (3)$$

Figure 4. Reactivity of CdSe nanorods against oxidants: (a) Powder XRD patterns before and after treatment with aqueous 0.2M KMnO$_4$ or 30% w/w H$_2$O$_2$ at R.T. for 3 days. (The standard XRD pattern for "bulk" wurtzite CdSe is shown for comparison) (b) Representative TEM images and size histograms, and (c) time evolution of absorption and emission spectra upon treatment with aqueous 0.2M KMnO$_4$ at R.T. for 3 days.
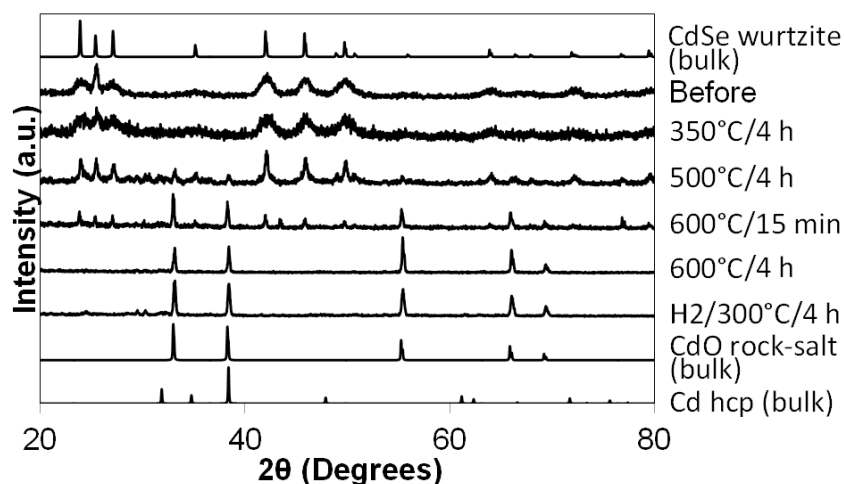
$$CdSe \xrightarrow[\Delta,\ t]{O_2\ (air)} CdO \xrightarrow[\Delta,\ t]{H_2/Ar} N.R. \qquad (unbalanced) \quad (4)$$
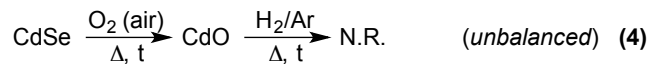
Figure 5. Reactivity of CdSe nanorods against oxidants: Powder XRD patterns showing the effect of O_2 (and moisture) from air upon heating at different temperatures. The polycrystalline (bulk) CdO product does not easily react with hydrogen (H_2) gas. (The standard XRD patterns for "bulk" wurtzite CdSe, rock-salt CdO, and hcp Cd are shown for comparison)

Reactivity against reductants. We also explored whether CdSe nanorods react with two common reducing agents, hydrogen and n-butyllithium. Upon treatment of CdSe nanorods with hydrogen gas (H_2/Ar) at 500 °C, XRD shows a narrowing of the individual diffraction peaks, indicating an increase in particle size (see Figure S5). However, CdSe remains as the only crystalline material, and there is no evidence of reduction, much like in the aforementioned CdO case (equation **5**, Table 1's entry 9). In contrast, CdSe nanorods react with n-butyllithium at 300 °C to form metallic Cd^0 (equation **6**, Table 1's entry 10). The sharpness of the peaks in the XRD pattern indicates the Cd^0 product is made up of large particles (Figure 6). Using reaction temperatures lower than 300 °C either did not enable reduction or resulted in incomplete reduction. The overall reactivity of CdSe nanorods against different common acids, bases, oxidants and reductants is summarized in Scheme 1.
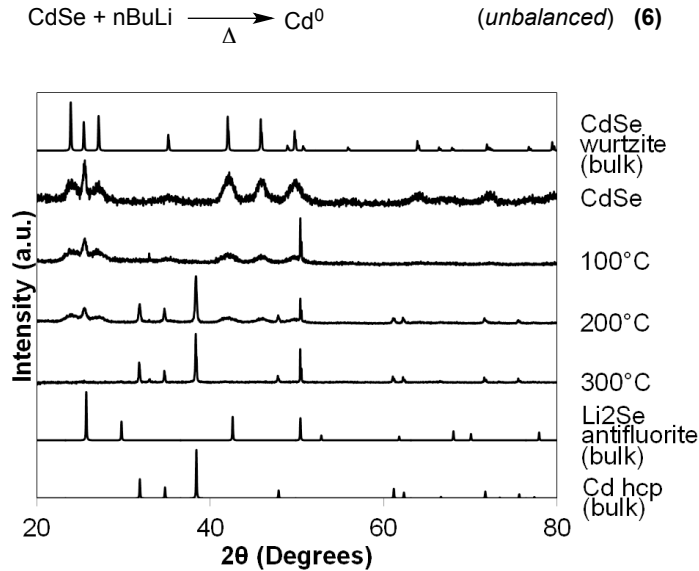
$$CdSe \xrightarrow[\Delta,\ t]{H_2/Ar} N.R. \qquad\qquad (\textit{unbalanced}) \quad \textbf{(5)}$$

$$CdSe + nBuLi \xrightarrow{\Delta} Cd^0 \qquad \textit{(unbalanced)} \quad \textbf{(6)}$$

Figure 6. Reactivity of CdSe nanorods against reductants: Powder XRD patterns of CdSe nanorods before and after treatment with n-butyllithium and subsequent heating to 100 °C, 200 °C, and 300 °C. (The peak at $2\theta = 51°$ is an unidentified impurity, possibly Li_2Se; the standard XRD patterns for "bulk" wurtzite CdSe, antifluorite Li_2Se, and hcp Cd are shown for comparison)
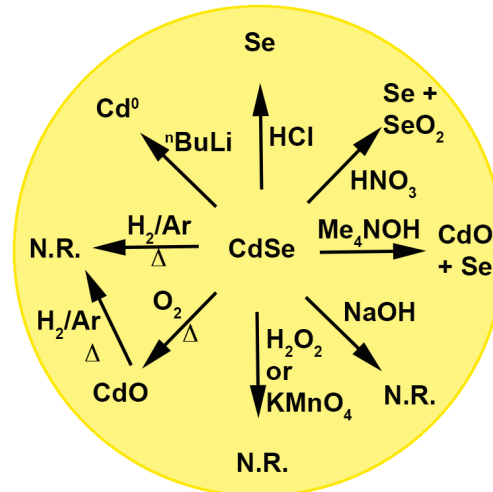
Scheme 1. Overall chemical reactivity of semiconducting CdSe nanorods against some common acids, bases, oxidants, and reductants (N.R. = no reaction).

Thermal stability of II-VI semiconductor nanorods: Selective axial melting precedes particle coalescence. As mentioned above, CdSe nanorods are compositionally stable upon

heating and this stability continues up to at least 700 °C, provided that the sample is maintained in an inert atmosphere (Ar or He). This is not immediately surprising because the melting temperatures reported for polycrystalline (bulk) CdSe and CdS are 1268 °C and 1750 °C, respectively. Nevertheless, nanostructured materials are well known to melt at temperatures well below those reported for their polycrystalline (bulk) counterparts (see above),[35-39] and II-VI nanorods are no exception; variable temperature (VT) or "hot stage" powder XRD data reveal orientation-selective melting and nanoparticle coalescence at temperatures as low as 300 °C and 500 °C, respectively. Figures 7 and 8 show stack plots of VT XRDs, individual diffraction peak widths, and corresponding single crystalline domain sizes obtained using the Scherrer equation for CdSe and CdS nanorods. At room temperature (R.T.), the nanorod-like morphology of the wurtzite (hexagonal) nanocrystals is evident by looking at how sharp the 002 XRD peak, corresponding to planes along the axial direction is in comparison to all the other, much wider peaks, particularly the orthogonal 100 or 110 directions (see Figure 3).
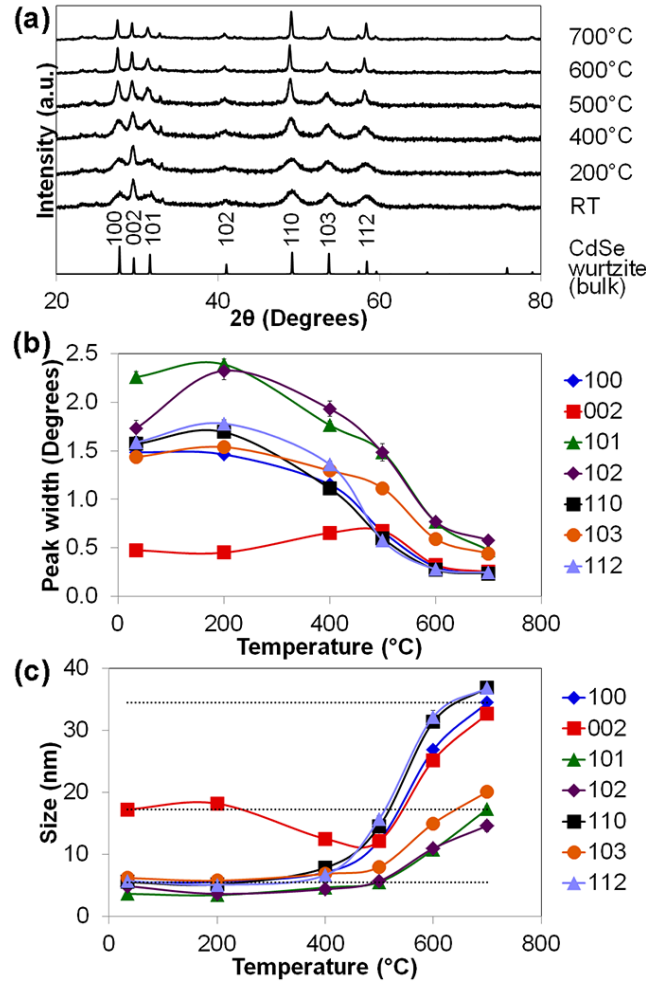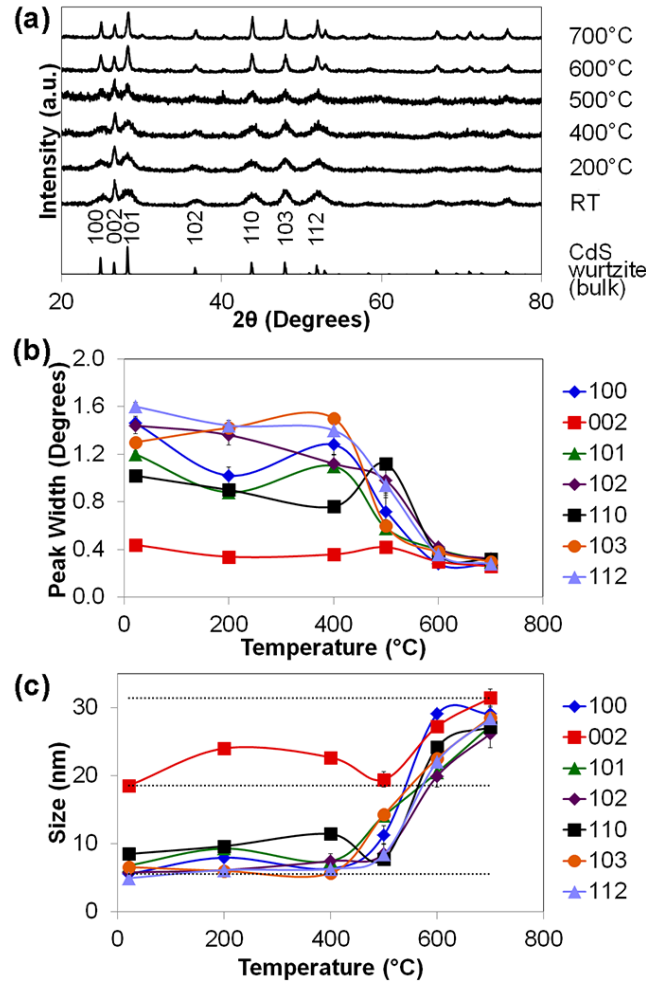
Figure 7. Thermal stability of CdSe nanorods: (a) Hot stage (VT) powder XRD patterns starting from room temperature to 700 °C. Corresponding (a) XRD peak widths and (c) crystallite sizes (Scherrer) for the main CdSe diffraction planes (wurtzite) as a function of temperature (dashed lines show the initial and final grain sizes of the 002 planes, and the initial size of the 100 or 101 planes). (Note: The peak at 2theta = 33 degrees corresponds to lava (aluminosilicate) sample holder; the standard XRD patterns for "bulk" wurtzite CdSe is shown for comparison)

Figure 8. Thermal stability of CdS nanorods: (a) Hot stage (VT) powder XRD patterns starting from room temperature to 700 °C. Corresponding (a) XRD peak widths and (c) crystallite sizes (Scherrer) for the main CdS diffraction planes (wurtzite) as a function of temperature. (The standard XRD patterns for "bulk" wurtzite CdS is shown for comparison)

Careful inspection of how the peak widths (Figures 7b and 8b) and single crystalline domain sizes change with temperature (Figures 7c and 8c) shows that *II-VI nanorods respond to heating in three well defined stages* (Scheme 2): *(i) Annealing*: Heating between R.T. and 200 °C increases the single crystalline domain size along (perpendicular to) the 002 planes by 1-5 nm. This is most likely due to the extrusion of defects and elimination of stacking faults along the axis of the nanorods.[47,48,64] Interestingly, the longer and higher aspect ratio CdS nanorods show

the steepest annealing. *(ii) Axial melting*: Continued heating between 200 °C and 500 °C causes the single crystalline domain size along the 002 planes to collapse by 5-10 nm. This clearly indicates that melting along the axial direction precedes melting on any other directions. *(iii) Coalescence*: Additional heating above 500 °C and up to 700 °C increases the grain sizes along all directions. Similarly to axial melting, coalescence appears to be an orientation-dependent phenomenon for CdSe nanorods, with the 100, 002, 110 and 112 peaks narrowing faster than the 101, 102 and 103 peaks (Figure 7c). In contrast, coalescence occurs at similar rates along all crystallographic planes in the case of CdS nanorods, before reaching a plateau at around 700 °C (Figure 8c).
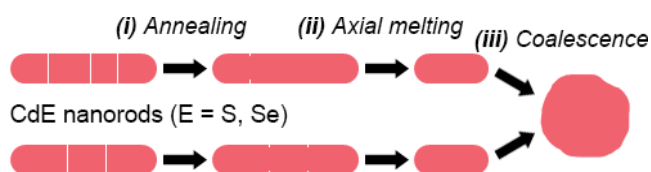
Scheme 2. Temperature dependent behavior of CdS and CdSe nanorods: (i) Annealing of axial defects (R.T. to 200 °C), (ii) axial melting (200 °C to 500 °C), and (iii) particle coalescence (500 °C to 700 °C and above).

We were surprised that the change from selective axial melting to particle coalescence occurs at very similar temperatures (*ca.* 500 °C) for both CdSe and CdS nanorods. To better understand this, we conducted differential thermal analysis (DTA) and thermogravimetric analysis (TGA) on both samples (Figure 9). The first DTA heating cycle shows *two clear endothermic transitions: (1st)* A large and well-defined endotherm peaking at 500-510 °C that we ascribe to axial melting, thus lowering the aspect ratio of the nanorods and in accordance with our XRD observations above. Interestingly, the longer and higher aspect ratio CdS nanorods show the steepest axial melting endotherm. *(2nd)* A broader, less defined endotherm between 580-730 °C that we ascribe to particle coalescence. As expected, these two melting transitions are

irreversible because after they occur, the resulting particles are much larger and are expected to melt at higher temperatures (closer to bulk). Consequently, the second DTA heating cycle shows the samples no longer melt at these temperatures (≤700 °C).
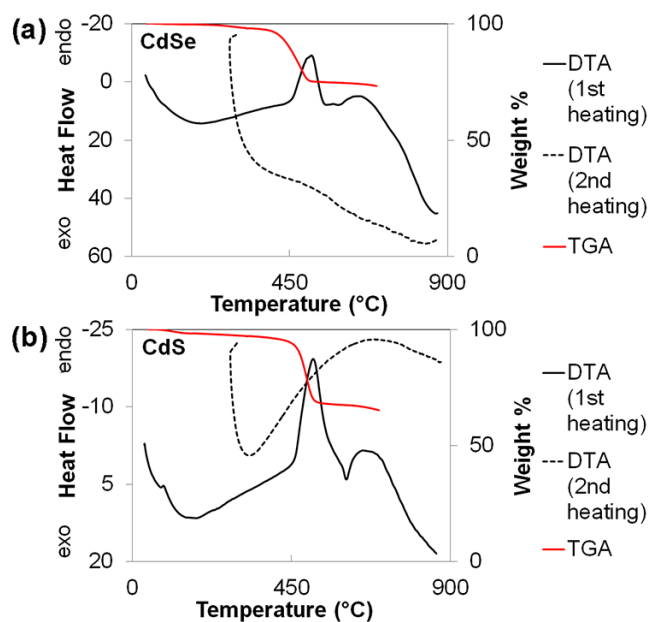

Figure 9. DTA and TGA traces for (a) CdSe and (b) CdS nanorods (first endotherms appear at 499 °C (CdSe) and 511 °C (CdS); second endotherms appear at 581-680 °C (CdSe) and 601-730 °C (CdS)).

Critically, TGA analysis shows that the 1st endotherm (500-510 °C) is coupled to a significant mass loss of 20-30% for both CdSe and CdS nanorods. Given that the same TOP (b.p. = 445 °C), TOPO (b.p. = 411 °C) and ODPA (b.p. = 463 °C) ligands are coating both samples, *we conclude that axial melting is a ligand-dependent and not a material-dependent process*. This suggests that the aspect ratio and degree of anisotropy of the nanorods can only be maintained as long as the particles remain encased by the passivating layer of organic ligands on their surface.
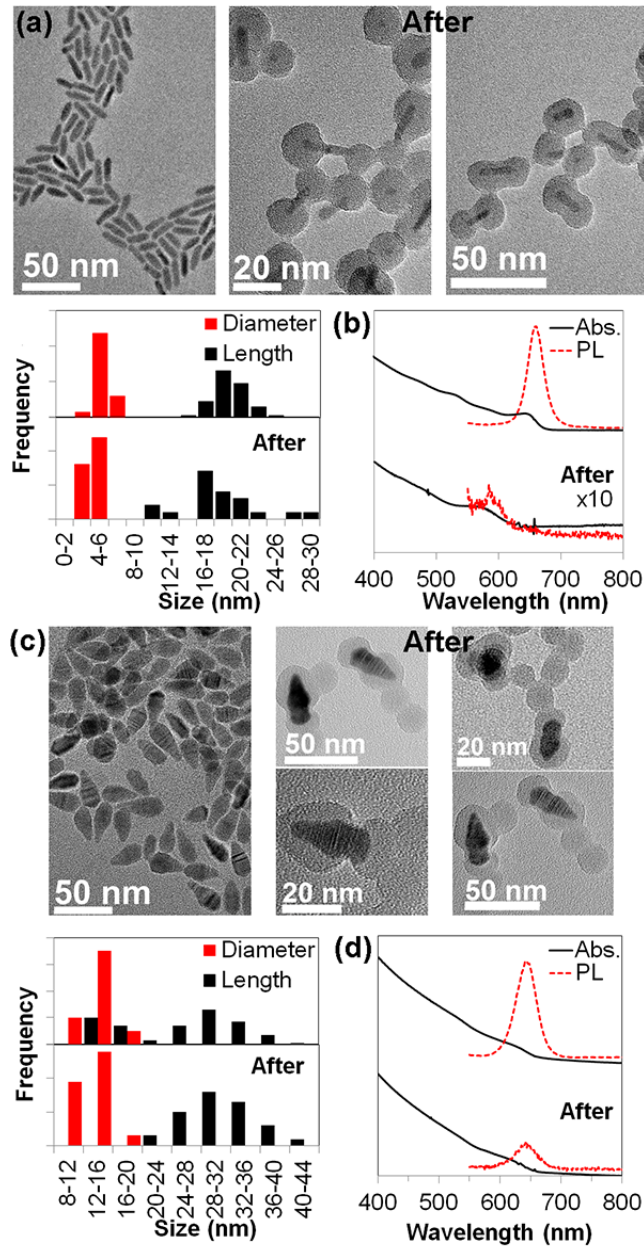
Figure 10. (a, c) TEM images and size histograms, and (b, d) absorption and emission spectra before and after slica coating of (a, b) CdSe nanorods and (c, d) axially anisotropic/compositionally graded $CdS_{0.4}Se_{0.6}$ nanorods.

Probing the effect of curvature: Silica coating. The selective axial melting behavior observed above prompted us to more closely examine the role of surface curvature on the reactivity and (in)stability of II-VI nanorods. We were particularly drawn to the base-catalyzed

hydrolysis and condensation of tetraorthosilicate (TEOS) in the presence of II-VI nanorods.[65-70] As shown in Figure 10, this process results in the heterogeneous nucleation of silica (SiO$_2$) shells on top of CdS$_x$Se$_{1-x}$ nanorods.[71] When CdSe is used (x = 0), SiO$_2$ nucleates starting from the two tips of the nanorods at similar times (concomitantly) (Figure 10a). However, when axially-anisotropic, drumstick-like CdS$_{0.4}$Se$_{0.6}$ nanorods are used, SiO$_2$ first nucleates starting from the thinner, CdS end of the nanorods, followed at a later coating stage by slower nucleation from the thicker, CdSe-rich end of the nanorods (Figure 10c and Scheme 3b).
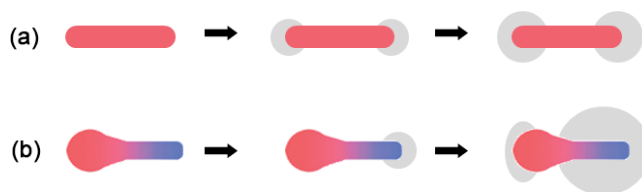
Scheme 3. Time evolution of silica coating in (a) CdSe nanorods (b) and axially anisotropic/compositionally graded CdS$_{0.4}$Se$_{0.6}$ nanorods. (Red = CdSe, Blue = CdS, Gray = SiO$_2$)

Conclusion

In this paper, we investigated the general (but relatively unknown) chemical reactivity of II-VI semiconductor nanorods, with an emphasis on CdSe nanorods. Acids (HCl and HNO$_3$) react rapidly with CdSe nanorods; after 12 h, the CdSe absorption and band edge PL disappear and Se and SeO$_2$ (HNO$_3$) form. CdSe nanorods are relatively stable in basic conditions (NaOH and Me$_4$NOH), as well as in the presence of strong oxidants (KMnO$_4$ and H$_2$O$_2$). Neither bases nor oxidants caused significant changes in absorption spectra, although one oxidant (H$_2$O$_2$) caused a decrease in emission, likely due to the introduction of small amounts of CdO and SeO$_2$ on the nanorod surface. However, bases slightly etch the nanorods along their axis, as evidenced by a decrease in intensity and widening of the 002 XRD peak relative to the 100 and 110 XRD peaks. CdSe nanorods are relatively stable for long periods of time under air at temperatures up

to 350 °C. However, roasting (heating in air) CdSe to 600 °C produces polycrystalline rock salt CdO. Neither CdO nor CdSe nanorods are reduced to Cd in the presence of H_2 at elevated temperatures. Using another reductant, n-BuLi, CdSe gets reduced to Cd metal at 300 °C. Lower reaction temperatures than 300 °C result in incomplete reduction or no reduction at all.

Along with their chemical reactivity, we also explored the thermal stability and effect of curvature on the stability of II-VI semiconductor nanorods (CdSe and CdS). Variable temperature (VT) XRD studies showed that II-VI nanorods respond to heating in three stages: (i) annealing, (ii) axial melting and (iii) coalescence. Furthermore, thermal analysis experiments (DTA and TGA) of CdSe and CdS nanorods showed that axial melting is not reliant on the type of inorganic crystalline material but on the ligand(s) coating its surface. Ligands coating the nanorod surface help maintain their anisotropy and specific aspect ratio. In view of this axial melting behavior, we looked at the effect of curvature on the activity of II-VI nanorods: For example, heterogeneous nucleation of SiO_2 on regularly-shaped CdSe nanorods starts at both tips at the same time, while heterogeneous nucleation of SiO_2 starts from the thinner CdS-rich tip of axially anisotropic $CdS_{0.4}Se_{0.6}$ nanorods (drumsticks). A better and more systematic understanding of the chemical reactivity and general stability of II-VI semiconductor nanostructures may greatly help in furthering their application to photocatalysis, photovoltaics, optics and light emitting devices.

Acknowledgement

References

[1] Amirav, L.; Alivisatos, A. P. *J. Phys. Chem. Lett.* **2010**, *1*, 1051–1054.

[2] Frame, F. A.; Carroll, E. C.; Larsen, D. S.; Sarahan, M.; Browning, D. N.; Osterloh, F. E. *Chem. Commun.* **2008**, 2206–2208.

[3] Qu, Y.; Duan, X. *Chem. Soc. Rev.* **2013**, *42*, 2568–2580.

[4] Spanhel, L.; Weller, H.; Henglein, A. *J. Am. Chem. Soc.* **1987**, *109*, 6632–6635.

[5] Henglein, A. *Top. Curr. Chem.* **1988**, *143*, 113–180.

[6] Henglein, A. *J. Phys. Chem.* **1982**, *86*, 2291–2293.

[7] Spanhel, L.; Haase, M.; Weller, H.; Henglein, A. *J. Am. Chem. Soc.* **1987**, *109*, 5649–5655.

[8] Williams, R. *J. Chem. Phys.* **1960**, *32*, 1505–1514.

[9] Gerischer, H. *J. Electrochem. Soc.* **1966**, *113*, 1174–1182.

[10] Gerischer, H.; Seraphin, B. O. In *Solar Energy Conversion*; Vol. *31*; Springer: Heidelberg, Germany, 1979; p. 115.

[11] Zhou, H.; Qu, Y.; Zeid, T.; Duan, X. *Energy Environ. Sci.* **2012**, *5*, 6732–6743.

[12] Pleskov, Y. V.; Gurevich, Y. Y. In *Semiconductor Photoelectrochemistry*; Bartlett, P. N., Ed.; Plenum: New York, 1986.

[13] Kudo, A.; Miseki, Y. *Chem. Soc. Rev.* **2009**, *38*, 253–278.

[14] Lim, S. J.; Kim, W.; Shin, S. K. *J. Am. Chem. Soc.* **2012**, *134*, 7576–7579.

[15] Carbone, L.; Cozzoli, P. D. *Nano Today* **2010**, *5*, 449–493.

[16] Wen, X.; Sitt, A.; Yu, P.; Ko, H. C.; Toh, Y. R.; Tang, J. *J. Nanopart. Res.* **2012**, *14*, 1278-1–13.

[17] Wilker, M. B.; Schnitzenbaumer, K. J.; Dukovic, G. *Isr. J. Chem.* **2012**, *52*, 1002–1015.

[18] Ruberu, T. P. A.; Nelson, N. C.; Slowing, I. I.; Vela, J. *J. Phys. Chem. Lett.* **2012**, *3*, 2798–2802.

[19] Vela, J. *J. Phys. Chem. Lett.* **2013**, *4*, 653–668.

[20] Ha, J. W.; Ruberu, T. P. A.; Han, R.; Dong, B.; Vela, J.; Fang, N. *J. Am. Chem. Soc.* **2014**, *136*, 1398–1408.

[21] Shim, M.; Guyot-Sionnest, P. *Nature* **2000**, *407*, 981−983.

[22] Wang, C.; Shim, M.; Guyot-Sionnest, P. *Science* **2001**, *291*, 2390−2392.

[23] Yu, T.-H.; Cheng, W.-Y.; Chao, K-J.; Lu, S.-Y. *Nanoscale* **2013**, *5*, 7356–7360.

[24] Xiong, P.; Zhu, J.; Wang, X. *Ing. Eng. Chem. Res.* **2013**, *52*, 17126−17133.

[25] Lim, S. J.; Kim, W.; Jung, S.; Seo, J.; Shin, S.K. *Chem. Mater.* **2011**, *23*, 5029–5036.

[26] Guo, W.; Li, J. J.; Wang, A.; Peng, X. *J. Am. Chem. Soc*. **2003**, *125*, 3901–3909.

[27] Ogata, K.; Dobashi, H.; Koike, K.; Sasa, S.; Inoue, M.; Yano, M. *Phys. Status Solidi C* **2010**, *7*, 1562–1564.

[28] Gao, S.; Xie, Y.; Zhu, L.; Tian, X. *Inorg. Chem*. **2003**, *42*, 5442–5447.

[29] Wang, Y.; Hou, L.; Qin, X.; Ma, S.; Zhang, B.; Gou, H.; Gao, F. *J. Phys. Chem. C* **2007,** *111,* 17506–17511.

[30] Niu, Y. F.; Guin, J. P.; Rouxel, T.; Abdelouas, A.; Troles, J.; Smektala, F. *J. Am. Ceram. Soc.* **2009**, *92*, 1779–1787.

[31] Jana, N.; Gearheart, L.; Obare, S.; Murphy, C. J. *Langmuir* **2002**, *18*, 922–927.

[32] Sau, T. K.; Rogach, A. L.; Jäckel, F.; Klar, T. A.; Feldmann, J. *Adv. Mater.* **2010**, *22*, 1805–1825.

[33] Tsung, C.; Kou, X.; Shi, Q.; Zhang, J.; Yeung, M. H.; Wang, J.; Stucky, G. D. *J. Am. Chem. Soc.* **2006**, *126*, 5352–5353.

[34] Murphy, C. J.; Sau, T. K.; Gole, A. M.; Orendorff, C. J.; Gao, J.; Gou, L.; Hunyadi, S. E.; Li, T. *J. Phys. Chem. B* **2005**, *109*, 13857–13870.

[35] Su, X.; Zhang, Z.; Zhu, M. *Appl. Phys. Lett.* **2006**, *88*, 061913-1–3.

[36] Wu, Y. Y.; Yang, P. D. *Adv. Mater.* **2001**, *13*, 520–523.

[37] Karabacak, T.; Deluca, J. S.; Wang, P. I.; Ten Eyck, G. A.; Ye, D.; Wang, G. C.; Lu, T. M. *J. Appl. Phys.* **2006**, *99*, 064304-1–6.

[38] Cross, M. W.; Varhue, W. J. *Nanotechnology* **2008**, *19*, 435705-1–5.

[39] Yalcin, A. O.; van Huis, M. A.; Tichelaar, F. D.; Zandbergen, H. W. *In-situ high resolution TEM study of CdSe nanorods sub-limation*. 15th European Microscopy Congress, Manchester Central, United Kingdom, September 16–21, 2012.

[40] Kotkata, M. F.; Masoud, A. E.; Mohamed, M. B. Mahmoud, E.A. *Physica E* **2009**, *41*, 1457–1465.

[41] Kotkata, M. F.; Masoud, A. E.; Mohamed, M. B. Mahmoud, E. A. *Physica E* **2009**, *41*, 640–645.

[42] Goldstein, A. N.; Echer, C. M.; Alivisatos, A. P. *Science* **1992**, *256*, 1425–1427.

[43] Paul, G. S.; Gogoi, P.; Agarwal, P. *J. Non-Cryst. Solids* **2008**, *354*, 2195–2199.

[44] *Handbook of Thermal Analysis*; Hatakeyama, T., Liu, Z., Eds.; John Wiley & Sons; Chichester, U.K., 1998; Chapter 3, p 43.

[45] Goris, B.; van Huis, M. A.; Bals, S.; Zandbergen, H. W.; Manna, L.; van Tendeloo, G. *Small* **2012**, *8*, 937–942.

[46] Khan, A. H.; Ji, Q.; Ariga, K.; Thupakula, U.; Acharya, S. *J. Mater. Chem.* **2011**, *21*, 5671–5676.

[47] Link, S.; El-Sayed, M. A. Optical Spectroscopy of Surface Plasmons in Metal Nanoparticles. In *Semiconductor and Metal Nanocrystals: Synthesis and Electronic and Optical Properties*; Klimov, V.I., Ed.; Marcel Dekker, Inc.; New York, 2004, 421–452.

[48] Link, S.; Wang, Z. L.; El-Sayed, M. A. *J. Phys. Chem. B* **2000**, *104*, 7867–7870.

[49] Van Huis, M. A.; Figuerola, A.; Fang, C.; Béché, A.; Zandbergen, H. W.; Manna, L. *Nano Lett.* **2011**, *11*, 4555–4561.

[50] Deng, Z. X.; Li, L.; Li, Y. *Inorg. Chem.* **2003**, *42*, 2331–2341.

[51] Fan, Z.; Yalcin, A. O.; Tichelaar, F. D.; Zandbergen, H. W.; Talgorn, E.; Houtepen, A. J.; Vlugt, T. J. H.; van Huis, M. A. *J. Am. Chem. Soc.* **2013**, *135*, 5869–5876.

[52] Pan, L. S.; Lee, H. P.; Lu, C. *Eur. Phys. J. D* **2008**, *50*, 27–33.

[53] Rivest, J.; Jain, P. K. *Chem. Soc. Rev.* **2013**, *42*, 89–96.

[54] Subila, K. B.; Kumar, G. K.; Shivaprasad, S. M.; Thomas, K. G. *J. Phys. Chem. Lett.* **2013**, *4*, 2774–2779.

[55] Sharma, H.; Sharma, S. N.; Singh, G.; Shivaprasad, S. M. *J. Nanosci. Nanotechnol.* **2007**, *7*, 1953–1959.

[56] Park, Y.; Felipe, M. J.; Advincula, R. C. *App. Mater. Interfaces* **2011**, *3*, 4363–4369.

[57] Farva, U.; Park, C. *Sol. Energy Mater. Sol. Cells* **2010**, *94*, 303–309.

[58] Lee, W.; Kim, H.; Jung, D.-R.; Kim, J.; Nahm, C.; Lee, J.; Kang, S.; Lee, B.; Park, B. *Nanoscale Res. Lett.* **2012**, *7*, 672-1–5.

[59] Costas-Mora, I.; Romero, V.; Lavilla, I.; Bendicho, C. *Anal. Chim. Acta* **2013**, *788*, 114–121.

[60] Robinson, R. D.; Sadtler, B.; Demchenko, D. O.; Erdonmez, C. K.; Wang, L.-W.; Alivisatos, A. P. *Science* **2007**, *317*, 355–358.

[61] Ruberu, T. P. A; Vela, J. *ACS Nano* **2011**, *5*, 5775–5784.

[62] Ruberu, T. P. A.; Albright, H. R.; Callis, B.; Ward, B.; Cisneros, J.; Fan, H.-J.; Vela, J. *ACS Nano* **2012**, *6*, 5348–5359.

[63] Alemseghed, M. G.; Ruberu, T. P. A.; Vela, J. *Chem. Mater.* **2011**, *23*, 3571–3579.

[64] Kuno, M. *Phys. Chem. Chem. Phys.* **2008**, *10*, 620–639.

[65] Khanal, B. P.; Pandey, A.; Li, L.; Lin, Q.; Bae, W. K.; Luo, H.; Klimov, V. I.; Pietryga, J. M. *ACS Nano* **2012**, *6*, 3832–3840.

[66] Lian, J.; Xu, Y.; Lin, M.; Chan, Y. *J. Am. Chem. Soc*. **2012**, *134*, 8754−8757.

[67] Kumar, R.; Ding, H.; Hu, R.; Yong, K.-T.; Roy, I.; Bergey, E. J.; Prasad, P. N. *Chem. Mater*. **2010**, *22*, 2261−2267.

[68] Gupta, N.; Pal, B. *J. Nanosci. Nanotechnol.* **2013**, *13*, 5069–5079.

[69] Liu, N.; Prall, B. S.; Klimov, V. I. *J. Am. Chem. Soc.* **2006**, *128*, 15362–15363.

[70] Obare, S. O.; Jana, N. R.; Murphy, C. J. *Nano Lett.* **2001**, *1*, 601–603.

[71] Pietra, F.; van Dijk - Moes, R. J. A.; Ke, X.; Bals, S.; Van Tendeloo, G.; de Mello Donega, C.; Vanmaekelbergh, D. *Chem. Mater*. **2013**, *25*, 3427−3434.

Supporting Information

$$CdSe + 4M\ HNO_3 \xrightarrow[\text{3 day}]{\text{RT}} Se^0 + SeO_2 \qquad (\textit{unbalanced}) \quad \textbf{(S1)}$$
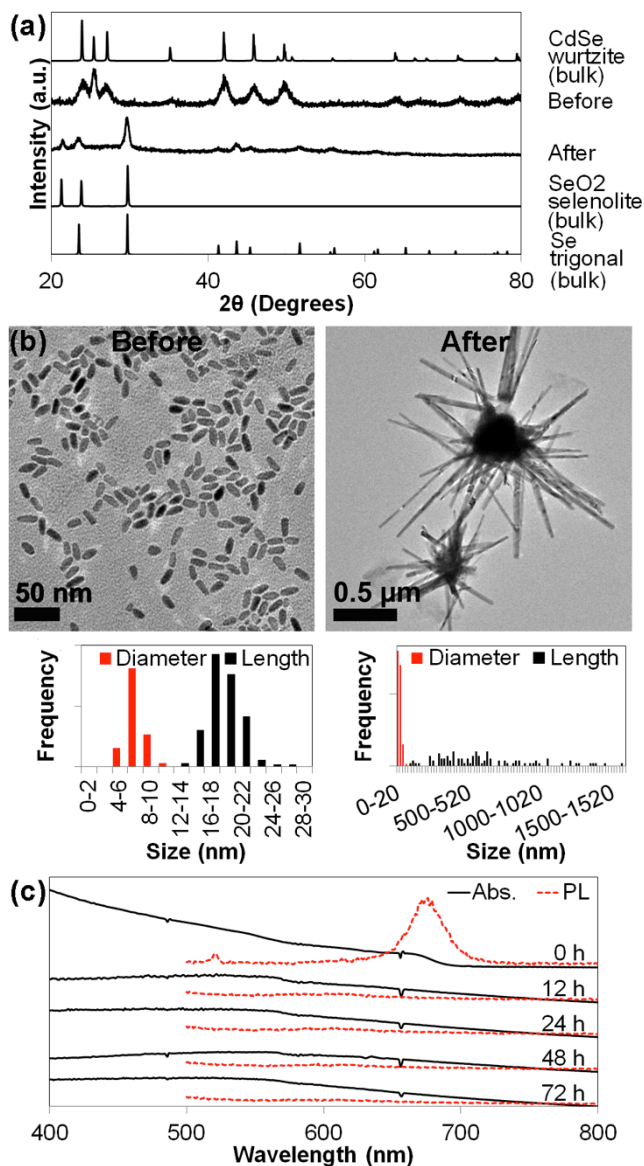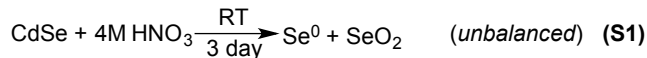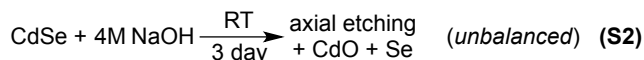

Figure S1. Reactivity of CdSe nanorods against acids: (a) Powder XRD patterns, (b) representative TEM images and size histograms, and (c) time evolution of absorption and emission spectra upon treatment with aqueous 4M HNO$_3$ at R.T. for 3 days.
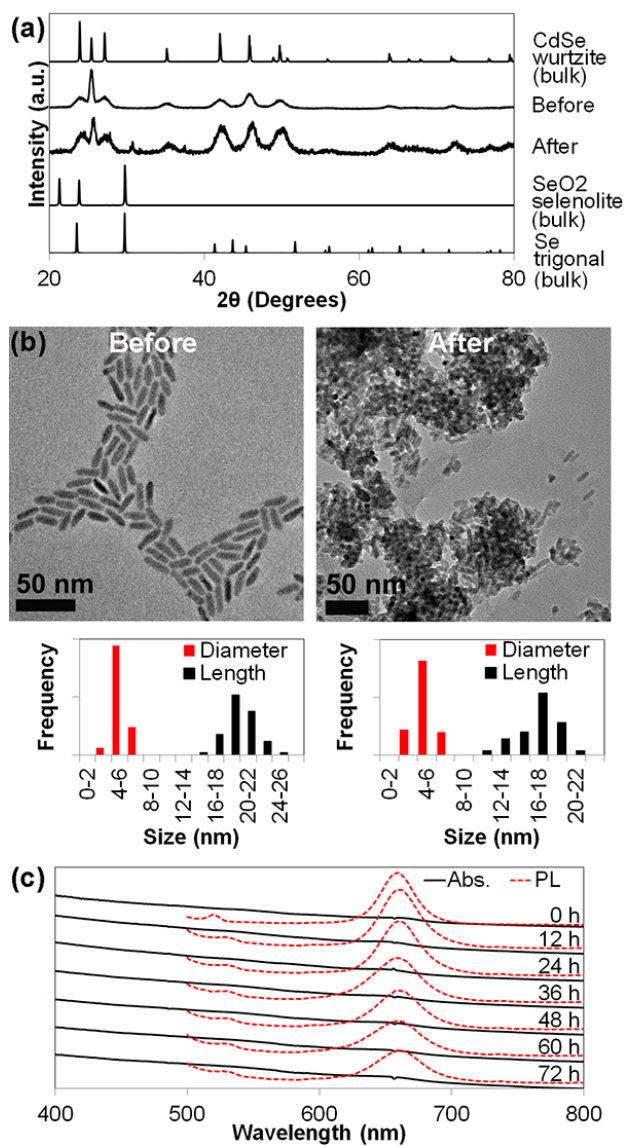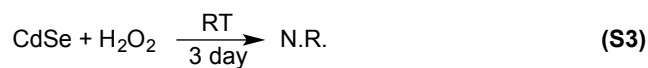
$$CdSe + 4M\ NaOH \xrightarrow[\text{3 day}]{\text{RT}} \text{axial etching} + CdO + Se \qquad (\textit{unbalanced}) \quad \textbf{(S2)}$$

Figure S2. Reactivity of CdSe nanorods against bases: (a) Powder XRD patterns, (b) representative TEM images and size histograms, and (c) time evolution of absorption and emission spectra upon treatment with aqueous 4M NaOH at R.T. for 3 days.
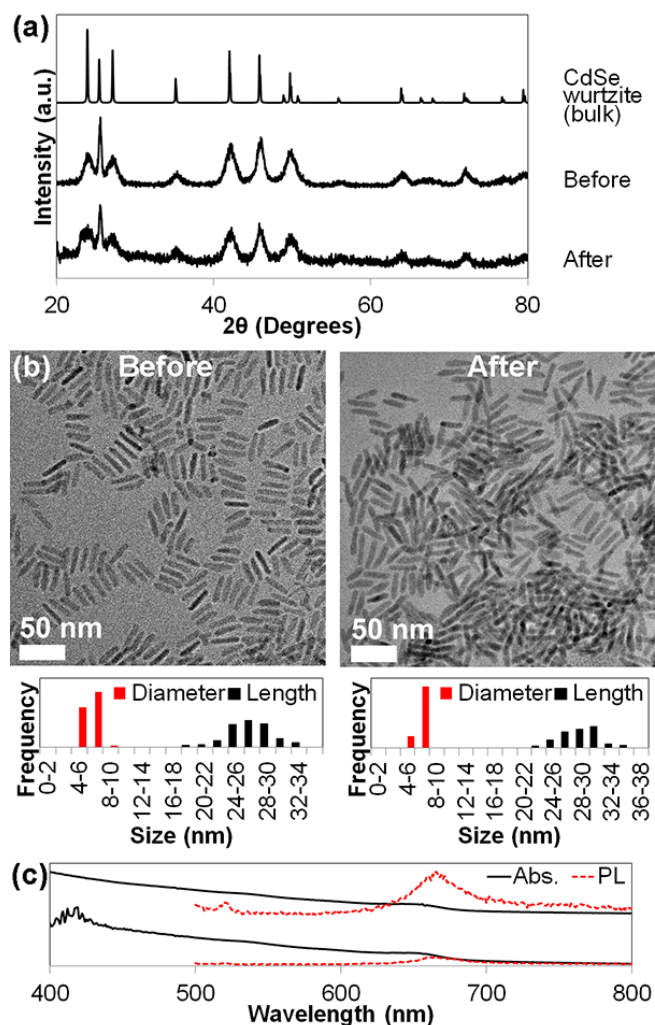
$$CdSe + H_2O_2 \xrightarrow[\text{3 day}]{\text{RT}} \text{N.R.} \qquad \text{(S3)}$$

Figure S3. Reactivity of CdSe nanorods against oxidants: (a) Powder XRD patterns, (b) representative TEM images and size histograms, and (c) time evolution of absorption and emission spectra of CdSe nanorods upon treatment with aqueous 30% w/w H_2O_2 at R.T. for 3 days.

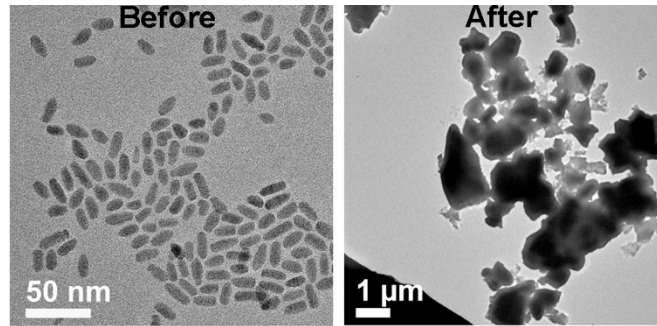$$CdSe \xrightarrow[\Delta, t]{O_2 \text{ (air)}} CdO \qquad (unbalanced) \quad \textbf{(S4)}$$

Figure S4. TEM images and morphology of CdSe nanorods before and after roasting (heating in air) at 600 °C for 4 h.
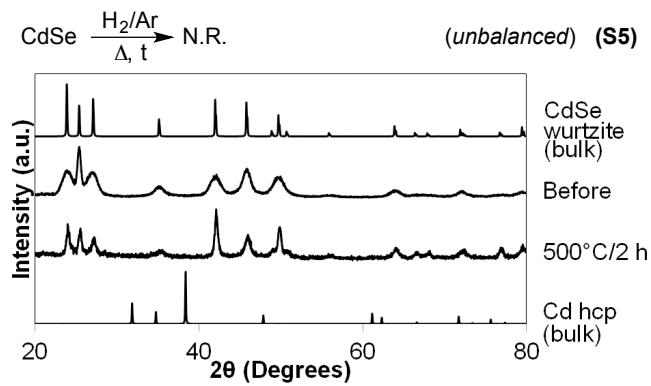

Figure S5. Reactivity of CdSe nanorods against reductants: (a) Powder XRD patterns of CdSe nanorods upon heating with H_2.
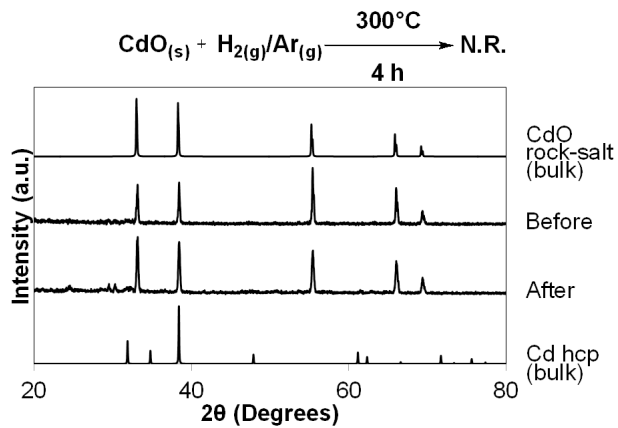

Figure S6. XRD patterns of CdO (made by roasting) before and after treating with H_2 300 °C.
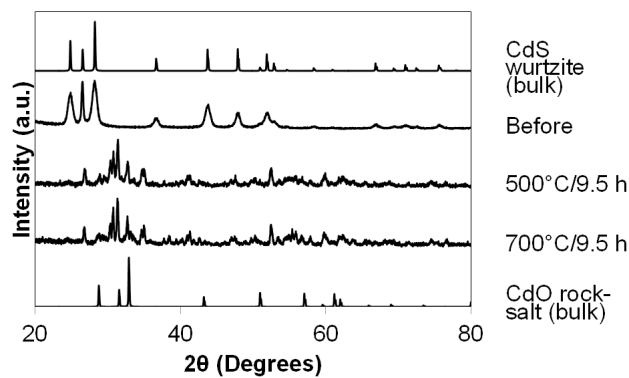
Figure S7. Reactivity of CdS nanorods against oxidants: Powder XRD patterns showing the effect of O_2 (and moisture) from air upon heating at different temperatures.
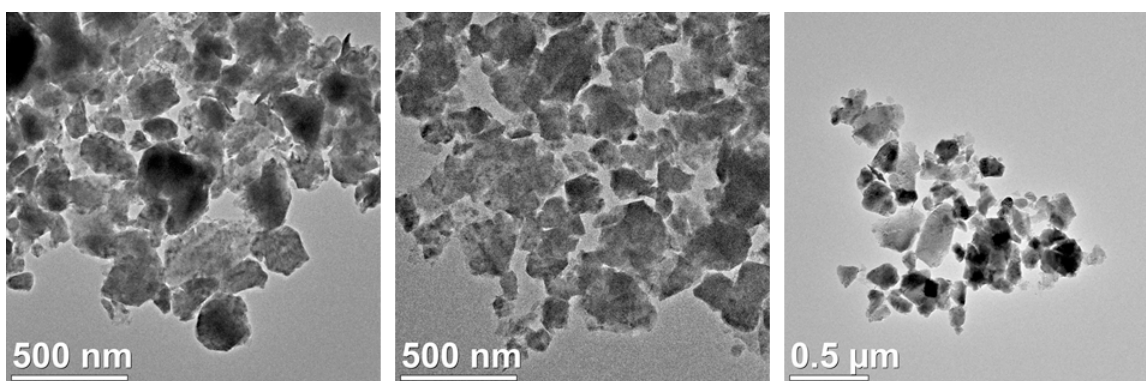

Figure S8. Representative TEM images obtained after heating CdSe nanorods to 700 °C for a couple of hours (after VT experiments).

CHAPTER 3

PREPARATION AND INSTABILITY OF NANOSIZED CUPROUS NITRIDE

Malinda D. Reichert, Miles A. White, Michelle J. Thompson, Gordon J. Miller, Javier Vela

Abstract

Low-dimensional cuprous nitride (Cu_3N) was synthesized by nitridation (ammonolysis) of cuprous oxide (Cu_2O) nanocrystals using either ammonia (NH_3) or urea (H_2NCONH_2) as the nitrogen source. The resulting nanocrystalline Cu_3N spontaneously decomposes to nanocrystalline CuO in the presence of both water and oxygen from air at room temperature. Ammonia was produced in 60% chemical yield during Cu_3N decomposition, as measured using the colorimetric indophenol method. Because Cu_3N decomposition requires H_2O and produces substoichiometric amounts of NH_3, we conclude that this reaction proceeds through a complex stoichiometry that involves the concomitant release of both N_2 and NH_3. This is a thermodynamically unfavorable outcome, strongly indicating that H_2O (and thus NH_3 production) facilitate the kinetics of the reaction by lowering the energy barrier for Cu_3N decomposition. The three different Cu_2O, Cu_3N and CuO nanocrystalline phases were characterized by a combination of optical absorption, powder X-ray diffraction, transmission electron microscopy, and electronic density of states (DOS) obtained from electronic structure calculations on the bulk solids. The relative ease of inter-conversion between these interesting and inexpensive materials bears possible implications for catalytic and opto-electronic applications.

Introduction

Copper(I) nitride (Cu_3N) is a metastable semiconductor that has a low reflectivity and high electrical resistivity.[1] It has been reported to have a narrow experimental band gap of 1.2-1.9 eV[2] and features a cubic anti-ReO_3 structure.[3] Because of these properties, Cu_3N nanocrystals (NCs) are promising materials for optical storage devices, random access memory chips, conductive inks, high-speed integrated circuits, microscopic metal links, photocatalysis, and electrocatalytic hydrogen reduction devices.[1-3]

Cu_3N NCs can be synthesized by several methods. Cu_3N nanocubes were synthesized by the one-pot decomposition of copper(II) nitrate in octadecene, octadecylamine, and oleylamine.[1,2,4,5] Copper nitride nanocrystals were also produced by decomposing $Cu(OAc)_2$ with ammonia,[3,6-9] a metastable $CuCl_2$-sodium azide precursor,[10] or $\{[Cu_5(CN)_6(NH_3)_6(N_3)_2]\}_n$.[11] Cu_3N nanopowders were produced by ammonolysis of CuF_2.[12] Cu_4N and Cu_3N_2 nanostructures have been prepared as thin films.[13-16]

A versatile route for making nitrides and oxynitrides is the nitridation (ammonolysis) of metal oxides. CuO has been used as a precursor to Cu_3N. Silica-supported CuO nanoparticles were converted to Cu_3N by nitridation with ammonia.[17] Nitridation of sol-gel CuO with ammonia produced silica-supported Cu_3N nanocrystals.[18] Ammonia is believed to reduce CuO to a zerovalent (metallic) copper intermediate during nitride formation.[19]

Cupric (Cu^{2+}) and cuprous (Cu^+) oxide nanocrystals are well described in the literature. The synthesis, characterization, and optoelectronic properties of CuO nanostructures have been reviewed.[20,21] Like CuO nanocrystals, nitridation of Cu_2O nanocrystals could also lead to Cu_3N. Controlled syntheses (monodispersity, size,

morphology) of Cu_2O nanocrystals by electrodeposition, wet chemical, and solvothermal methods exist, along with reports on their surface, catalytic, and electrical properties.[20,22,23]

An interesting feature of Cu_3N is its documented decomposition upon heating or electron bombardment. For example, Cu_3N thin films convert to CuO nanowire arrays by annealing in air.[24] Cu_3N deposited by magnetic sputtering converts to Cu and N_2 under electron bombardment or by annealing in a vacuum.[25,26] The optical properties of Cu_3N thin films made by ion-assisted deposition remained unchanged upon conducting an aging test at 60 °C and 95% humidity for 15 months, but degrade to copper metal when heated to 300 °C.[27] Cu_3N nanocubes were reported to degrade thermally, forming CuO at temperatures ranging between 200-330 °C under an argon atmosphere.[3]

In this work, we synthesize Cu_3N nanocrystals by nitridation of Cu_2O nanocrystals with either ammonia or urea. We characterize the structure, optical properties, and morphology of both oxide and nitride phases using structural, optical and computational methods. We also describe the spontaneous room-temperature decomposition of Cu_3N nanocrystals upon exposure to moisture and air, and used simple thermodynamics calculations to explain that the observed concomitant release of NH_3 and N_2 is due to kinetic factors.

Experimental

Materials. Copper(II) chloride dihydrate ($CuCl_2 \cdot 2H_2O$, 99.0%) and sodium nitroprusside dihydrate ($Na_2[Fe(CN)_5NO] \cdot 2H_2O$, 99.0%) were purchased from Sigma-Aldrich; ammonium carbonate (($NH_4)_2CO_3$, tech.), ascorbic acid ($C_6H_8O_6$, tech.), and sodium hydroxide (NaOH, tech.) from Fisher; urea (H_2NCONH_2, tech.) and phenol (C_6H_5OH, tech.)

from Alfa Aesar; ammonia gas (NH_3, 99.99%) from Airgas; and sodium hypochlorite (NaOCl, 8.25%) from Clorox. All chemicals were used as received.

Synthesis. *Cu_2O nanocrystals.* Cu_2O nanocrystals were made by a modified literature procedure:[28] Briefly, 100 mL of a 0.4 M NaOH solution was added to 100 mL of a 0.2 M $CuCl_2$ solution. After the solution was stirred for 5 min, 100 mL of a 0.2 M $C_6H_8O_6$ was added. The mixture was stirred for 25 min and centrifuged. The precipitate was collected, washed three times with distilled water and once with ethanol, and dried at room temperature (R.T., *ca.* 21-24 °C) for 12 h. *Cu_3N nanocrystals from ammonia.* Cu_2O nanocrystals (0.15 g) were placed in an alumina combustion boat and put in a fused silica tube inside of a tube furnace (Lindberg 55035). The tube was purged with NH_3 (60 mL/min) for 30 min and then heated to 250 °C for 21 h. *Cu_3N nanocrystals from urea.* Cu_2O nanocrystals (0.15 g) were weighed along with H_2NCONH_2 (0.126 g) into a Teflon liner inside a 23 mL steel autoclave. The autoclave was placed in a Thomas Scientific (5300A25) muffle furnace and heated to 190 °C (10 °C/min ramp rate, 6 h dwell time). *CuO from Cu_3N decomposition.* Cu_3N (~100 mg, synthesized using either NH_3 or H_2NCONH_2) was exposed to de-ionized water (10 mL) for 15 days. The product was isolated by centrifugation (4500 rpm, 10 min). To determine the amount of ammonia released during the Cu_3N decomposition reaction, we used the *indophenol method.*[29,30] *Solution A:* C_6H_5OH (5 g, 53 mmol) and $Na_2[Fe(CN)_5NO]\cdot2H_2O$ (0.025 g, 0.084 mmol) were dissolved in deionized water (500 mL) using a volumetric flask. *Solution B:* NaOH (2.5 g, 62.5 mmol) was dissolved in deionized water, NaOCl (8.25%, 4.2 mL) added, and solution diluted with deionized water to 500 mL in a volumetric flask. The two solutions were stored in amber bottles at *ca.* 8-10 °C using a refrigerator and used within 2 weeks. Seven different calibration solutions were made using solution A (5 mL) and a 0.5

mM solution of $(NH_4)_2CO_3$ in deionized water (0 to 350 µL in 50 µL increments). Solution B (5 mL) was added and the mixture stirred at 37 °C for 20 min. Absorbance values at $\lambda = 623$ nm were used to construct the calibration curve. After centrifugation to isolate the CuO during Cu_3N decomposition, the same indophenol method was to analyze the supernatant solutions (100 µL) for NH_3 content. Values reported are three-run averages.

Structural Characterization. *X-Ray Diffraction.* Powder X-ray diffraction (XRD) data were measured using Cu Kα radiation on a Rigaku Ultima U4 difractometer. Sample percent composition was determined using PowderCell 2.4 (PCW) refined against standard XRD patterns for Cu_2O, Cu_3N, and CuO. Single-crystalline domain sizes were calculated using the Scherrer equation and the typical uncertainty estimated to be ± 0.2 nm. *Transmission Electron Microscopy.* Transmission electron microscopy (TEM) was conducted on carbon-coated copper grids using a FEI Tecnai G2 F20 field emission scanning transmission electron microscope (STEM) at 200 kV (point-to-point resolution <0.25 nm, line-to-line resolution <0.10 nm). Particle dimensions were measured manually and/or by using ImageJ. Size measurements and particle statistics were obtained for at least >100 particles. Average sizes ± standard deviations are reported.

Optical Characterization. Absorption spectra were measured using a photodiode array Agilent 8453 UV-Vis spectrophotometer. Solvent absorption was subtracted from all spectra. Diffuse reflectance measurements were made using a StellarNet Inc. Black-Comet-SR spectrometer (200-1080 nm).

Density of States (DOS) Calculations. Electronic structure calculations of CuO, Cu_2O, and Cu_3N were performed using the Vienna *Ab initio* Simulation Package (VASP).[31,32] All VASP calculations were performed using projected augmented-wave (PAW)

pseudopotentials with a cutoff energy of 500 eV and a convergence energy of 1×10^{-6} eV.[33] A conjugated algorithm was applied for the structural optimization with a $15 \times 15 \times 15$ Monkhorst-pack k-points grid.[34] During structure optimization, atomic coordinates and cell volumes were allowed to optimize. Total energies were calculated using the tetrahedron method with Blöchl[35] corrections applied. All VASP calculations treated exchange and correlation by the Perdew-Burke-Enzerhoff (PBE) method.[36] Because of the highly correlated nature of these compounds, on-site Coulomb interactions were used (LDA + U). The *U* value applied was 5.0 eV for the Cu d states due to this value being successful for previous studies on strongly correlated Cu compounds.[37,38]

Results and Discussion

Synthesis of Cu₂O nanocrystals. On the basis of previous reports of successful nitridation of CuO, we attempted to perform a similar reaction using nanocrystalline Cu_2O as the starting material. We first synthesized Cu_2O nanocrystals by reacting copper(II) chloride and sodium hydroxide using a modified literature procedure.[28] This reaction proceeds through a blue copper-hydroxide intermediate, which upon treatment with ascorbic acid produces an orange solution of Cu_2O. X-ray diffraction confirmed the formation of cubic copper(I) oxide (Cu_2O) nanocrystals (Figures 1 and 2a). The unit cell of Cu_2O consists of a body-centered cubic (bcc) arrangement of oxide ions (O^{2-}) with two-coordinate cuprous ions (Cu^+) linking every second corner with the central oxide (Figure 2a). The size of the Cu_2O nanocrystals, as estimated from XRD peak widths using the Scherrer equation, is approximately 25 nm. Figure 3 shows the general appearance and optical absorption of the Cu_2O nanocrystals. Absorption starts at 600 nm for both the diffuse reflectance of a solid film and the solution phase absorption spectrum of the Cu_2O nanocrystals, which roughly agree

with a reported experimental Cu_2O band gap of 2.2 eV (see calculated *vs.* experimental band

gap discussion below).[28] TEM shows that the Cu_2O nanocrystals have a cubic morphology,

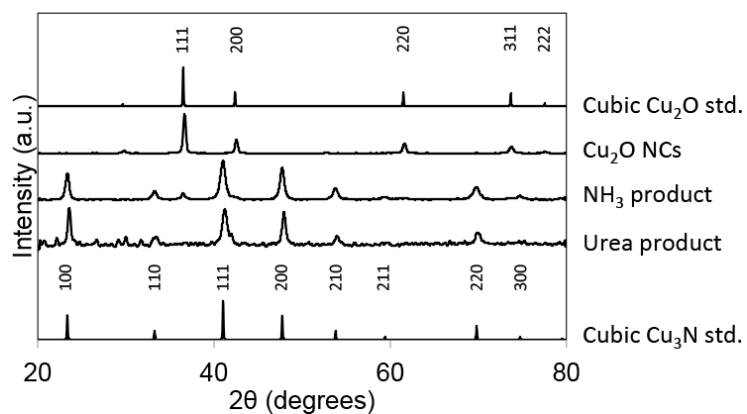with an average size of 43 ± 10 nm (Figure 4). Table 1 summarizes these observations.

Figure 1. Experimental powder XRD patterns before and after treating Cu_2O nanocrystals with ammonia (NH_3) or urea (H_2NCONH_2). Reported powder XRD patterns for bulk cubic Cu_2O and cubic (anti-ReO$_3$) Cu_3N are shown for comparison.
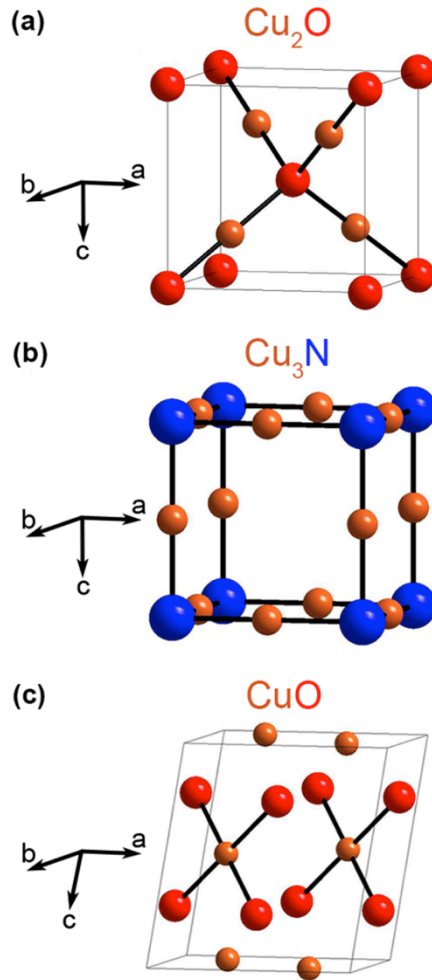
Figure 2. Crystalline unit cells for cubic (a = 4.27 Å) (cuprite) Cu_2O (a), cubic (a = 3.81 Å) (anti-ReO_3) Cu_3N (b), and monoclinic (a = 4.68 Å, b = 3.47 Å, c = 5.12 Å, and β = 99.7°) (tenorite) CuO (c).
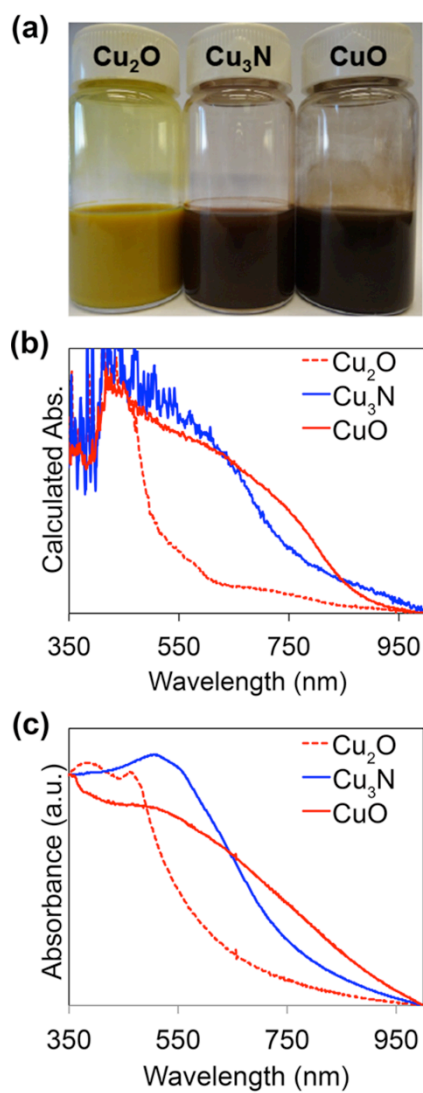
Figure 3. General appearance (suspended in methanol) (a), solid phase diffuse reflectance (b), and solution phase electronic absorption spectra (in methanol) (c) of nanocrystalline Cu_2O, Cu_3N, and CuO.
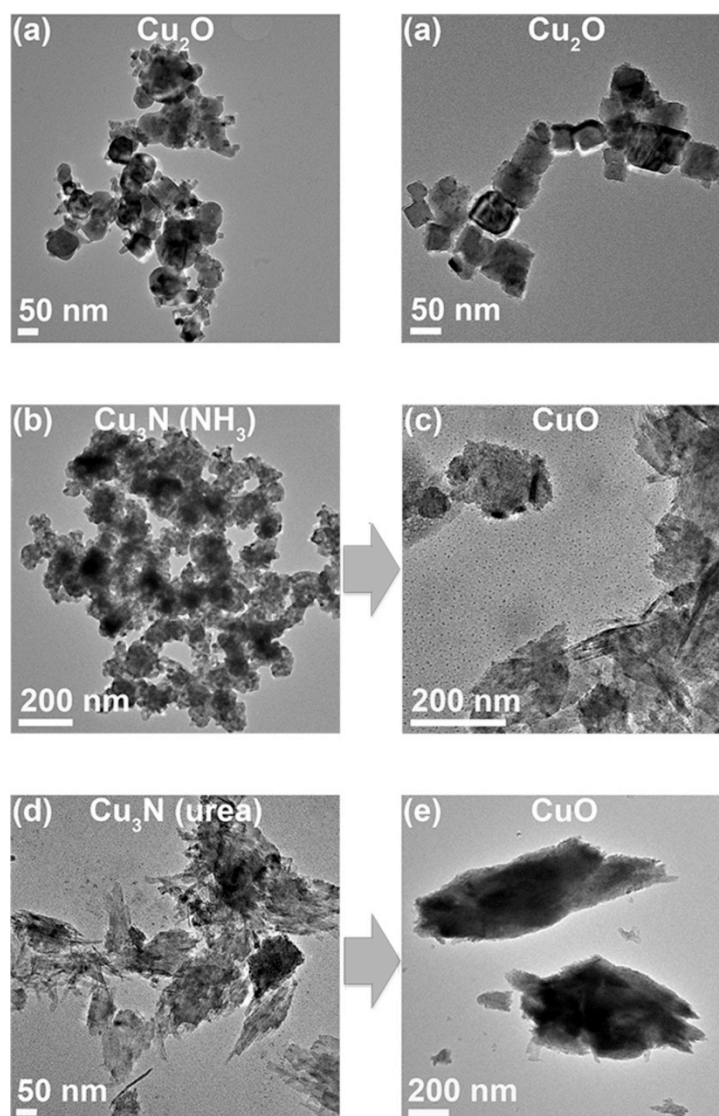
Figure 4. Representative TEM micrographs of nanocrystalline Cu₂O (a), Cu₃N made from NH₃ (b) and its decomposition product (c), and Cu₃N made from urea (d) and its decomposition product (e).

Nitridation of Cu₂O nanocrystals. We used two different reagents to nitride nanocrystals of Cu_2O to produce Cu_3N, namely, ammonia (NH_3) and urea (H_2NCONH_2) (equations 1 and 2, respectively, in Scheme 1). XRD shows that, in both cases, the main product is made of anti-ReO₃ Cu_3N nanocrystals with Scherrer sizes of 15 nm (NH_3) and 22 nm (urea) (Figure 1 and Table 1). The cubic, anti-ReO₃-type unit cell of Cu_3N consists of a primitive cubic arrangement of nitride ions with two-coordinate cuprous ions linking every

two neighboring nitrides (Figure 2b). The product of nitridation with ammonia contains some unreacted Cu_2O (6%), while the product of nitridation with urea contains smaller amounts of Cu_2O (1.6 %) and CuO (0.4 %) (Table 1). Figure 3 shows diffuse reflectance (solid) and optical absorption (solution) spectra of the Cu_3N nanocrystals made using ammonia as the nitridation agent as a representative example. These nanocrystals show an absorption band edge of around 700 nm, which very roughly matches different reports of experimental Cu_3N band gaps between 1.1 eV and 1.9 eV.[39] The absorption spectra of the reddish-brown Cu_3N nanocrystals in both solid form and in solution demonstrate this red shifting (Figure 3b,c). TEM measurements indicate a reagent-dependent change in nanocrystal morphology upon nitridation. Nitridation with ammonia leads to aggregated, spheroidal Cu_3N nanocrystals with a size of 22 ± 7 nm (Figure 4b and Table 1). Nitridation with urea leads to aggregated Cu_3N nanocrystals with a wider range of morphologies, including rods, sheets, and clusters with sizes of 370 ± 160 nm, 310 ± 160 nm, and 220 ± 140 nm, respectively (Figure 4d and Table 1).

#			Dimensions (nm)		XRD phase(s) (% composition)[c]
	Precursors	Conditions	XRD	TEM	
1	$CuCl_{2(aq)}$ + NaOH + $C_6H_8O_6$[a]	R.T.,[b] 20 min	25	43 ± 10	Cubic Cu_2O (100)
2	Cu_2O + $NH_{3(g)}$	250 °C, 24 h	15	22 ± 7	Cubic (anti-ReO_3) Cu_3N (94) + cubic Cu_2O (6)
3	Cu_2O + H_2NCONH_2 (urea)	190 °C, 6 h	22	370 ± 160 (rods) 310 ± 160 (sheets) 220 ± 140 (aggregates)	Cubic (anti-ReO_3) Cu_3N (98) + cubic Cu_2O (1.6) + monoclinic (tenorite) CuO (0.4)
4	Cu_3N (NH_3) + H_2O + O_2 (air)	R.T.,[b] 15 d	16	13 ± 3 (dots) 140 ± 60 (aggregates)	Monoclinic (tenorite) CuO (99.1) + cubic Cu_2O (0.7) +

Table 1. Synthesis and Instability Studies of Cuprous Nitride Nanocrystals.

Table 1. continued				
				cubic (anti-ReO$_3$) Cu$_3$N (0.2)
5	Cu$_3$N (urea) + H$_2$O + O$_2$ (air)	R.T.,[b] 15 d	12	100 ± 70 (aggregates)	CuO monoclinic (100)
[a]Ascorbic acid. [b]21-24 °C. [c]Sample percent composition was determined using PowderCell 2.4 (PCW) refined against standard XRD patterns for Cu$_2$O, Cu$_3$N, and CuO.				

Electronic structure calculations. To gain more insight into the optical properties of the different nanocrystalline copper phases presented here, we performed first-principles electronic structure calculations on bulk solids to obtain electronic DOS curves (Figure 5). Cu$_2$O and Cu$_3$N both display similar electronic structures. In both species, a band gap is present at the Fermi level with a magnitude of 0.95 eV and 0.73 eV for Cu$_3$N and Cu$_2$O, respectively. This value agrees well with previously reported calculations: Cu$_2$O is similar to prior calculations that reported a theoretical value of 0.78;[40] Cu$_3$N calculations claimed band gaps that were generally smaller but ranged in theoretical value from 0.23 to 0.9 eV.[41] Our calculated band gap for Cu$_3$N agrees well with experimental values, while the Cu$_2$O band gap is much smaller than those obtained experimentally. An explanation for this discrepancy is the difference between electronic and optical band gaps in Cu$_2$O. Previous work has found that the direct transition at Γ is forbidden, which leads to no appreciable optical absorption until above 2 eV.[42]
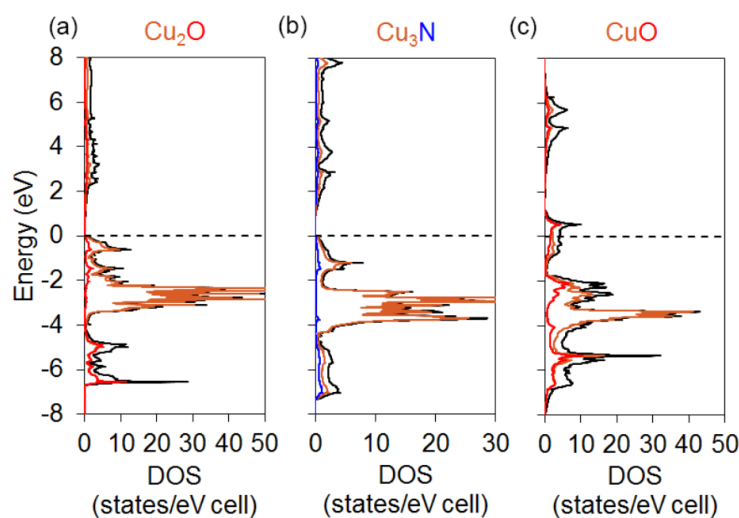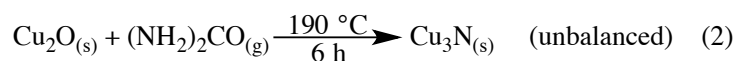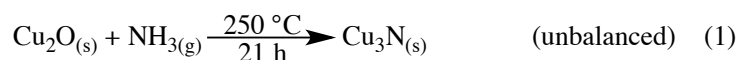
Figure 5. Density of State (DOS) curves for Cu_2O (a), Cu_3N (b), and CuO (c). Total DOS is depicted in black. Partial DOS (pDOS) are given in copper (Cu), red (O), and blue (N).

Scheme 1.

$$Cu_2O_{(s)} + NH_{3(g)} \xrightarrow[\text{21 h}]{\text{250 °C}} Cu_3N_{(s)} \qquad \text{(unbalanced)} \quad (1)$$

$$Cu_2O_{(s)} + (NH_2)_2CO_{(g)} \xrightarrow[\text{6 h}]{\text{190 °C}} Cu_3N_{(s)} \qquad \text{(unbalanced)} \quad (2)$$

Spontaneous decomposition of Cu₃N to CuO. During the humid summer time, we observed spontaneous decomposition of the Cu_3N nanocrystals over a period of several days. To track their fate, we characterized the product using powder XRD and determined that it was made of nanocrystalline monoclinic (tenorite) CuO (Figure S1, Scheme 2). The tenorite CuO unit cell contains tetracoordinate cupric (Cu^{2+}) ions in an approximately square planar configuration (Figure 2c). Scherrer particle sizes obtained from XRD are 16 nm and 12 nm for CuO nanocrystals derived from NH_3- and urea-made Cu_3N, respectively. TEM shows that the CuO produced is made of highly aggregated clusters (100-140 nm) of small nanocrystals (13 ± 3 nm) (Figure 4c,e and Table 1).

Reported experimental band gap values for CuO lie in the 1.2-1.5 eV range (see below).[43,44] The black-colored CuO produced here has a slightly redder absorption edge (*ca.*

850 nm) than Cu$_3$N (Figure 5). DOS calculations show that the electronic structure of CuO is much more complicated than Cu$_2$O or Cu$_3$N (Figure 5). The most notable feature of the DOS curve for CuO is the peak located at the Fermi level. In traditional band theory, this would indicate CuO is metallic. Along with CoO and NiO, CuO belongs to a class of late metal oxides known as Mott insulators. In addition to the strong Coulombic interactions mentioned above, a recent investigation, focused on elucidating the electronic structure of CuO, found that spin-orbit coupling (SOC) also plays an important role.[45] Without SOC, the valence band ends 1.17 eV above the Fermi level, after which there is a small gap of 0.49 eV, consistent with prior theoretical estimates.[41] However, calculations accounting for SOC found the band gap to start at the Fermi level and be 1.2 eV in magnitude.[45] This value agrees better with experimental values, and supports the claim that SOC is an important factor for this class of compounds.

To elucidate what caused the decomposition of Cu$_3$N nanocrystals, we attempted to react them with water under argon (oxygen-free), with dry oxygen (water-free), or with water and oxygen together as control experiments (eqs 3, 4, and 5, respectively, in Scheme 2). As shown in Figure 6, treating Cu$_3$N nanocrystals with water under an oxygen-free Ar atmosphere at room temperature (R.T.) for 15 days did not result in any observable change. The same was true when dry (moisture-free) O$_2$ was used. In contrast, Cu$_3$N completely transformed to nanocrystalline CuO in the presence of both water and O$_2$ (Figure 6). This reproducible result is independent of the original nitridation source (NH$_3$ or urea) that was employed in making Cu$_3$N with very different sizes and morphologies. This result is also consistent with our observation that Cu$_3$N decomposition occurred faster during the humid summer months than during the dry winter months.
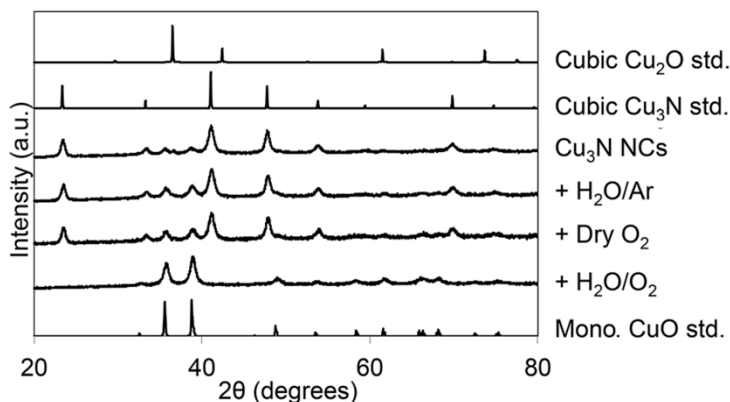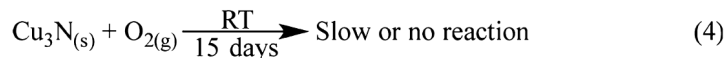
Scheme 2.

$$Cu_3N_{(s)} + H_2O_{(l)} \xrightarrow[\text{15 days}]{RT / Ar} \text{Slow or no reaction} \qquad (3)$$

$$Cu_3N_{(s)} + O_{2(g)} \xrightarrow[\text{15 days}]{RT} \text{Slow or no reaction} \qquad (4)$$

$$Cu_3N_{(s)} + H_2O_{(l)} + O_{2(g)} \xrightarrow[\text{15 days}]{RT} CuO_{(s)} \quad \text{(unbalanced)} \quad (5)$$

Figure 6. Experimental powder XRD patterns obtained before and after treating Cu_3N nanocrystals (NCs) with H_2O under Ar (O_2-free), dry O_2 (H_2O-free), and H_2O plus O_2. Reported powder XRD patterns for bulk cubic Cu_2O, cubic (anti-ReO_3) Cu_3N, and monoclinic (tenorite) CuO are shown for comparison (all reactions were performed at R.T. for 15 d).

Tracing the fate of nitrogen after Cu_3N decomposition. Two nonmutually exclusive, possible nitrogen-containing products of Cu_3N decomposition are ammonia (NH_3) and molecular nitrogen (N_2). We first suspected that NH_3 was produced after observing an increase in the pH of the original solution exposed to the Cu_3N nanocrystals from slightly acidic or neutral before reaction, to basic after the decomposition of Cu_3N to CuO was complete. To further examine this issue, we sought to confirm whether NH_3 was produced and, if so, to measure exactly how much NH_3 was produced, using the colorimetric indophenol method (eq 6 in Scheme 3 and Figure S2).[46,47] As shown in Table 2, similar amounts of ammonia were released upon Cu_3N decomposition regardless of the source of

nitrogen originally used for nitridation (NH_3 or urea). In all cases, the experimentally measured chemical yield of NH_3 remained constant and equal to 60% relative to the initial amount of Cu_3N.
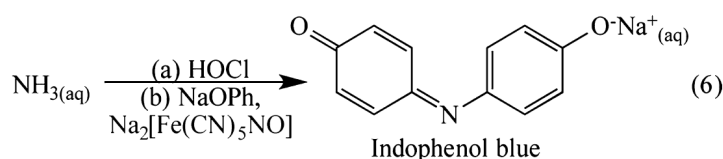
Scheme 3. Colorimetric Indophenol Quantification of NH_3.

$$NH_{3(aq)} \xrightarrow[\text{(b) NaOPh, } Na_2[Fe(CN)_5NO]]{\text{(a) HOCl}} \quad \text{Indophenol blue} \quad (6)$$

Table 2. Colorimetric determination of NH_3 produced from Cu_3N decomposition using the indophenol method.

	Cu_3N^a	NH_3	
	moles^a	moles^b	% yield^c
Cu_3N (NH_3)	$5.13 \pm 0.07 \times 10^{-5}$	$3.27 \pm 0.04 \times 10^{-5}$	63.7 ± 0.9
Cu_3N (urea)	$5.33 \pm 0.05 \times 10^{-5}$	$2.98 \pm 0.04 \times 10^{-5}$	56 ± 1
^{a}Decomposition reactions were carried out in 10 mL of deionized water. ^{b}Small, 100 μL aliquots were further diluted with 10 mL of deionized water to produce the solutions in Figure S2. ^{c}Based on the total amount of nitrogen (from Cu_3N).			

Thermodynamic rationale of CuO formation. In principle, formation of N_2 or NH_3 from Cu_3N decomposition (oxidation to CuO) could be rationalized by either of the balanced eqs 7 or 8 (Scheme 4). The enthalpies of formation (ΔH_f) of all reactants and products in these equations are known, including those of Cu_3N (ΔH_f = 77 kJ/mol)[48,49] and CuO (ΔH_f = -157.3 kJ/mol)[50] (near standard conditions). Using these values, the enthalpies of reactions (ΔH_r) (7) and (8) are calculated to be -549 kJ/mol and -197 kJ/mol, respectively. Therefore, decomposition of Cu_3N to exclusively N_2 *vs.* NH_3 (reaction 7 *vs.* 8) is favored enthalpically by *ca.* 350 kJ/mol (Figure 7). In other words, there is an inverse relationship between the enthalpy of the Cu_3N decomposition and the amount of N_2 produced by this reaction (relative to NH_3). Unfortunately, we are presently unable to exactly calculate the free energies (ΔG_r)

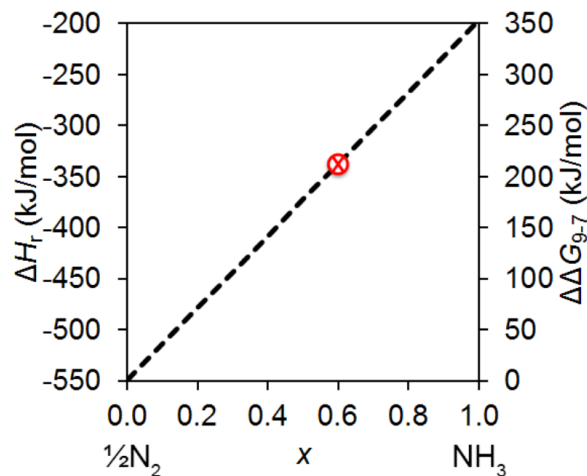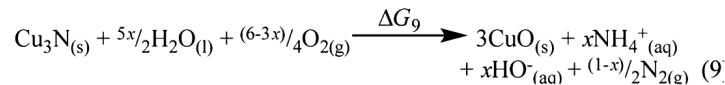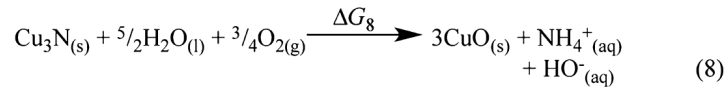of reactions (7) and (8), because the free energy of formation (ΔG_f) of Cu_3N remains unknown.

Scheme 4.

$$Cu_3N_{(s)} + {}^3/_2O_{2(g)} \xrightarrow{\Delta G_7} 3CuO_{(s)} + {}^1/_2N_{2(g)} \qquad (7)$$

$$Cu_3N_{(s)} + {}^5/_2H_2O_{(l)} + {}^3/_4O_{2(g)} \xrightarrow{\Delta G_8} 3CuO_{(s)} + NH_4{}^+{}_{(aq)} + HO^-{}_{(aq)} \qquad (8)$$

$$Cu_3N_{(s)} + {}^{5x}/_2H_2O_{(l)} + {}^{(6-3x)}/_4O_{2(g)} \xrightarrow{\Delta G_9} 3CuO_{(s)} + xNH_4{}^+{}_{(aq)} + xHO^-{}_{(aq)} + {}^{(1-x)}/_2N_{2(g)} \qquad (9)$$
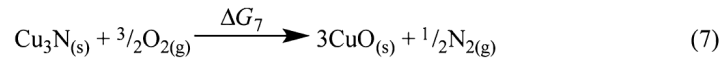

Figure 9. Change in enthalpy (ΔH_r) and free energy (ΔG_r) of Cu_3N decomposition to CuO as a function of NH_3 chemical yield (percent = $100x$). The circled cross marker in red represents the NH_3 yield (x) observed in this study.

In spite of the large enthalpic preference for exclusive N_2 production, this was not observed experimentally. On the basis of our observations that H_2O is required for Cu_3N decomposition to occur and that NH_3 is produced in 60% yield based on the initial amount of Cu_3N ((x = 0.6, Table 2), we conclude that this reaction proceeds through a complex stoichiometry that involves the concomitant release of both N_2 and NH_3, according to eq 9.

We are able to calculate the true thermodynamic cost of ammonia production by considering the difference in Gibb's free energies between reactions 9 and 7 ($\Delta\Delta G_{9-7}$), as follows:

$$\Delta\Delta G_{9-7} = \Delta G_9 - \Delta G_7 = x\Delta G_{f_{NH4^+(aq)}} + x\Delta G_{f_{HO^-(aq)}} - \frac{5x}{2}\Delta G_{f_{H2O(l)}} + \frac{x}{2}\Delta G_{f_{N2(g)}} - \frac{3x}{4}\Delta G_{f_{O2(g)}}$$

In this equation, $3\Delta G_{f_{CuO(s)}}$ and $\Delta G_{f_{Cu3N(s)}}$ have been canceled out. In addition, by definition both $\Delta G_{f_{N2(g)}}$ and $\Delta G_{f_{O2(g)}}$ are zero under ideal or near-ideal conditions (25 °C, 1 atm). This yields:

$$\Delta\Delta G_{9-7} = x\Delta G_{f_{NH4^+(aq)}} + x\Delta G_{f_{HO^-(aq)}} - \frac{5x}{2}\Delta G_{f_{H2O(l)}}$$

$$= -x(79 \text{ kJ/mol}) - x(157 \text{ kJ/mol})$$

$$+ (5x/2)(237 \text{ kJ/mol})^{47} = x(358 \text{ kJ/mol})$$

Figure 7 shows a plot of $\Delta\Delta G_{9-7}$ as a function of chemical yield of NH_3 based on the initial amount of Cu_3N. The experimentally observed value of 60% is 72 kJ/mol less favorable by free energy compared to when (if) no ammonia is produced. This strongly indicates that the role of H_2O (and thus NH_3 production) is to facilitate the kinetics of the reaction by lowering the energy barrier for Cu_3N decomposition to CuO.

Conclusion

In summary, nanocrystalline Cu_3N was synthesized from nanocrystalline Cu_2O and one of two nitrogen sources, ammonia (NH_3) or urea (H_2NCONH_2). Using urea leads to slightly more phase-pure Cu_3N, as observed by XRD. In addition, the use of ammonia as the nitridation (ammonolysis) reagent requires a longer reaction time and higher temperature. TEM reveals that the cubic morphology of the initial Cu_2O nanocrystals is lost upon nitridation to Cu_3N. Nitridation with ammonia produces clusters of spherical particles whereas nitridation with urea produced a mixture of several different morphologies (rods, sheets, and aggregates). Electronic structure, calculations of the DOS appear to

underestimate, but agree with the presence of, a band gap of under 1 eV for both Cu_2O and Cu_3N phases.

Cu₃N nanocrystals spontaneously decompose to nanocrystalline CuO at room temperature. Control experiments show that both air (O_2, an oxidant) and moisture (H_2O, for hydrolysis to NH_3) are necessary for this transformation to take place. Cu_3N decomposition occurs within 15 days to produce substoichiometric amounts of ammonia. Specifically, ammonia was produced in 60% chemical yield during Cu_3N decomposition, as measured using the colorimetric indophenol method. Because Cu_3N decomposition requires H_2O and produces substoichiometric amounts of NH_3, we conclude that this reaction proceeds through a complex stoichiometry that involves the concomitant release of both N_2 and NH_3. This is a thermodynamically unfavorable outcome, strongly indicating that H_2O (and thus NH_3 production) facilitate the kinetics of the reaction by lowering the energy barrier for Cu_3N decomposition. Additional studies will be required to assess the potential reversibility and catalytic usefulness of this transformation.

Acknowledgement

References

[1] Wang, D.; Li, Y. *Chem. Commun.* **2011**, *47*, 3604–3606.

[2] Xi, P.; Xu, Z.; Gao, D.; Chen, F.; Xue, D.; Tao, C.-L.; Chen, Z.-N. *RSC Adv.* **2014**, *4*, 14206–14209.

[3] Nakamura, T.; Hayashi, H.; Hanaoka, T.-A.; Ebina, T. *Inorg. Chem.* **2013** *53*, 710–715.

[4] Wu, H.; Chen, W. *J. Am. Chem. Soc.* **2011**, *133*, 15236–15239.

[5] In, S-I.; Vaughn II, D. D.; Schaak, R. E. *Angew. Chem. Int. Ed.* **2012**, *51*, 3915–3918.

[6] Lee, B. S.; Yi, M.; Chu, S. Y.; Lee, J. Y.; Kwon, H. R.; Lee, K. R.; Kang, D.; Kim, W. S.; Lim, H. B.; Lee, J.; Youn, H-J.; Chi, D. Y.; Hur, N. H. *Chem. Commun.* **2010**, *46*, 3935–3937.

[7] Desmoulins-Krawiec, S.; Aymonier, C.; Loppinet-Serani, A.; Weill, F.; Gorsse, S.; Etourneau, J.; Cansell, F. *J. Mater. Chem.* **2004**, *14*, 228–232.

[8] Cansell, F.; Aymonier, C.; Loppinet-Serani, A. *Curr. Opin. Solid State Mater. Sci.* **2003**, *7*, 331–340.

[9] Cansell, F.; Chevalier, B.; Demourgeues, A.; Etourneau, J.; Even, C.; Garrabos, Y.; Pessey, V.; Petit, S.; Tressaud, A.; Weill, F. *J. Mater. Chem.* **1999**, *9*, 67–75.

[10] Choi, J.; Gillan, E. G. *Inorg. Chem.* **2005**, *44*, 7385–7393.

[11] Trivedi, M.; Singh, G.; Kumar, A.; Rath, N. P. *RSC Adv.* **2014**, *4*, 34110–34116.

[12] Paniconi, G.; Stoeva, Z.; Doberstein, H.; Smith, R. I.; Gallagher, B. L.; Gregory, D. H. *Solid State Sciences* **2007**, *9*, 907–913.

[13] Gordillo, N.; Gonzalez-Arrabal, R.; Martin-Gonzalez, M. S.; Olivares, J.; Rivera, A.; Briones, F.; Agulló-López, F.; Boerma, D. O. *J. Cryst. Growth* **2008**, *310*, 4362–4367.

[14] Hadian, F.; Rahmati, A.; Movla, H.; Khaksar, M. *Vacuum* **2012**, *86*, 1067–1072.

[15] Gordillo, N.; Rivera, A.; Grötzschel, R.; Munnik, F.; Güttler, D.; Crespillo, M. L.; Agulló-López, F.; Gonzalez-Arrabal, R. *J. Phys. D: Appl. Phys.* **2010**, *43*, 345301-1–9.

[16] Gonzalez-Arrabal, R.; Gordillo, N.; Martin-Gonzalez, M. S.; Ruiz-Bustos, R.; Agulló-López, F. *J. Appl. Phys.* **2010**, *107*, 103513-1–7.

[17] Deshmukh, R.; Schubert, U. *Eur. J. Inorg. Chem.* **2013**, *14*, 2498–2504.

[18] Deshmukh, R.; Schubert, U. *J. Mater. Chem.* **2011**, *21*, 18534–18536.

[19] Baiker, A.; Maciejewski, M. *J. Chem. Soc., Faraday Trans. 1* **1984**, *80*, 2331–2341.

[20] Filipič, G.; Cvelbar, U. *Nanotechnology* **2012**, *23*, 194001 1–16.

[21] Zhang, Q.; Zhang, K.; Xu, D.; Yang, G.; Huang, H.; Nie, F.; Liu, C.; Yang, S. *Prog. Mater. Sci.* **2014**, *60*, 208–337.

[22] Kuo, C.-H.; Huang, M. H. *Nano Today* **2010**, *5*, 106–116.

[23] Lignier, P.; Bellabarba, R.; Tooze, R. P. *Chem. Soc. Rev.* **2012**, *41*, 1708–1720.

[24] Fan, X. Y.; Wu, Z. G.; Yan, P. X.; Geng, B. S.; Li, H. J.; Li, C.; Zhang, P. J. *Material Letters* **2008**, *62*, 1805–1808.

[25] Lesch, N.; Karduck, P.; Cremer, R.; Richthofen, A. V. *Fresenius J. Anal. Chem.* **1998**, *361*, 604–607.

[26] Yue, G. H.; Yan, P. X.; Wang, J. *J. of Cryst. Growth* **2005**, *274*, 464–468.

[27] Asano, M.; Umeda, K.; Tasaki, A. *Jpn. J. Appl. Phys.* **1990**, *29*, 1985–1986.

[28] Wang, Z.; Wang, H.; Wang, L.; Pan, L. *Cryst. Res. Technol.* **2009**, *44*, 624–628.

[29] Weatherburn, M. W. *Anal. Chem.* **1967**, *39*, 971–974.

[30] Searle, P.L. *Analyst* **1984**, *109*, 549–568.

[31] Kresse, G.; Furthmüller, J. *Comput. Mater. Sci.* **1996**, *6*, 15–50.

[32] Kresse, G. *Phys. Rev. B* **1996**, *54*, 11169–11186.

[33] Kresse, G. *Phys. Rev. B* **1999**, *59*, 1758–1775.

[34] Monkhorst, H. J.; Pack, J. D. *Phys. Rev. B* **1976**, *13*, 5188–5192.

[35] Blöchl, P. E. *Phys. Rev. B* **1994**, *50*, 17953–17979.

[36] Perdew, J. P.; Burke, K.; Ernzerhof, M. *Phys. Rev. Lett.* **1996**, *77*, 3865–3868.

[37] Scanlon, D.; Walsh, A.; Morgan, B.; Watson, G.; Payne, D.; Egdell, R. *Phys. Rev. B* **2009**, *79*, 035101-1–7.

[38] Raebiger, H.; Lany, S.; Zunger, A. *Phys. Rev. B* **2007**, *76*, 045209-1–5.

[39] Xiao, J.; Li, Y.; Jiang, A. *J. Mater. Sci. Technol.* **2011**, *27*, 403–407.

[40] Ching, W.; Xu, Y.-N.; Wong, K. *Phys. Rev. B* **1989**, *40*, 7684–7695.

[41] Hahn, U.; Weber, W. *Phys. Rev. B* **1996**, *53*, 12684–12693.

[42] Elliott, R. *Phys. Rev.* **1957**, *108*, 1384–1389.

[43] Marabelli, F.; Parravicini, G. B.; Salghetti-Drioli, F. *Phys. Rev. B* **1995**, *52*, 1433–1436.

[44] Serin, N.; Serin, T.; Horzum, Ş.; Çelik, Y. *Semicond. Sci. Technol.* **2005**, *20*, 398–401.

[45] Ekuma, C. E.; Anisimov, V. I.; Moreno, J.; Jarrell, M. *Eur. Phys. J. B* **2014**, *87*, 23-1–6.

[46] Vela, J.; Stoian, S.; Flaschenriem, C. J.; Münck, E.; Holland, P. L. *J. Am. Chem. Soc.* **2004**, *126*, 4522–4523.

[47] Yandulov, D. V.; Schrock, R. R. *Science* **2003**, *301*, 76–78.

[48] Elder, S. H.; DiSalvo, F. J.; Topor, L.; Navrotsky, A. *Chem. Mater.* **1993**, *5*, 1545–1553.

[49] Caskey, C. M.; Richards, R. M.; Ginleya, D. S.; Zakutayeva, A. *Mater. Horiz.* **2014**, *1*, 424–430.

[50] CRC Handbook of Chemistry and Physics, 95th ed.; Boca Raton, FL, 2013.
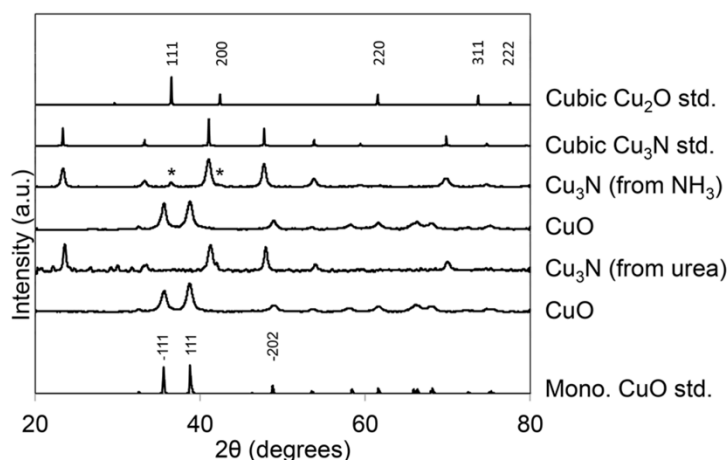
Supporting Information

Figure S1. Experimental powder XRD patterns obtained for nanocrystalline Cu_3N (from nitridation of Cu_2O with NH_3 or urea) before and after decomposition (* = Cu_2O impurity). Reported powder XRD patterns for bulk cubic Cu_2O, cubic (anti-ReO_3) Cu_3N, and monoclinic (tenorite) CuO are shown for comparison.
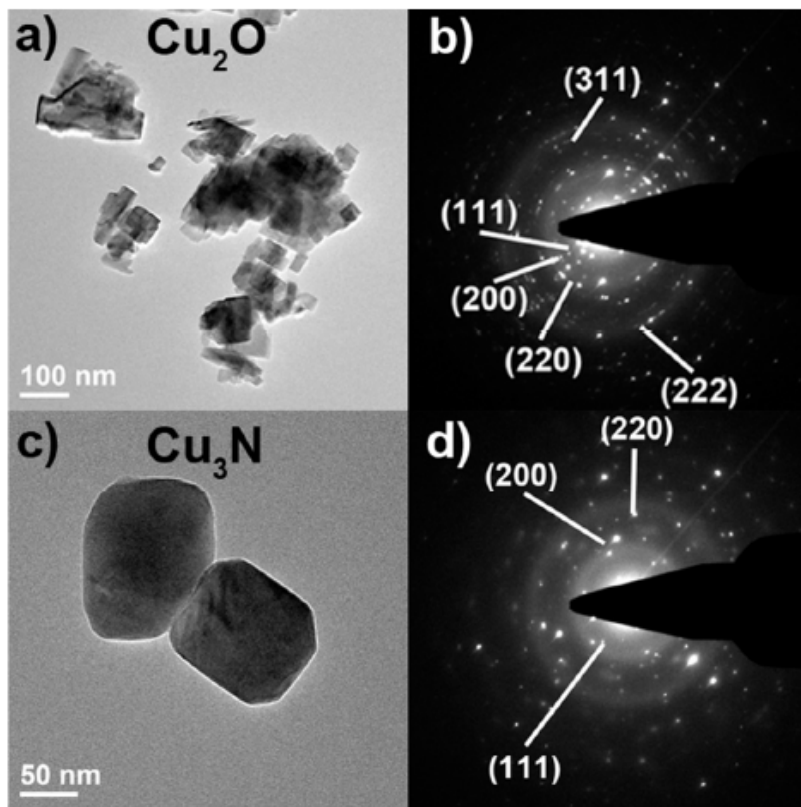
Figure S2. Representative TEM micrographs of nanocrystalline Cu_2O (a), SAED pattern for Cu_2O (b), Cu_3N made from urea (c), and its corresponding SAED pattern (d). These patterns show the presence of reflections consistent with the lattice planes of their respective crystal types. The one major reflection that is not observed is the (100) plane in Cu_3N. This is due to a large d spacing of 3.81 Å. The reciprocal lattice spacing is thus very small; causing the powder ring to be blocked by the central beam making it unobservable. The consistency between SAED and powder diffraction data confirms the phase assignments. However, impurities are observed within both sets of data. The impurities present in the SAED are visible as the reflections contained between the powder rings. Based solely on SAED characterization of these crystal structures would not be reliable. For Cu_3N, powder diffraction showed that these impurities are minor phases primarily composed of unreacted Cu_2O.
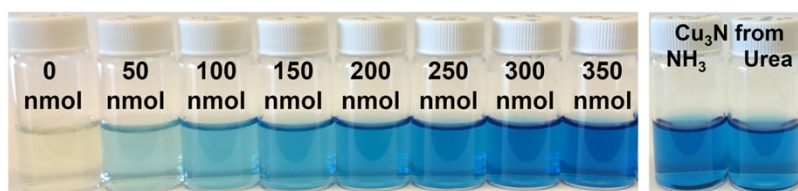

Figure S3. Representative calibration and sample solutions used to quantify the amount of ammonia produced from Cu_3N decomposition using the indophenol method (in all cases, the total volume was 10 mL).

CHAPTER 4

EXPLORING THE THERMAL DECOMPOSITION OF METHYLAMMONIUM LEAD HALIDES (CH$_3$NH$_3$PbX$_3$, WHERE X = I, Br or Cl)

Malinda D. Reichert, Long Men, Bryan Rosales and Javier Vela

Abstract

Perovskites are promising, new materials for solar cells. The thermal stability has been investigated and different pathways are reported for decomposition. In the literature decomposition of methylammonium lead halides decompose to CH$_3$NH$_2$X followed by HX or HX followed by CH$_3$NH$_2$. However, further investigation by thermogravimetric analysis/differential scanning calorimetry with mass spectrometry and Fourier-Transform infrared spectroscopy (TGA/DSC/MS/FT-IR) for gas evolution reveals a different decomposition pathway occurring for each halide. Bulk methylammonium lead iodide and methylammonium lead bromide both decompose by a similar route that differs from that of bulk methylammonium lead chloride. For the iodide and bromide, ammonia and methyl halide evolve, and the bromide shows evolution of methylamine. The chloride acts similarly to what is previously reported in the literature, producing methylamine and HCl. However, FT-IR peaks for HCl overlap with the CH$_3$ stretching of methylamine making it difficult to distinguish. Using this data and decomposition pathways, a way to achieve long-term thermal stability may be determined for methylammonium lead halide perovskites for solar cells.

Introduction

Interest in organic-inorganic lead halide perovskites as light harvesters in photovoltaics flourished the past few years, which lead to a power conversion efficiency (PCE) of 19% seen in methylammonium lead halide perovskites.[1] These materials were initially used in dye sensitized solar cells but are now commonly used in solid-state devices

due to dissolution of the perovskite in the liquid electrolyte of dye sensitized cells.[2,3,4] Other advantages of these materials are low production cost due to solution processability, tunable optical properties, high charge mobilities, and large absorption coefficients.[5] However, $CH_3NH_3PbX_3$ (where X = I, Br, or Cl) perovskites also have drawbacks for use in solar cells.

Methylammonium lead halides are susceptible to degradation from humidity, light, electron beam and heat. [4,6-9] These stability issues, along with being toxic, make the use of these materials problematic for solar cells. The moisture stability of perovskites was studied, and they were found to decompose due to the hygroscopic amine salts.[10] Above 55% humidity, the perovskite degraded, as evidenced by a color change from dark brown to yellow. However, at low humidity (below 50%), $CH_3NH_3PbI_3$ does not degrade significantly as evidenced from the PCE remaining stable. A mixed halide system, $CH_3NH_3Pb(I_{1-x}Br_x)_3$, displayed decreased humidity sensitivity and the efficiency remained relatively unchanged with increasing bromine content. Previously, it was shown $CH_3NH_3PbI_3$ is more moisture sensitive than $CH_3NH_3PbBr_3$.[11] A mechanism proposed for the degradation of $CH_3NH_3PbI_3$ under light produces CH_3NH_2 and HI, leaving PbI_2.[12] Also, another mixed perovskite, $CH_3NH_3PbI_2Cl$ was stable to processing in air and to prolonged light exposure (1000 h under simulated full sunlight) compared to $CH_3NH_3PbI_3$.[13] Looking to stabilize these materials, others have observed many things. For instance, introducing an aluminum oxide modification increased the moisture stability by protecting the $CH_3NH_3PbI_3$ sensitized solar cells from moisture and sunlight.[14] Recently, long-term stabilization of the materials has been examined, for instance; using carbon nanotube/polymer composites as stable hole collection layers.[6,15] A perovskite solar cell with the composites showed notable moisture and thermal

stability. Others have also looked at using a hole transport material-free solar cell with a carbon back contact, which showed a resistance to water and stability for greater than 1000 hours in ambient air under sunlight.[6,16] However, a better understanding of degradation mechanisms of the perovskite would help improve the long-term stability of the perovskite solar cells.

As a collaboration with the Ames Lab DOE Nanodomains group, our group looked at the controllable syntheses of methylammonium lead halide materials for solar cells. Various morphologies of $CH_3NH_3PbX_3$ (X = I or Br) nanocrystals were synthesized using different solvents and capping ligands.[17] Single particle luminescence shows a shape-correlated PL emission with little photobleaching. However, during this study, the perovskite materials were sensitive to the TEM electron beam as well as humidity and high temperature, as reported in literature.

Previously, the structural changes in $CH_3NH_3PbX_3$ (where X = I, Br, or Cl) were probed by thermal and spectroscopic methods.[18-25] Recently, groups looked at the thermal stability and decomposition of the perovskites at higher temperatures. They studied the effect of temperature on photovoltaic performance, using thermogravimetric analysis (TGA), and found perovskite quantum dots are stable up to 300 °C.[26] DSC of $CH_3NH_3PbI_3$ shows there is a phase transition at low temperature from the cubic to tetragonal phase.[27] TGA of the same material saw a 66% mass loss corresponding to complete decomposition of the perovskite to lead metal. Another report on the thermal properties of $CH_3NH_3PbX_3$ (X = I or Cl) and its precursors determined that $CH_3NH_3PbI_3$ decomposed by consecutive loss of HI and CH_3NH_2 (20% and 5-6% mass losses).[28] The chloride derivative decomposed to $PbCl_2$ by losing CH_3NH_3Cl.[28] Another study reported the thermal decomposition of both $CH_3NH_3SnI_3$ and

$CH_3NH_3PbI_3$.[29] These results determined that $CH_3NH_3PbI_3$ had a decomposition that started after 300 °C and again had a mass loss corresponding to production of CH_3NH_3I and HI. The thermal decomposition of $CH_3NH_3PbBr_3$ monitored by TGA showed the crystals were stable to 238 °C but decomposed quickly due to escape of CH_3NH_2 and HBr.[30] These three reports used only thermal analysis (TGA and/or DSC) to determine the decomposition of the perovskite materials. Another group used a tandem calorimetric-spectroscopic study to directly correlate evolved gases with calorimetric events.[31] They looked at the decomposition of $CH_3NH_3PbI_3$ and a mixed system $CH_3NH_3PbI_{3-x}Cl_x$ in DMF, and found that for the iodide perovskite at 230 °C along with DMF, weak features from ammonia appear. For the mixed iodide-chloride, peaks from DMF are seen along with signals for CH_3NH_2 and HCl.

Although the thermal stability of various types of methylammonium lead halide perovskite materials has been investigated, not all three halides (I, Br, and Cl) or their evolved gases have been explored. In this chapter, we investigate the thermal stability of the bulk $CH_3NH_3PbX_3$ (where X = I, Br, or Cl) perovskite materials to determine how these materials decompose. Using thermogravimetric analysis and differential scanning calorimetry coupled with a quadrupole mass spectrometer (QMS) and Fourier-Transform infrared (FT-IR) spectrometer, the decomposition temperature and evolved gas products were analyzed. Using this data to understand decomposition pathways may provide a way to achieve long-term thermal stability for organometal halide perovskite materials for solar cells.

Experimental

Materials. Lead(II) iodide (99%), lead(II) bromide (≥98%), lead(II) chloride (99.999%), methylamine solution (33 wt.% in absolute ethanol), N,N-dimethylformamide

(DMF, anhydrous, 99.8%) were purchased from Sigma-Aldrich; hydroiodic acid (ACS, 55-58%), hydrobromic acid (ACS, 47-49%) from Alfa Aesar; and hydrochloric acid (37%), acetonitrile (99.9%), ethanol (200 proof), toluene (99.9%) from Fisher.

Synthesis. *Ammonium halides*. Hydrogen halides were prepared by a modified literature procedure.[13,17] Hydroiodic acid (10 mL, 0.075 mol), hydrobromic acid (8.6 mL, 0.075 mol), or hydrochloric acid (6.32 mL, 0.075 mol) was added to a solution of excess methylamine (24 mL, 0.192 mol) in ethanol (50 mL) at 0 °C, and the mixture stirred for 2 h. The solution was concentrated under vacuum, and the resulting powder was dried under dynamic vacuum at 60 °C for 12 h, then recrystallized from ethanol. *Methylammonium lead halides (X = I, Br or Cl)*. Bulk perovskites were prepared by a modified literature procedure.[17,32] *$CH_3NH_3PbI_3$*. PbI_2 (4.1 mg, 0.089 mmol) and CH_3NH_3I (3.9 mg, 0.025 mmol) were dissolved in acetonitrile (20 mL). Toluene (15 mL) was added by fast injection into the precursor mixture (4 mL CH_3CN solution) while stirring. The solution was stirred overnight and then centrifuged (10 min at 4000 rpm). The precipitate was re-dissolved in toluene. *$CH_3NH_3PbBr_3$*. $PbBr_2$ (7.4 mg, 0.02 mmol) and CH_3NH_3Br (2.2 mg, 0.02 mmol) were dissolved in DMF (0.5 mL). Toluene (15 mL) was added by fast injection into the precursor mixture (0.05 mL DMF solution) while stirring. The solution was stirred overnight and then centrifuged (10 min at 4000 rpm). The precipitate was re-dissolved in toluene. *$CH_3NH_3PbCl_3$*. $PbCl_2$ (5.3 mg, 0.02 mmol) and CH_3NH_3Cl (1.3 mg, 0.02 mmol) dissolved in DMF (0.5 mL). Toluene (15 mL) was added by fast injection into the precursor mixture (0.05 mL DMF solution) while stirring. The solution was stirred overnight and centrifuged (10 min at 4000 rpm). The precipitate was re-dissolved in toluene.

Structural characterization. *X-Ray Diffraction.* Powder X-ray diffraction (XRD) data were measured using Cu Kα radiation on a Rigaku Ultima U4.

Thermal analysis. *Thermogravimetric analysis (TGA) and differential scanning calorimetry (DSC).* Measurements were taken using a Netzsch STA449 F1 Jupiter[®] TGA/DSC instrument coupled to a Quadrupole Mass Spectrometer (QMS) and Bruker Tensor 27 FT-IR spectrometer. Using ~10 mg samples in alumina crucibles were heated from 40 °C to 500 °C using Ar as the carrier gas and 10 °C /min for the ramp rate.

Results and Discussion

With the great attention given to solar energy and the increased interest in $CH_3NH_3PbX_3$ (X = I, Br, or Cl) perovskites for solar cells, the decomposition of these materials must be understood to devise means for enhancing the stability for commercialization of the solar cells. In this chapter, the thermal stability of the three different bulk $CH_3NH_3PbX_3$ (X = I, Br, or Cl) perovskite materials is examined along with suggestions to increase the stability from the observed results.

Bulk $CH_3NH_3PbX_3$ (X = I, Br, or Cl) perovskite materials were synthesized using a reported method by mixing the lead halide with the corresponding methylammonium halide (equation 1).[17,32] Powder X-ray diffraction was used to demonstrate that the samples were crystalline and had the correct material. Figure 1 shows the three different bulk halide materials along with the standard bulk pattern for iodide and simulated patterns for the bromide and chloride. Both the bromide and chloride are cubic while the iodide is tetragonal. Once the samples were determined to be the correct composition from the powder XRD patterns, thermal analysis using TGA and DSC coupled to FT-IR and MS, was performed.

$$PbX_2 + CH_3NH_3X \rightarrow CH_3NH_3PbX_3 \qquad (1)$$

CH₃NH₃PbI₃

For the iodide, as previously mentioned, literature found that decomposition occurred through two mass losses; one of 20% and the second of 5-6%.[28] The first is due to decomposition of the lead methylammonium iodide to HI and then CH_3NH_2. Another paper also reported the decomposition to produce CH_3NH_2I and HI.[27,31] However, using the Netzsch TGA/DSC system, we saw a different products. Table 1 shows the main compounds that we believe could be present with the decomposition, molecular weights, and their weight percentage of the methylammonium lead iodide.
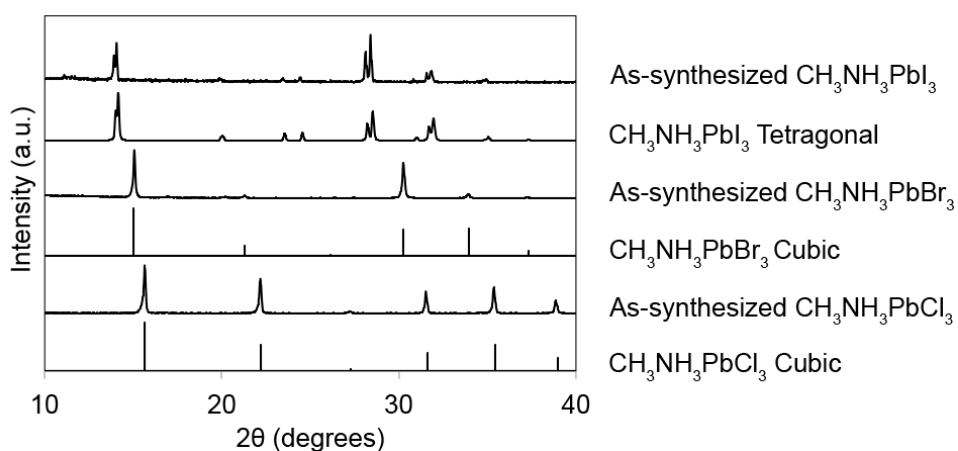

Figure 1. Powder XRD patterns for as synthesized $CH_3NH_3PbX_3$ (X = I, Br, or Cl) bulk perovskites along with standard (iodide) or simulated (bromide and chloride) patterns.

Table 1. Compound, molecular weight and mass percentage of $CH_3NH_3PbI_3$.		
Compound	**MW (g/mol)**	**Percentage (%)**
$CH_3NH_3PbI_3$	620	100
PbI_2	461	74
CH_3NH_2	31	5
NH_3	17	2.7
CH_3I	142	23
HI	128	21

The thermogravimetric analysis (TGA) measurement for the $CH_3NH_3PbI_3$, shown in Figure 2, shows a one-step decomposition starting at 340 °C. The mass loss is about 26%, which corresponds to only inorganic lead iodide remaining and is also similar to literature results. The melting point of PbI_2 is 410 °C.[33] Furthermore, CH_3NH_2I sublimes at 247 ± 26 °C and CH_3NH_2 at 247 ± 26 °C.[28] Differential scanning calorimetry (DSC) displays an endothermic transition at 358 °C which may be from both the decomposition of the organic cation and melting of PbI_2. DSC data had not been shown for temperatures greater than 200 °C in literature for $CH_3NH_3PbI_3$. In literature, an endothermic peak is reported at approximately 60 °C which was assigned to a tetragonal to cubic phase transition.[27,28,31,34] This peak is not seen in Figure 2, which may be due to the transition just lowering the symmetry and not a chemical bond breakage or formation. Therefore, the change in heat capacity is low and no signal is seen.[29]
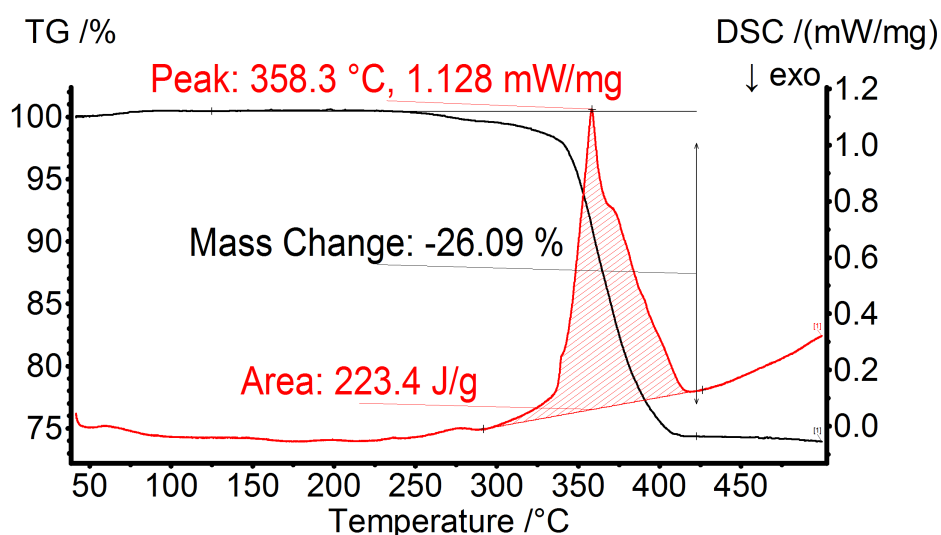

Figure 2. TGA (black) and DSC (red) for bulk $CH_3NH_3PbI_3$ 40 °C to 500 °C.

Recently, FT-IR of the evolved gasses from methylammonium lead iodide and chloride were examined while in DMF.[27] However, this is the first report of the thermal

decomposition of the perovskites without solvent using the Netzsch system. Figure 3 shows the 3D FT-IR plot of the evolved gases from 500 to 4500 wavenumbers (cm^{-1}) and 40 to 500 °C. This plot shows that the main evolution of gases starts above 300 °C. The IR spectrum of gases evolved at different temperatures are shown in Figure 4. At lower temperature (328 °C), characteristic peaks of both ammonia and iodomethane are observed.[35] As temperature increases (346 and 362 °C), both compounds still evolve and account for the 26% weight loss in the TGA (Figure 2). Furthermore, peaks at 950, 1600 and 3300-3400 cm^{-1} are due to ammonia and are NH symmetrical deformations, NH degenerate deformations, and NH symmetric stretches, respectively.[36] Peaks at about 1250 and 3000 cm^{-1} are due to iodomethane and CH_3 symmetrical deformations and CH_3 symmetrical stretching, respectively.[36] Previously in the literature, HI was said to be evolved; however, from the FT-IR spectra in Figure 3, HI is not observed. Figure 5 shows an expanded portion of the IR where HI should be seen along with a standard spectrum of HI from the Pacific Northwest National Laboratory database.[37] Furthermore, the decomposition of $CH_3NH_3PbI_3$ follows the decomposition of CH_3NH_3I reported in the literature where both NH_3 and CH_3I gases evolve.[31]

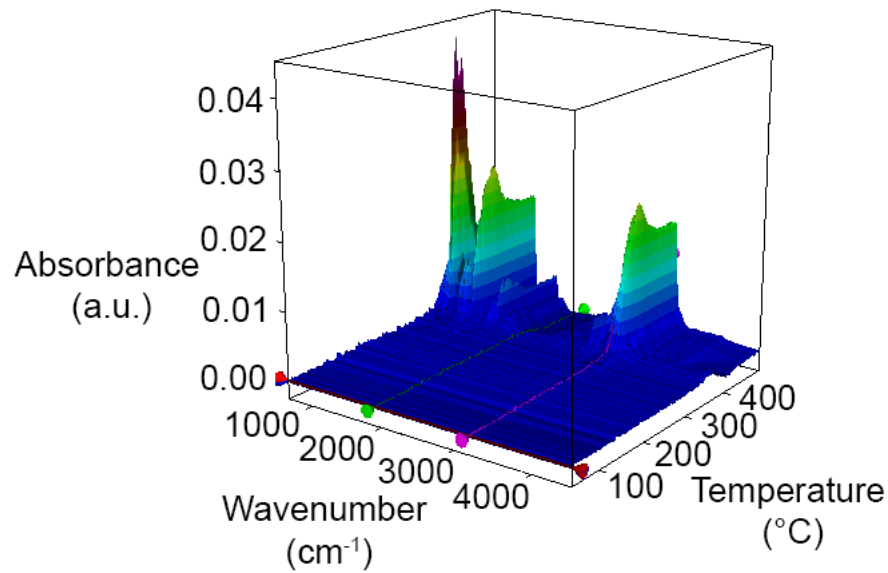**Figure 3.** IR spectra for $CH_3NH_3PbI_3$ from 40 °C to 500 °C.

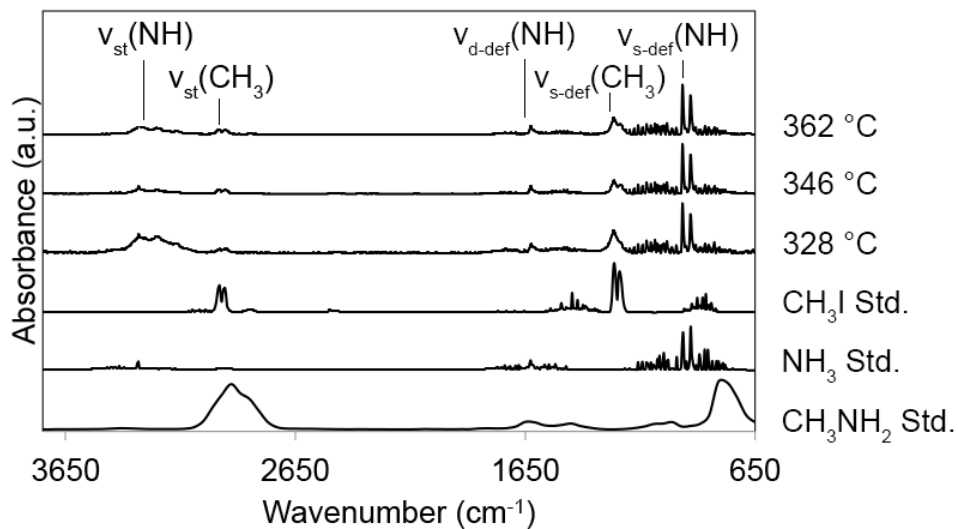**Figure 4.** IR spectra at different temperatures (328 °C, 346 °C, and 362 °C) showing the evolution of gases from $CH_3NH_3PbI_3$ along with standard patterns for CH_3I, NH_3, and CH_3NH_2.[35] HI shows bands at 4000 cm^{-1} that is not shown here, see Figure 5.
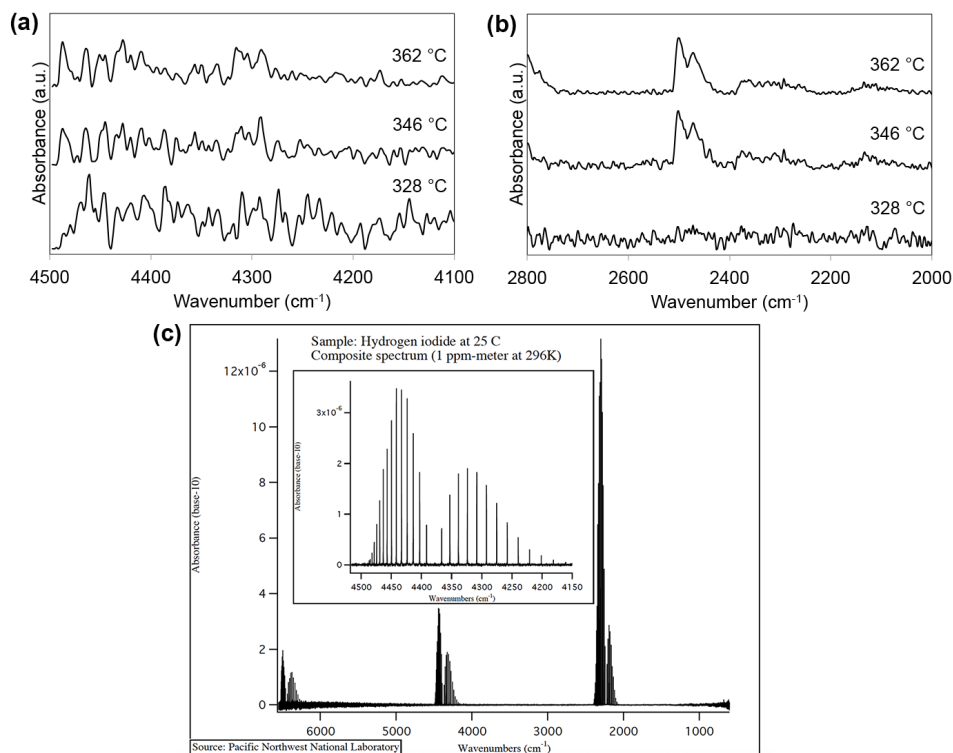
Figure 5. (a) and (b) IR spectra of HI regions (c) standard pattern for HI from Pacific Northwest National Laboratory.[37]

Mass spectrometry of the evolved gases shows a result similar to the IR data and has not been previously reported. Figure 6 shows the mass spectra from analysis at three temperatures: 328, 346, and 362 °C (these are the temperatures reported in the IR spectra in Figure 4). In all spectra, peaks at 19 and 39 m/z are due to tailing from the Ar^{2+} 20 and Ar^+ 40 peaks.[38] An ammonia peak appears in all spectra at 17 m/z and ammonia evolves at even lower temperatures than observed in Figure 6. Peaks for iodomethane (142 m/z) increase with temperature, along with peaks for iodide (127 m/z) which is also from the iodomethane.[35] Iodide 127 has 100% abundance so only one main peak is seen in each spectrum.[39]
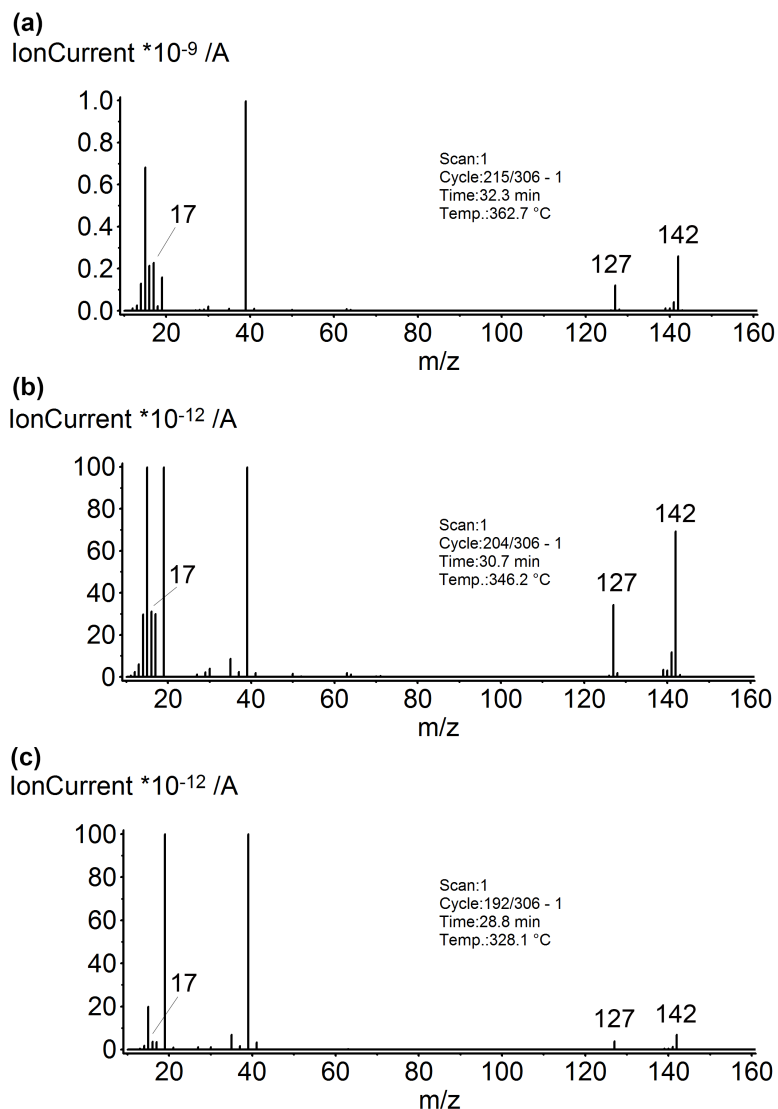
Figure 6. MS spectra for gas evolution from $CH_3NH_3PbI_3$ at (a) 362 °C, (b) 346 °C, (c) 328 °C.

As shown by the IR and MS, $CH_3NH_3PbI_3$ decomposed into ammonia and iodomethane, not methylamine and HI reported in the literature. The TGA literature results matches with the decomposition of the material to CH_3NH_2 and HI but also agrees with what is seen here. We also looked at the other two $CH_3NH_3PbX_3$ (X = Br or Cl) perovskites to determine if they decompose in a similar manner to the iodide or if they follow the literature reported decomposition.

CH₃NH₃PbBr

Unlike methylammonium lead iodide, where the thermal decomposition has been examined at with both TGA and DSC, the thermal decomposition of $CH_3NH_3PbBr_3$ was only studied with TGA.[30] In the report, the perovskite was robust up to 238 °C and had a mass loss of 22.44%. The mass loss was said to be due to escape of CH_3NH_3Br because of the weak bond between the organic cations and inorganic anions of the perovskite. They concluded that CH_3NH_2 and HBr were emitted with the annealing of the bromide perovskite.[30] Using the Netzsch TGA/DSC system, we saw similar results to the literature results for decomposition of the bromide and also to the decomposition of the iodide. Table 2 shows the main compounds that could be present with the decomposition, their molecular weights, and their weight percentage of the methylammonium lead bromide. The TGA measurement for the methylammonium lead bromide, shown in Figure 7, shows a one-step decomposition. The mass loss is about 24%, which corresponds to only having inorganic lead bromide left. DSC displays an endothermic transition at 385 °C, which along with the decomposition of the organic portion of the perovskite, may correspond to the melting point of $PbBr_2$ (371 °C).[33] The organic portions of the perovskite sublime at lower temperatures, CH_3NH_3Br at ~250 °C and CH_3NH_2 at 247 ± 26 °C.[28,40]

Table 2. Compound, molecular weight and mass percentage of $CH_3NH_3PbBr_3$.

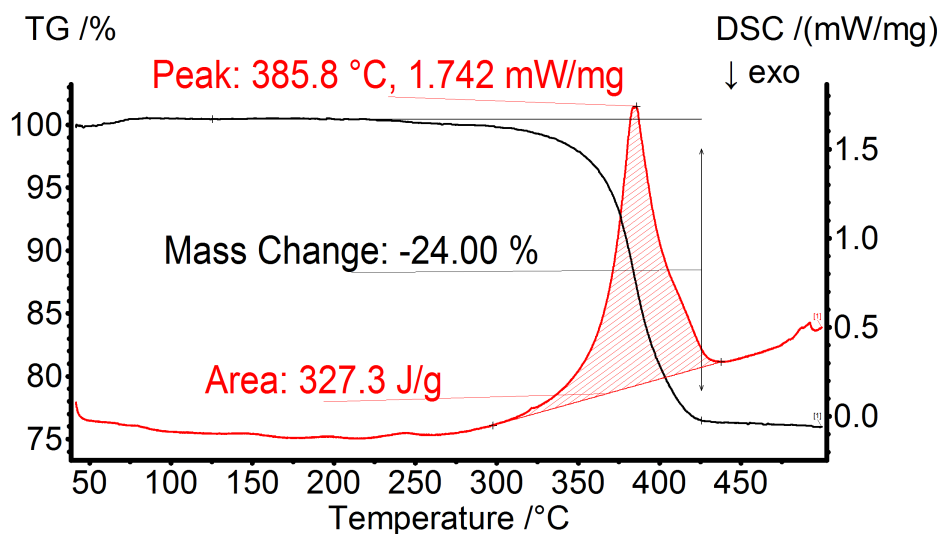| Compound	MW (g/mol)	Percentage (%)
$CH_3NH_3PbBr_3$	479	100
$PbBr_2$	367	77
CH_3NH_2	31	6.5
NH_3	17	3.5
CH_3Br	95	20

Table 2. continued		
HBr	81	17

Figure 7. TGA (black) and DSC (red) for bulk $CH_3NH_3PbBr_3$ from 40 °C to 500 °C.

Recently, an FT-IR study of the evolved gases from $CH_3NH_3PbX_3$ (X = I or Cl) in DMF was investigated.[27] However, the decomposition of $CH_3NH_3PbBr_3$ was not investigated. Figure 8 shows the 3D FT-IR plot of the evolved gases from 500 to 4500 cm^{-1} and 40 to 500 °C. The main evolution of gases starts after 350 °C. The evolved gases at different temperatures are shown in Figure 9. At 350 °C, characteristic IR peaks for both ammonia and methylamine are produced.[35] IR bands due to ammonia at 950, 1600 and 3300-3400 cm^{-1} are NH symmetrical deformations, NH degenerate deformations, and NH symmetric stretches, respectively.[36] The two very strong IR peaks from methylamine are at about 2900 and 780 cm^{-1} from CH_3 deformation/symmetrical stretching and NH_2 wagging.[36] As temperature increases, both compounds are still evolved along with an IR peak growing in at about 1300 cm^{-1} due to bromomethane and CH_3 symmetrical deformations.[35] The CBr stretch is not seen

since it is located at 611 cm^{-1} and is out of range.[36] Peaks at ~3200 cm^{-1} are attributed to NH stretching and observed in the FT-IR spectrum for $CH_3NH_3PbI_3$.[41] Characteristic peaks for HBr do not appear in the IR spectra. Figure 10 shows the region of the IR spectrum where HBr should appear (2350-2750 cm^{-1}) along with the standard spectrum. In all three spectra HBr is not detected. $CH_3NH_3PbBr_3$ seems to follow decomposition similar to $CH_3NH_3PbI_3$, except for evolving methylamine.
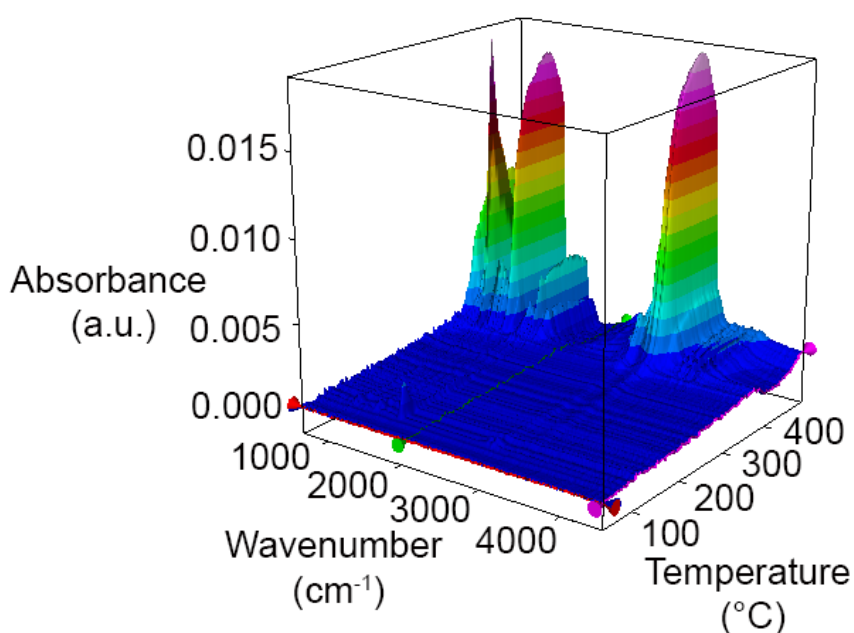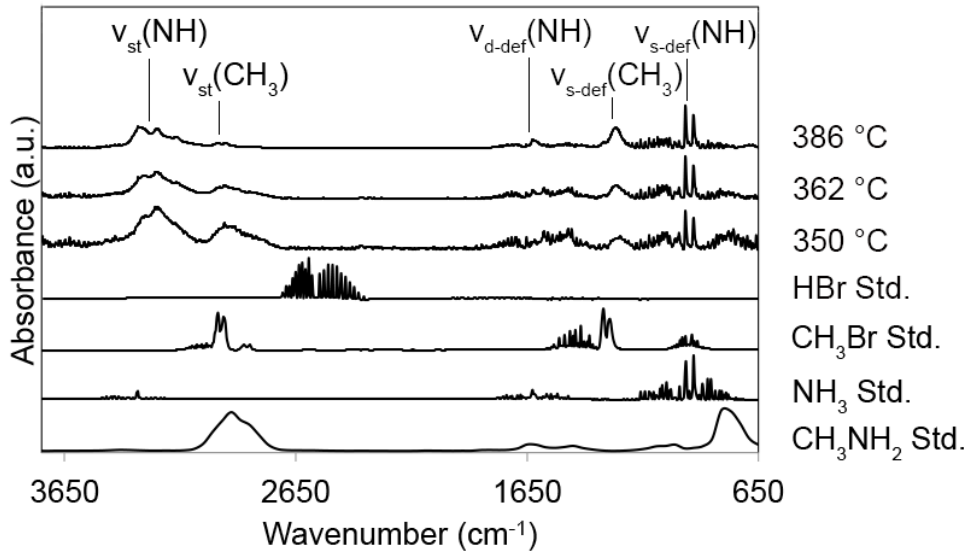

Figure 8. IR spectra for $CH_3NH_3PbBr_3$ from 40 °C to 500 °C.

Figure 9. IR spectra at different temperatures (350 °C, 362 °C, and 386 °C) showing the evolution of gases from $CH_3NH_3PbBr_3$ along with standard IR spectra for HBr, CH_3Br, NH_3, and CH_3NH_2.[35]
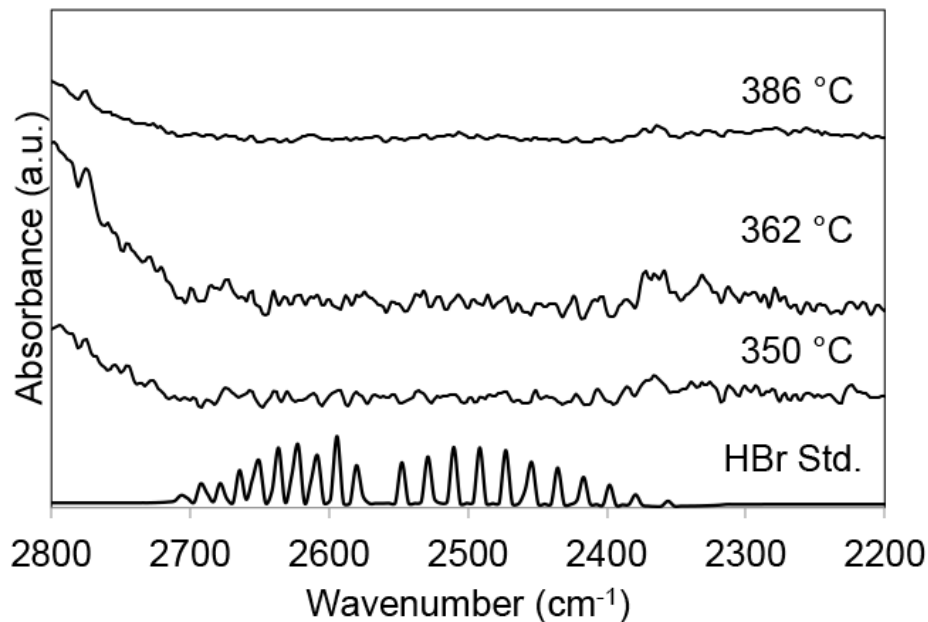

Figure 10. Expanded region of FT-IR spectrum at different temperatures (350, 362 and 386 °C) for HBr along with the HBr standard spectrum for comparison.[35]

Mass spectrometry of the evolved gases from $CH_3NH_3PbBr_3$ display masses for ammonia, bromomethane, and methylamine and support the IR data. Figure 11 shows the

mass spectra over three temperatures: 350, 362, and 386 °C, corresponding to the same temperatures used for the IR spectra in Figure 9. Again, mass peaks at 19 and 39 m/z are due to Ar tailing from Ar^{2+} 20 and Ar^+ 40 m/z peaks.[38] A peak for ammonia appears in all spectra at 17 m/z and for methylamine at 31 m/z. Both ammonia and methylamine evolve first as shown in Figure 11c. Masses for bromomethane at 95 m/z appear at 362 °C. Also, masses for bromine associated with the bromomethane (79 and 81 m/z) appear at 386 °C.[38] For both bromomethane and bromine, the mass clusters are due to bromine having two main isotopes, 79 m/z at 50.69% abundance and 81 m/z at 49.31% abundance.[39]

For both $CH_3NH_3PbX_3$ (X = I or Br) perovskite materials, the decomposition is similar with the evolution of ammonia and methyl halide. However, methylamine is seen from the $CH_3NH_3PbBr_3$. Neither of these pathways has been discerned in the literature with coupling IR and MS to TGA/DSC. To see if $CH_3NH_3PbCl_3$ followed a similar decomposition route, we investigated it using the Netzsch TGA/DSC/IR/MS system.
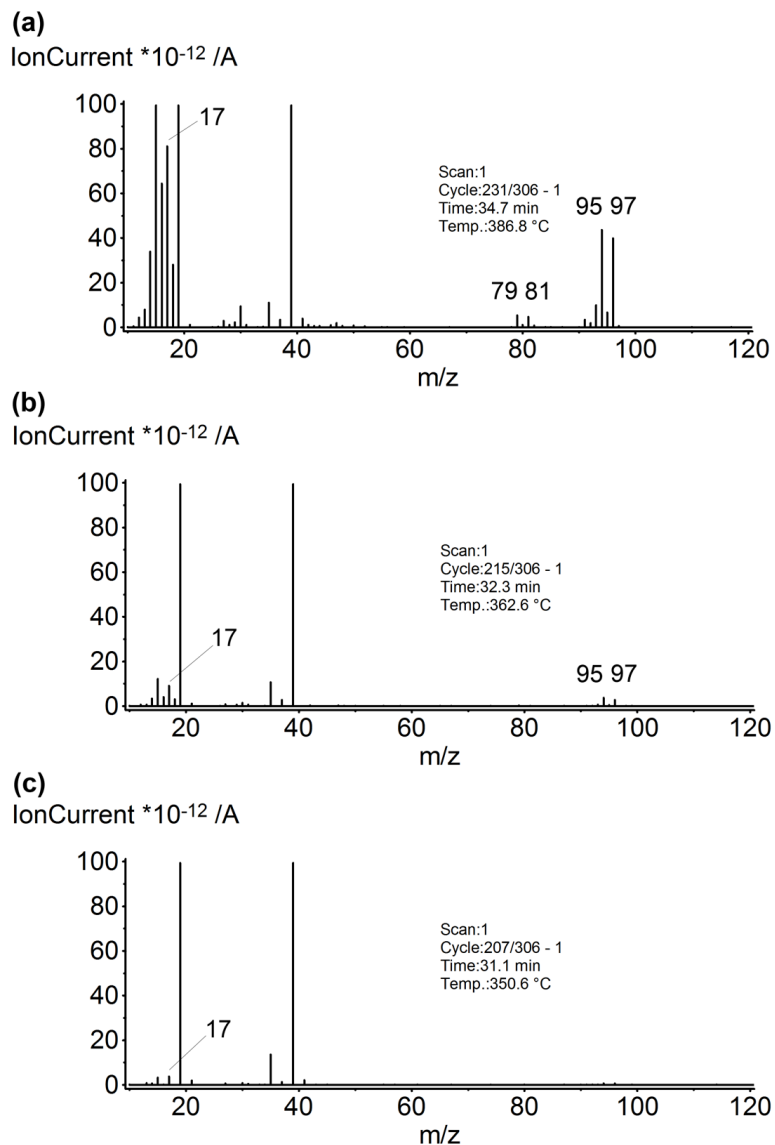
(a)
IonCurrent *10^{-12} /A

Scan:1
Cycle:231/306 - 1
Time:34.7 min
Temp.:386.8 °C

17

95 97

79 81

m/z

(b)
IonCurrent *10^{-12} /A

Scan:1
Cycle:215/306 - 1
Time:32.3 min
Temp.:362.6 °C

17

95 97

m/z

(c)
IonCurrent *10^{-12} /A

Scan:1
Cycle:207/306 - 1
Time:31.1 min
Temp.:350.6 °C

17

m/z

Figure 11. MS spectra for gas evolution from $CH_3NH_3PbBr_3$ at (a) 350 °C, (b) 362 °C, (c) 386 °C.

$CH_3NH_3PbCl_3$

$CH_3NH_3PbCl_3$ decomposes by a different route than $CH_3NH_3PbI_3$ or $CH_3NH_3PbBr_3$. Table 3 shows the main compounds that could be present with the decomposition, their molecular weights, and their weight percentage of the methylammonium lead chloride. The TGA measurement for the methylammonium lead chloride (Figure 12), shows a mass loss of

about 20%, which corresponds to only having inorganic lead chloride left. DSC displays an endothermic transition at 365 °C. The melting point of $PbCl_2$ is 501 °C.[33] Furthermore, CH_3NH_2Cl sublimes at 195 ± 9 °C and CH_3NH_2 at 247 ± 26 °C.[28] DSC data in the literature, reported from room temperature to 100 °C, does not show any transitions, and has not been shown for temperatures greater than 200 °C. Here the DSC results at lower temperatures shows multiple transitions. The transition at 100 °C may be due to loss of water and corresponds to a similar mass loss in the TGA.

Table 3. Compound, molecular weight and mass percentage of $CH_3NH_3PbCl_3$.

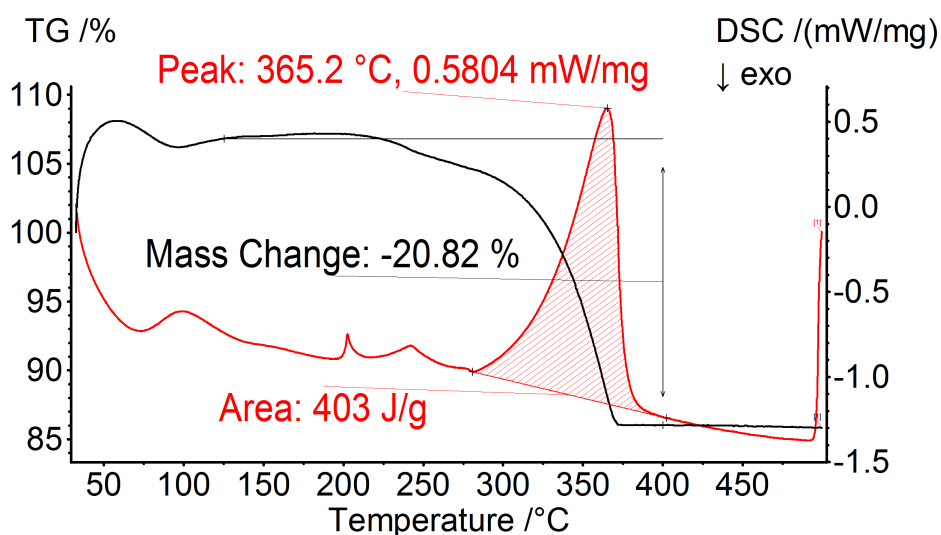| Compound	MW (g/mol)	Percentage (%)
$CH_3NH_3PbCl_3$	346	100
$PbCl_2$	278	80
CH_3NH_2	31	9
NH_3	17	4.9
CH_3Cl	50	14
HCl	36	10

Figure 12. TGA (black) and DSC (red) for bulk $CH_3NH_3PbCl_3$ from 40 °C to 500 °C.

Recently, an FT-IR study of the evolved gases from a mixed halide perovskite, $CH_3NH_3PbI_{3-x}Cl_x$, in DMF was reported.[27] In the literature, primary alkylammonium halides are predicted to decompose to CH_3NH_2 and HX.[42] As shown previously, $CH_3NH_3PbI_3$ and $CH_3NH_3PbBr_3$ did not follow this decomposition; however, the chloride perovskite fits this decomposition pattern. Figure 13 shows the 3D FT-IR plot of the evolved gases from 500 to 4500 cm^{-1} versus temperature (40 to 500 °C). The main evolution of gases start at much lower temperature (200 °C) compared to the iodide and bromide. Looking closer at different temperatures, the progression of evolved gases is determined (Figure 14). At 346 °C, methylamine is observed, along with HCl.[35] Spectra for higher temperatures, 367 and 423 °C, are very similar to the spectrum at 346 °C. Two very intense peaks from methylamine are at about 2900 and 780 cm^{-1} from CH_3 deformation/symmetrical stretching and NH_2 wagging.[36] IR peaks at ~3200 cm^{-1} are attributed to NH stretching and reported in a literature FT-IR spectrum for $CH_3NH_3PbI_3$.[41] HCl peaks at 2700-3100 cm^{-1} are from both the vibrational mode, stretching, and rotation of the H-Cl bond.[43] Figure 15 shows an expanded portion of the IR spectra where HCl is seen, overlapped with the CH_2 stretch from methylamine, along with a standard spectrum of HCl.[35,36] Furthermore, the peak at about 2350 cm^{-1} is due to C=O stretching vibrations from CO_2.[35,36] The sample contained some oxygen to evolve CO_2. Peaks in the fingerprint region are hard to assign but may be due to contamination.

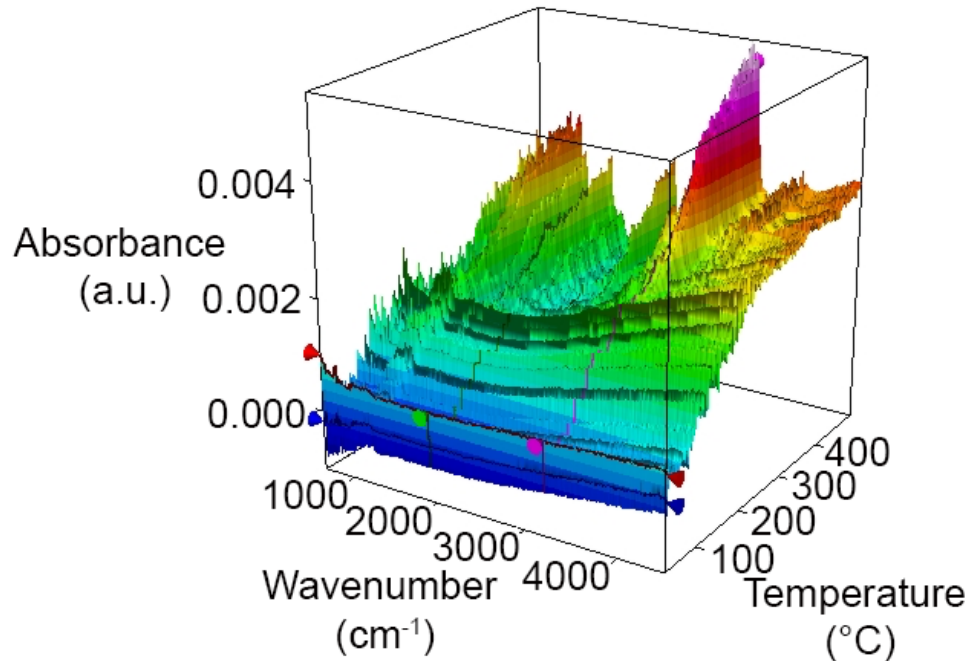**Figure 13.** IR spectra for $CH_3NH_3PbCl_3$ from 40 °C to 500 °C.

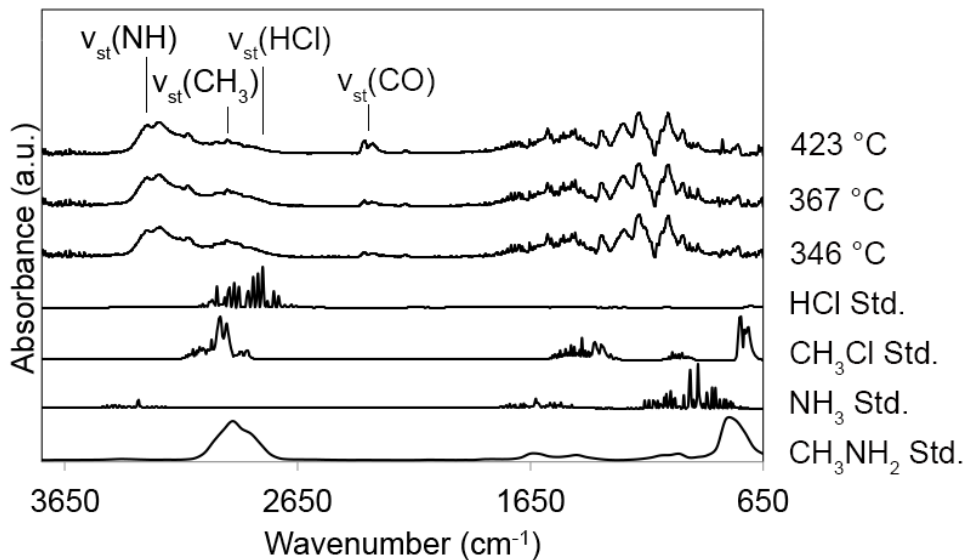**Figure 14.** IR spectra at different temperatures (350 °C, 362 °C, and 386 °C) showing the evolution of gases from $CH_3NH_3PbCl_3$ along with standard IR spectra for HCl, CH_3Cl, NH_3, and CH_3NH_2.[35]
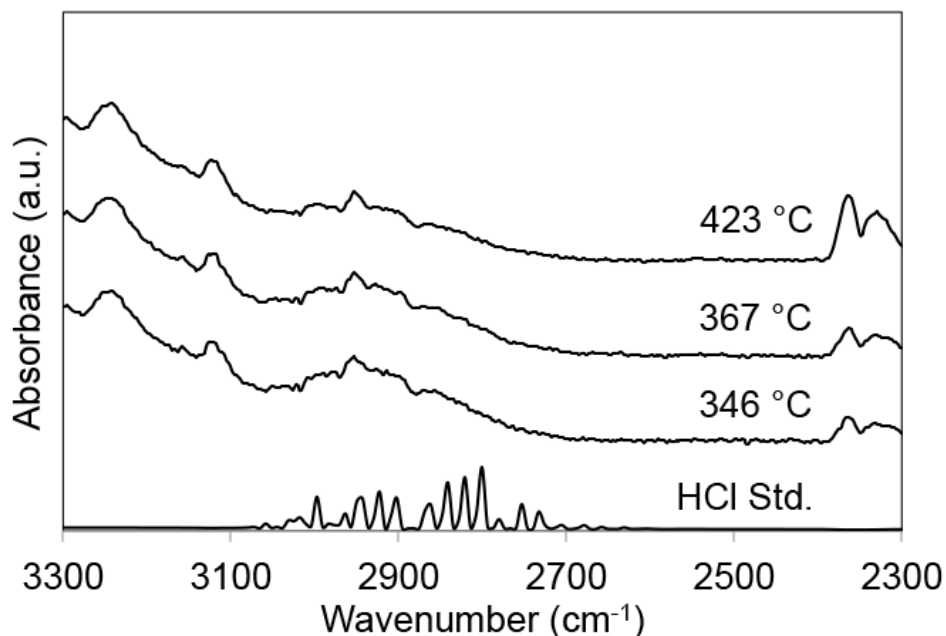
Figure 15. Expanded region of IR spectra for HCl that is overlapped with the CH_3 stretching of methylamine.[35]

Mass spectrometry of the evolved gases from decomposition of $CH_3NH_3PbCl_3$ supports the IR data and has not been previously reported, as is the case with $CH_3NH_3PbX_3$ (X = I or Br). Figure 16 illustrates the mass spectra over three temperatures: 346, 367, and 423 °C; these correspond to the same temperature used for the IR spectra in Figure 14. In all spectra, mass peaks at 19 and 39 m/z are due to Ar as tailing from the Ar^{2+} 20 and Ar^+ 40 m/z.[38] A mass peak for ammonia appears in all spectra at 17 m/z but the standard peaks were not clear in the FT-IR. There are mass peaks for both the methylamine and hydrochloric acid/chloride at 31 and 35 m/z, respectively.[38] Chlorine has two main isotopes, 35 m/z with 75.76% abundance and 37 m/z with 24.24% abundance.[39] Since the peaks are so small for the 35 isotope, the 37 is difficult to see unless the ion current axis expanded to smaller values.

(a)
IonCurrent *10⁻¹² /A

Scan:1
Cycle:255/306 - 1
Time:38.4 min
Temp.:423.5 °C

m/z

(b)
IonCurrent *10⁻¹² /A

Scan:1
Cycle:218/306 - 1
Time:32.8 min
Temp.:367.7 °C

m/z

(c)
IonCurrent *10⁻¹² /A

Scan:1
Cycle:204/306 - 1
Time:30.7 min
Temp.:346.5 °C

m/z
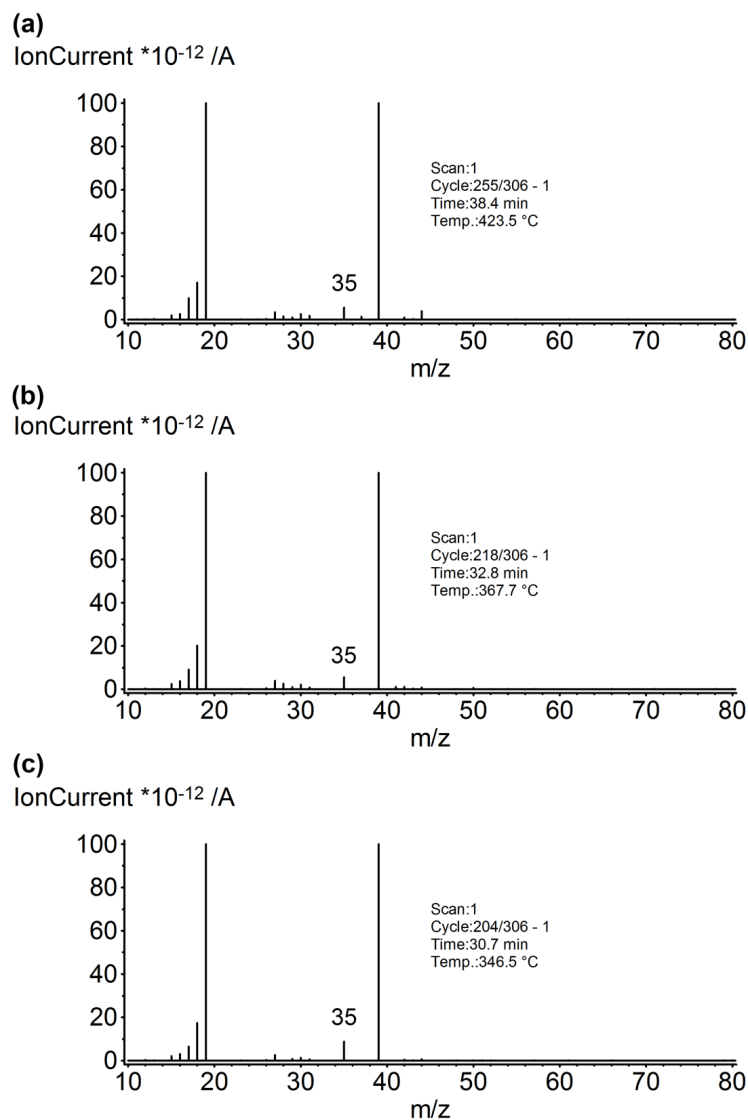
Figure 16. MS spectra for gas evolution from $CH_3NH_3PbCl_3$ at (a) 346 °C, (b) 367 °C, (c) 423 °C.

Conclusion

In summary, the decomposition of $CH_3NH_3PbX_3$ (X = I, Br or Cl) occurs differently for each of the halides that was studied. First, all the methylammonium lead halides decompose to the inorganic lead halide determined by the TGA mass loss data. From DSC, the endotherms of the materials are all different: Iodide at 358 °C, bromide at 385°C, and chloride at 365 °C. In the literature, the decomposition is reported to evolve HX and CH_3NH_2

or CH_3NH_3X and HX. However, we see by FT-IR and MS that the iodide perovskite decomposes to ammonia and iodomethane. The bromide perovskite decomposes by a similar route but produces ammonia, methylamine and bromomethane. In agreement with published reports, the chloride perovskite breaks down to methylamine and hydrochloric acid. Elucidating the different thermal decomposition pathways for the $CH_3NH_3PbX_3$ (X = I, Br or Cl) perovskites helps to discern how to increase the stability of the materials.

In the future, our group will look at different routes to increase the stability of methylammonium lead halide materials. The four routes are: 1. Using all inorganic cations such as $CsPbX_3$, 2. Using C-D materials such as $CD_3NH_3PbX_3$ or $CD_3ND_3PbX_3$, 3. Changing the basicity or acidity by using $HONH_4^+$ or NH_4^+, 4. Strengthening the C-N bond by using NH_2-CH=NH_2^+ or CH_3-NH_2^+-CH_3. Investigating these materials will give a better understanding of the decomposition and increasing the thermal stability of the methylammonium lead halide perovskites for solar cells.

References

[1] Zhou, H.; Chen, Q.; Li, G.; Luo, S.; Song, T.; Duan, H.-S.; Hong, Z.; You, J.; Liu, Y.; Yang, Y. *Science* **2014**, *345*, 542–546.

[2] Kojima, A.; Teshima K.; Shirai, Y.; Miyasaka, T. *J. Am. Chem. Soc.* **2009**, *131*, 6050–6051.

[3] Kim, H.-S.; Lee, C.-R.; Im, J.-H.; Lee, K.-B.; Moehl, T.; Marchioro, A.; Moon, S.-J.; Humphry-Baker, R.; Yum, J.-H.; Moser, J. E.; Grätzel, M.; Park, N.-G. *Sci. Rep*. **2012**, *2*, 591-1–7.

[4] Park, N.-G. *Mater. Today* **2015**, *18*, 65–72.

[5] Gao, P.; Grätzel, M.; Nazeeruddin, M. K. *Energy Environ. Sci.* **2014**, *7*, 2448–2463.

[6] Jung, H. S.; Park, N.-G. *Small* **2015**, *11*, 10–25.

[7] Green, M. A.; Ho-Baillie, A.; Snaith, H. J. *Nat. Photonics* **2014**, *8*, 506–514.

[8] Snaith, H. J. *J. Phys. Chem. Lett.* **2013**, *4*, 3623–3630.

[9] Boix, P. P.; Nonomura, K.; Mathews, N.; Mhaisalkar, S. G. *Mater. Today* **2014**, *17*, 16–23.

[10] Noh, J. H.; Im, S. H.; Heo, J. H.; Mandal, T. N.; Seok, S. I. *Nano Lett.* **2013**, *13*, 1764–1769.

[11] Cheng, Z.; Lin, J. *CrystEngComm* **2010**, *115*, 2646–2662.

[12] Ito, S.; Tanaka, S.; Manabe, K.; Nishino, H. *J. Phys. Chem. C* **2014**, *118*, 16995–17000.

[13] Lee, M. M.; Teuscher, J.; Miyasaka, T.; Murakami, T. N.; Snaith, H. J. *Science* **2012**, *338*, 643–647.

[14] Niu, G.; Li, W.; Meng, F.; Wang, L.; Dong, H.; Qiu, Y. *J. Mater. Chem. A* **2014**, *2*, 705–710.

[15] Habisreutinger, S. N.; Leijtens, T.; Eperon, G. E.; Stranks, S. D.; Nicholas, R. J.; Snaith, H. J. *Nano Lett.* **2014**, *14*, 5561–5568.

[16] Mei, A.; Li, X.; Liu, L.; Ku, Z.; Liu, T.; Rong, Y.; Xu, M.; Hu, M.; Chen, J.; Yang, Y.; Grätzel, M.; Han, H. *Science* **2014**, *345*, 295–298.

[17] Zhu, F.; Men, L.; Guo, Y.; Zhu, Q.; Bhattacharjee, U.; Goodwin, P. M.; Petrich, J. W.; Smith, E. A.; Vela, J. *ACS Nano* **2015**, *X*, X–X.

[18] Yamamuro, O.; Matsuo, T.; Suga, H.; David, W. I. F.; Ibberson, R. M.; Leadbetter, A. J. *Acta Crystallogr., Sect. B: Struct. Sci.* **1992**, *B48*, 329–336.

[19] Yamamura, O., Onoda-Yamamuro, N.; Suga, H.; Kamiyama, T.; Ishigaki, T.; Asano, H. *J. Phys. Chem. Solids* **1994**, *55*, 383–389.

[20] Waldron, R. D. *J. Chem. Phys.* **1953**, *21*, 734–741.

[21] Theoret, A.; Sandorfy, C. *Spectrochim. Acta*, **1967**, *23A*, 519–542.

[22] Ishida, H.; Ikeda, R.; Nakamura, D. *J. Phys. Chem*. **1982**, *86*, 1003–1008.

[23] Cabana, A.; Sandorfy, C. *Spectrochim. Acta*, **1962**, *18*, 843–861.

[24] Aston, J. G.; Ziemer, C. W. *J. Am. Chem. Soc.* **1946**, *68*,1405–1413.

[25] Ishida, H.; Ikeda, R.; Nakamura, D. *Phys. Status Solidi* **1982**, *70*, K151–K154.

[26] Im, J.-H.; Lee, C.-R.; Lee, J.-W.; Park, S.-W.; Park, N.-G. *Nanoscale*, **2011**, *3*, 4088–4093.

[27] Baikie, T.; Fang, Y.; Kadro, J. M.; Schreyer, M.; Wei, F.; Mhaisalkar, S. G.; Grätzel, M.; White, T. J. *J. Mater. Chem. A* **2013**, *1*, 5628–5641.

[28] Dualeh, A.; Gao, P.; Seok, S.; Nazeeruddin, M. K.; Grätzel, M. *Chem. Mater.* **2014**, *26*, 6160–6164.

[29] Stoumpos, C. C.; Malliakas, C. D.; Kanatzidis, M. G. *Inorg. Chem.* **2013**, *52*, 9019–9038.

[30] Liu, C.; Qiu, Z.; Meng, W.; Chen, J.; Qi, J.; Dong, C.; Wang, M. *Nano Energy* **2015**, *12*, 59–68.

[31] Williams, A. E.; Holliman, P. J.; Carnie, M. J.; Davies, M. L.; Worsley, D. A.; Watson, T. M. *J. Chem. Mater. A* **2014**, *2*, 19338–19346.

[32] Papavassiliou, G. C.; Pagona, G.; Karousis, N.; Mousdis, G. A.; Koutselas, I.; Vassilakopoulou, A. *J. Mater. Chem.* **2012**, *22*, 8271–8280.

[33] "Physical Constants of Inorganic Compounds" in *CRC Handbook of Chemistry and Physics 95th Edition*, CRC Press, Taylor & Francis, Boca Raton, FL, 2014-2015, http://www.hbcpnetbase.com (accessed March 30, 2015).

[34] Poglitsch, A.; Weber, D. *J. Chem. Phys*. **1987**, *87*, 6373–6378.

[35] NIST Mass Spec Data Center, Stein, S. E. "Infrared Spectra" in *NIST Chemistry WebBook, NIST Standard Reference Database Number 69*, Eds. P. J. Linstrom and W. G. Mallard, National Institute of Standards and Technology, Gaithersburg MD, 20899, http://webbook.nist.gov, (accessed March 30, 2015).

[36] Shimanouchi, T. "Molecular Vibrational Frequencies" in *NIST Chemistry WebBook, NIST Standard Reference Database Number 69*, Eds. P. J. Linstrom and W. G. Mallard, National Institute of Standards and Technology, Gaithersburg MD, 20899, http://webbook.nist.gov, (accessed March 30, 2015).

[37] Hydrogen Iodide IR Spectrum from Pacific Northwest National Laboratory database, https://secure2.pnl.gov/nsd/nsd.nsf/b9f8ad7b5d2da07488256b1f00755d0a/5b28f5401478155 f88257592005ec9fe/$FILE/HI_25T.pdf (accessed March 30, 2015).

[38] NIST Mass Spec Data Center, Stein, S. E. "Mass Spectra" in *NIST Chemistry WebBook, NIST Standard Reference Database Number 69*, Eds. P. J. Linstrom and W. G. Mallard, National Institute of Standards and Technology, Gaithersburg MD, 20899, http://webbook.nist.gov, (accessed March 30, 2015).

[39] Holden, N. E. "Table of the Isotopes" in *CRC Handbook of Chemistry and Physics 95th Edition*, CRC Press, Taylor & Francis, Boca Raton, FL, 2014-2015, http://www.hbcpnetbase.com (accessed March 30, 2015).

[40] Zhao, Y.; Zhu, K. *J. Am. Chem. Soc.* **2014**, *136*, 12241–12244.

[41] Jeon, N. J.; Noh, J. H.; Kim, Y. C.; Yang, W. S.; Ryu, S.; Seok, S. I. *Nat. Mater.* **2014**, *13*, 897–903.

[42] Sawicka, M.; Storoniak, P.; Skurski, P.; Blazejowski, J.; Rak, J. *Chem. Phys.* **2006**, *324*, 425–437.

[43] Nakamoto, K. Infrared and Raman Spectra of Inorganic and Coordination Compounds, Theory and Applications in Inorganic Chemistry, John Wiley & Sons: New Jersey, 2009, pp 9–15.

CHAPTER 5

CONCLUSIONS AND FUTURE WORK

In conclusion, we investigated the chemical and thermal stability of different semiconductor materials. In chapter 2, CdSe and CdS nanorods were studied for robustness under harsh conditions usually used in catalysis. We synthesized copper(I) nitride and examined its decomposition to copper(II) oxide in Chapter 3. Finally, in Chapter 4, the thermal properties of bulk methylammonium lead halides were explored to determine the decomposition products; this could lead to an increased thermal stability of perovskite materials for solar cells.

We investigated the general chemical reactivity of II-VI semiconductor nanorods, with an emphasis on CdSe nanorods. HCl and HNO_3 react rapidly with CdSe nanorods; after 12 h, the CdSe absorption and band edge PL disappear and Se and SeO_2 (HNO_3) form. CdSe nanorods are relatively stable in basic conditions, as well as in the presence of strong oxidants. Neither bases nor oxidants caused significant changes in absorption spectra, although H_2O_2 caused a decrease in emission, likely due to the introduction of small amounts of CdO and SeO_2 on the nanorod surface. However, bases slightly etch the nanorods along their axis, as evidenced by a decrease in intensity and widening of the 002 XRD peak relative to the 100 and 110 XRD peaks. CdSe nanorods are relatively stable for long periods of time under air at temperatures up to 350 °C. However, roasting CdSe to 600 °C produces polycrystalline rock salt CdO. Neither CdO nor CdSe nanorods reduce to Cd in the presence of H_2 at elevated temperatures. Using n-BuLi, CdSe reduces to Cd metal at 300 °C. Lower reaction temperatures than 300 °C result in incomplete reduction or no reduction at all.

Along with their chemical reactivity, we also explored the thermal stability and effect of curvature on the stability of CdSe and CdS nanorods. Variable temperature (VT) XRD studies showed that II-VI nanorods respond to heating in three stages: (i) annealing, (ii) axial melting and (iii) coalescence. Furthermore, DTA and TGA of CdSe and CdS nanorods showed that axial melting is not reliant on the type of inorganic crystalline material but on the ligand(s) coating its surface. Ligands coating the nanorod surface help maintain their anisotropy and specific aspect ratio. In view of this axial melting behavior, we looked at the effect of curvature on the activity of II-VI nanorods: For example, heterogeneous nucleation of SiO_2 on regularly-shaped CdSe nanorods starts at both tips at the same time, while heterogeneous nucleation of SiO_2 starts from the thinner CdS-rich tip of axially anisotropic $CdS_{0.4}Se_{0.6}$ nanorods. A better and more systematic understanding of the chemical reactivity and general stability of II-VI semiconductor nanostructures may greatly help in furthering their application to photocatalysis, photovoltaics, optics and light emitting devices.

Nanocrystalline Cu_3N was synthesized from nanocrystalline Cu_2O and one of two nitrogen sources, ammonia or urea. Using urea leads to slightly more phase-pure Cu_3N, as observed by XRD. In addition, the use of ammonia as the nitridation reagent requires a longer reaction time and higher temperature. TEM reveals that the cubic morphology of the initial Cu_2O nanocrystals is lost upon nitridation to Cu_3N. Using ammonia produces clusters of spherical particles whereas with urea produced a mixture of several different morphologies (rods, sheets, and aggregates). Electronic structure, calculations of the DOS appear to underestimate, but agree with the presence of, a band gap of under 1 eV for both Cu_2O and Cu_3N phases.

Cu$_3$N nanocrystals spontaneously decompose to nanocrystalline CuO at room temperature. Control experiments show that both air and moisture are necessary for this transformation to take place. Cu$_3$N decomposition occurs within 15 days to produce substoichiometric amounts of ammonia. Specifically, ammonia was produced in 60% chemical yield, as measured using the indophenol method. Because Cu$_3$N decomposition requires H$_2$O and produces substoichiometric amounts of NH$_3$, we conclude that this reaction proceeds through a complex stoichiometry that involves the concomitant release of both N$_2$ and NH$_3$. This is a thermodynamically unfavorable outcome, strongly indicating that H$_2$O facilitates the kinetics of the reaction by lowering the energy barrier for Cu$_3$N decomposition. Additional studies will be required to assess the potential reversibility and catalytic usefulness of this transformation.

The decomposition of CH$_3$NH$_3$PbX$_3$ (X = I, Br or Cl) occurs differently for each of the halides that were studied. First, all the methylammonium lead halides decompose to the inorganic lead halide determined by the TGA mass loss data. In the literature, the decomposition is reported to evolve HX and CH$_3$NH$_2$ or CH$_3$NH$_3$X and HX. However, we see by FT-IR and MS that the iodide decomposes to ammonia and iodomethane. The bromide decomposes by a similar route but produces ammonia, methylamine and bromomethane. In agreement with published reports, the chloride perovskite breaks down to methylamine and hydrochloric acid. Elucidating the different thermal decomposition pathways for the CH$_3$NH$_3$PbX$_3$ (X = I, Br or Cl) perovskites helps to discern how to increase the stability of the materials.

In the future, our group will look at different routes to increase the stability of methylammonium lead halide materials. The four routes are: 1. Using all inorganic cations

such as $CsPbX_3$, 2. Using materials such as $CD_3NH_3PbX_3$ or $CD_3ND_3PbX_3$, 3. Changing the basicity or acidity by using $HONH_4^+$ or NH_4^+, 4. Strengthening the C-N bond by using $NH_2\text{-}CH=NH_2^+$ or $CH_3\text{-}NH_2^+\text{-}CH_3$. Investigating these materials will give a better understanding of the decomposition and increasing the thermal stability of the methylammonium lead halide perovskites for solar cells.